

AD-A214 252

WING FILE COPY

4

Technical Report 1147

July 1987

Accuracy of HF Skywave Field Strength Models: **PROPHET** and **HFBC84**

R. A. Sprague



Approved for public release; distribution is unlimited.

89 11 08 036

NAVAL OCEAN SYSTEMS CENTER

San Diego, California 92152-5000

E. G. SCHWEIZER, CAPT, USN
Commander

R. M. HILLYER
Technical Director

ADMINISTRATIVE INFORMATION

This work was performed by the Ionospheric Branch, Code 542, Naval Ocean Systems Center, for the Space and Naval Warfare Systems Command, PDW107-6.

Released by
D. B. Sailors, Head
Ionospheric Branch

Under authority of
J. H. Richter, Head
Ocean and Atmospheric
Sciences Division

UNCLASSIFIED
SECURITY CLASSIFICATION OF THIS PAGE

REPORT DOCUMENTATION PAGE

1a. REPORT SECURITY CLASSIFICATION UNCLASSIFIED		1b. RESTRICTIVE MARKINGS					
2a. SECURITY CLASSIFICATION AUTHORITY		3. DISTRIBUTION/AVAILABILITY OF REPORT Approved for public release; distribution is unlimited.					
2b. DECLASSIFICATION/DOWNGRADING SCHEDULE							
4 PERFORMING ORGANIZATION REPORT NUMBER(S) NOSC TR 1147		5. MONITORING ORGANIZATION REPORT NUMBER(S)					
6a. NAME OF PERFORMING ORGANIZATION Naval Ocean Systems Center	6b. OFFICE SYMBOL (if applicable) Code 542	7a. NAME OF MONITORING ORGANIZATION					
6c. ADDRESS (City, State and ZIP Code) San Diego, CA 92152-5000		7b. ADDRESS (City, State and ZIP Code)					
8a. NAME OF FUNDING/SPONSORING ORGANIZATION Space and Naval Warfare Systems Command	8b. OFFICE SYMBOL (if applicable) SPWR PDW107-6	9. PROCUREMENT INSTRUMENT IDENTIFICATION NUMBER					
8c. ADDRESS (City, State and ZIP Code) Washington, DC 20363		10. SOURCE OF FUNDING NUMBERS <table border="1"><tr><td>PROGRAM ELEMENT NO. RDDA</td><td>PROJECT NO. NSA</td><td>TASK NO. MP57</td><td>AGENCY ACCESSION NO. DN288 591</td></tr></table>		PROGRAM ELEMENT NO. RDDA	PROJECT NO. NSA	TASK NO. MP57	AGENCY ACCESSION NO. DN288 591
PROGRAM ELEMENT NO. RDDA	PROJECT NO. NSA	TASK NO. MP57	AGENCY ACCESSION NO. DN288 591				
11. TITLE (Include Security Classification) Accuracy of HF Skywave Field Strength Models: PROPHET and HFBC84							
12. PERSONAL AUTHOR(S) R.A. Sprague							
13a. TYPE OF REPORT Final	13b. TIME COVERED FROM Sep 85 TO Sep 86	14. DATE OF REPORT (Year, Month, Day) July 1987	15. PAGE COUNT 95				
16. SUPPLEMENTARY NOTATION							
17. COSATI CODES		18. SUBJECT TERMS (Continue on reverse if necessary and identify by block number) maximum usable frequency					
19. ABSTRACT (Continue on reverse if necessary and identify by block number) <p>This report presents a comparison of the predictions of the PROPHET and HFBC84 field strength models to observed data. Both models are described and plots of various statistical quantities relating to their predictive performance are given. Both models show large average residual and root mean square residual in predictions for frequencies which exceed the maximum usable frequency for a mode. The HFBC84 model shows large error for path lengths greater than 7000 km. The author suggests replacement for the current PROPHET field strength model based on the results of the comparison.</p>							
20. DISTRIBUTION/AVAILABILITY OF ABSTRACT <input type="checkbox"/> UNCLASSIFIED/UNLIMITED <input checked="" type="checkbox"/> SAME AS RPT <input type="checkbox"/> DTIC USERS		21. ABSTRACT SECURITY CLASSIFICATION UNCLASSIFIED					
22a. NAME OF RESPONSIBLE INDIVIDUAL R.A. Sprague		22b. TELEPHONE (Include Area Code) (619) 225-7706	22c. OFFICE SYMBOL Code 542				

DD FORM 1473, 84 JAN

83 APR EDITION MAY BE USED UNTIL EXHAUSTED
ALL OTHER EDITIONS ARE OBSOLETE

UNCLASSIFIED
SECURITY CLASSIFICATION OF THIS PAGE

UNCLASSIFIED

SECURITY CLASSIFICATION OF THIS PAGE (When Data Entered)

DD FORM 1473, 84 JAN

UNCLASSIFIED

SECURITY CLASSIFICATION OF THIS PAGE(When Data Entered)

EXECUTIVE SUMMARY

OBJECTIVE

Determine the accuracy of predictions of the current PROPHET field strength model. Compare the results to those for an accepted standard model (HFBC84).

RESULTS

1. Both models show poor performance for cases where the operating frequency exceeds the maximum usable frequency.
2. HFBC84 shows a large average residual for paths of length 7000 km or greater.
3. PROPHET shows a large average residual in winter while HFBC84 performs poorly in summer.
4. PROPHET shows a large root mean square (rms) residual and rms relative residual at low sunspot numbers.
5. PROPHET shows large average residual as a function of midpath local time.

Accession For	
NTIS GRA&I <input checked="" type="checkbox"/>	
DTIC TAB <input type="checkbox"/>	
Unannounced <input type="checkbox"/>	
Justification	
By _____	
Distribution/	
Availability Codes	
Dist	Avail and/or
	Special
A-1	

2
NSP/PC/26

CONTENTS

	PAGE
INTRODUCTION	1
FIELD STRENGTH PREDICTION	2
MUF Predictions	3
Simplified CCIR Method	3
MINIMUF-85	5
Field Strength Calculations	7
HFBC84 Method	7
Path Lengths < 7000 km	7
Path Lengths Between 7000 and 9000 km	17
Path Lengths Greater Than 9000 km (the FTZ Model)	18
Over-the-MUF Field Strength Model	25
PROPHET Field Strength Model	27
FIELD STRENGTH DATA BASE AND SCREENING PROCEDURE	30
RESULTS OF COMPARISON TO DATA	34
Overall Results as a Function of f/MUF Ratio	34
Individual Circuit Results	39
Circuit Length Results	46
Seasonal Results	46
Sunspot Number Results	53
Midpath Local Time Results	63
DISCUSSION AND RECOMMENDATIONS	73
REFERENCES	76
APPENDIX A: OVERALL RESULTS	A-1

ILLUSTRATIONS

	PAGE
1. Average relative residual as a function of frequency-to-MUF ratio ..	35
2. Average relative residual as a function of frequency-to-MUF ratio ..	35
3. Average absolute relative residual as a function of frequency-to-MUF ratio	36
4. Root mean square residual as a function of frequency-to-MUF ratio ..	36
5. Root mean square relative residual as a function of frequency-to-MUF ratio	37
6. Correlation coefficient as a function of frequency-to-MUF ratio	37
7. Average residual for each circuit with frequency less than or equal to the MUF	40
8. Root mean square residual for each circuit with frequency less than or equal to the MUF	40
9. Average relative residual for each circuit with frequency less than or equal to the MUF	41
10. Root mean square relative residual for each circuit with frequency less than or equal to the MUF	41
11. Average absolute relative residual for each circuit with frequency less than or equal to the MUF	42
12. Correlation coefficient for each circuit with frequency less than or equal to the MUF	42
13. Average residual for each circuit with frequency greater than the MUF	43
14. Root mean square residual for each circuit with frequency greater than the MUF	43
15. Average relative residual for each circuit with frequency greater than the MUF	44
16. Root mean square relative residual for each circuit with frequency greater than the MUF	44
17. Average absolute relative residual for each circuit with frequency greater than the MUF	45
18. Correlation coefficient for each circuit with frequency greater than the MUF	45

19.	Average residual as a function of circuit length for frequencies less than or equal to the MUF	47
20.	Root mean square residual as a function of circuit length for frequencies less than or equal to the MUF	47
21.	Average relative residual as a function of circuit length for frequencies less than or equal to the MUF	48
22.	Root mean square relative residual as a function of circuit length for frequencies less than or equal to the MUF	48
23.	Average absolute relative residual as a function of circuit length for frequencies less than or equal to the MUF	49
24.	Correlation coefficient as a function of circuit length for frequencies less than or equal to the MUF	49
25.	Average residual as a function of circuit length for frequencies greater than the MUF	50
26.	Root mean square residual as a function of circuit length for frequencies greater than the MUF	50
27.	Average relative residual as a function of circuit length for frequencies greater than the MUF	51
28.	Root mean square relative residual as a function of circuit length for frequencies greater than the MUF	51
29.	Average absolute relative residual as a function of circuit length for frequencies greater than the MUF	52
30.	Correlation coefficient as a function of circuit length for frequencies greater than the MUF	52
31.	Average residual as a function of season for frequencies less than or equal to the MUF	54
32.	Root mean square residual as a function of season for frequencies less than or equal to the MUF	54
33.	Average relative residual as a function of season for frequencies less than or equal to the MUF	55
34.	Root mean square relative residual as a function of season for frequencies less than or equal to the MUF	55
35.	Average absolute relative residual as a function of season for frequencies less than or equal to the MUF	56
36.	Correlation coefficient as a function of season for frequencies less than or equal to the MUF	56

37. Average residual as a function of season for frequencies greater than the MUF	57
38. Root mean square residual as a function of season for frequencies greater than the MUF	57
39. Average relative residual as a function of season for frequencies greater than the MUF	58
40. Root mean square relative residual as a function of season for frequencies greater than the MUF	58
41. Average absolute relative residual as a function of season for frequencies greater than the MUF	59
42. Correlation coefficient as a function of season for frequencies greater than the MUF	59
43. Average residual as a function of smoothed sunspot number for frequencies less than or equal to the MUF	60
44. Root mean square residual as a function of smoothed sunspot number for frequencies less than or equal to the MUF	60
45. Average relative residual as a function of smoothed sunspot number for frequencies less than or equal to the MUF	61
46. Root mean square relative residual as a function of smoothed sunspot number for frequencies less than or equal to the MUF	61
47. Average absolute relative residual as a function of smoothed sunspot number for frequencies less than or equal to the MUF	62
48. Correlation coefficient as a function of smoothed sunspot number for frequencies less than or equal to the MUF	62
49. Average residual as a function of smoothed sunspot number for frequencies greater than the MUF	64
50. Root mean square residual as a function of smoothed sunspot number for frequencies greater than the MUF	64
51. Average relative residual as a function of smoothed sunspot number for frequencies greater than the MUF	65
52. Root mean square relative residual as a function of smoothed sunspot number for frequencies greater than the MUF	65
53. Average absolute relative residual as a function of smoothed sunspot number for frequencies greater than the MUF	66
54. Correlation coefficient as a function of smoothed sunspot number for frequencies greater than the MUF	66

55. Average residual as a function of midpath local time for frequencies less than or equal to the MUF	67
56. Root mean square residual as a function of midpath local time for frequencies less than or equal to the MUF	67
57. Average relative residual as a function of midpath local time for frequencies less than or equal to the MUF	68
58. Root mean square relative residual as a function of midpath local time for frequencies less than or equal to the MUF	68
59. Average absolute relative residual as a function of midpath local time for frequencies less than or equal to the MUF	69
60. Correlation coefficient as a function of midpath local time for frequencies less than or equal to the MUF	69
61. Average residual as a function of midpath local time for frequencies greater than the MUF	70
62. Root mean square residual as a function of midpath local time for frequencies greater than the MUF	70
63. Average relative residual as a function of midpath local time for frequencies greater than the MUF	71
64. Root mean square relative residual as a function of midpath local time for frequencies greater than the MUF	71
65. Average absolute relative residual as a function of midpath local time for frequencies greater than the MUF	72
66. Correlation coefficient as a function of midpath local time for frequencies greater than the MUF	72
67. Comparison of full Wheeler method and current CCIR method for over-the-MUF loss	74

TABLES

1. Summary of comparison of MINIMUF-85 and HFBC84 MUF predictions	7
2. Summary of transmission circuits contained in the field strength data base	31

INTRODUCTION

High frequency (HF) skywave field strength and transmission loss predictions are necessary for a variety of reasons, apart from any theoretical interest in making such calculations. For example, in establishing a communication circuit we must have a preliminary estimate of expected median system performance. Also, effective management of frequency assets requires knowledge of the effect of ionospheric characteristic variations on system performance. These variations are then used to provide updated predictions of optimal operational frequencies.

For real-time frequency management, we normally begin with long-term predictions of expected performance based on median values of input parameters, i.e., $f_0 F2$, sunspot number, etc. These predictions are then updated with locally measured values of one of the relevant parameters to give a real-time prediction.

In circuit planning applications, we are primarily interested in expected hourly median behavior. Sometimes, these median predictions are augmented with predictions of shorter time-scale behavior. For example, in some field strength predictions, models that predict fading rates and amplitudes due to ionospheric scattering are employed. These variations about a median value may have time scales on the order of minutes or even seconds. However, these models are also based on median behavior determined from extensive statistical analysis of global scattering data. In general, predictions of field strengths on less than an hourly, monthly median basis require sounding of the ionosphere to determine its current state and to monitor its short-term variations.

This report deals with the long-term monthly median prediction of field strength or transmission loss. Consequently, all physical parameters will be assumed to be monthly median values. Also, we will be concerned exclusively with earth-based transmitters and receivers. For the most part this restricts the frequency range to the HF band of 2-30 MHz. Later, we will discuss possible propagation modes at frequencies greater than 30 MHz.

FIELD STRENGTH PREDICTION

When developing a method for prediction of field strength or transmission loss, the ultimate objective is obviously a simple and accurate method. In many instances, the method should also be fast enough for use in real-time applications. In general, there are two approaches that can be followed to produce such a model. One is to fit analytic equations to the experimentally determined dependence of transmission loss on path, time, and frequency. The other approach is to estimate the total transmission loss as the sum of a number of separate mechanisms for energy loss. In this method, each term is an expression deduced either from theory or measurement or both. Both techniques have advantages and disadvantages that must be recognized.

The former method is usually simpler in its implementation but requires an extremely inclusive data base to insure that all observable trends have been included. Even in instances where an adequate data base exists, errors inherent in the fitting process produce corresponding errors in predictions (*Second CCIR Computer-based*, 1978).

The latter method is conceptually more elegant and enables variations to be specified in a physically meaningful manner. However, failure to include an important term can lead to significant error in predictions. Also, the usual tendency is to produce a somewhat more complicated model that may not be justified in terms of the gain in accuracy achieved (*Second CCIR Computer-based*, 1978).

The two field strength models tested and described in this report include examples of both of the above methods. The first model we describe is that used in the program HFBC84, which is the latest version of LIL252-2. This program represents a simplified treatment of the methods established by the International Radio Consultative Committee (CCIR) in its original interim report (*CCIR Interim Method*, 1970), and in later updates (*Second CCIR Computer-based*, 1978). The second method is that used in the Naval Ocean Systems Center (NOSC) PROPHET family of prediction programs. This method is based on an empirical model developed at Forschungsinstitut der Deutschen Bundespost (FTZ) by Beckmann (1967) and further refined by Damboldt (1975).

The HFBC84 version of the CCIR-recommended field strength calculation method is used here because it compares most closely with the philosophy and intent of the PROPHET program to provide relatively fast, simple estimates of

field strength. This speed is achieved in PROPHET by using the FTZ method in conjunction with the MINIMUF algorithm for the maximum usable frequency (MUF) determination. HFBC84 achieves its speed of execution through its considerable simplification of the field strength models employed as compared to its parent programs.

A necessary input to any HF skywave field strength prediction scheme is the basic MUF. For a particular time and circuit, this is defined as the maximum frequency wave that can propagate by ionospheric refraction alone. We begin by describing the two methods for predicting this parameter used in the respective field strength prediction programs mentioned above. The first is a simplified version of the method recommended by the CCIR and used in HFBC84. Next, we outline the MINIMUF-85 algorithm used by PROPHET.

MUF PREDICTIONS

Simplified CCIR Method

For applications where speed is not essential and adequate computer memory is available, a method for predicting the median F2 layer basic MUF based on numerical maps of the ionospheric characteristics $f_o F2$ and $M(3000)F2$ has been developed (*Report to the Second Session, 1984*). Here $f_o F2$ is the F2 layer ordinary wave critical frequency. It represents the maximum frequency wave reflected back to the earth for vertical incidence on the ionosphere. Numerically it is proportional to the square root of the peak electron density of the layer. $M(3000)F2$ is a path length factor that represents the multiplier for the $f_o F2$. The product of $f_o F2$ and $M(3000)F2$ gives $F2(3000)MUF$, the F2 layer MUF for a 3000-km path. Both of these characteristics are scaled from vertical incidence ionograms.

For great circle path lengths, $D(\text{km})$, less than 4000 km, the F2-layer MUF is obtained by first determining $f_o F2$ and $M(3000)$ at the path midpoint for 12-month running mean sunspot numbers of $R_{12} = 0$ and $R_{12} = 100$. The values of these characteristics corresponding to the required R_{12} index are found by interpolation if the required value is between 0 and 100 and by extrapolation if the value is greater than 100. If the required R_{12} value is greater than 150, the value at 150 is used.

We then have

$$F2(0)MUF = f_o F2 + f_H/2$$

$$F2(4000)MUF = 1.1 \cdot f_o F2 \cdot M(3000)F2$$

where f_H is the electronic gyrofrequency at the midpoint of the path. The F2-layer MUF for the path distance D is then found by interpolation according to (*Report to the Second Session, 1984*),

$$F2(D)MUF = F2(0)MUF + [F2(4000)MUF - F2(0)MUF] \cdot M(D)$$

where

$$M(D) = 1.64 \cdot 10^{-7} \cdot D^2, \quad 0 \leq D < 800$$

or

$$M(D) = 1.26 \cdot 10^{-14} \cdot D^4 - 1.3 \cdot 10^{-10} \cdot D^3 + 4.1 \cdot 10^{-7} \cdot D^2 - 1.2 \cdot 10^{-4} \cdot D,$$

$$800 \geq D \leq 4000.$$

For great circle path lengths greater than 4000 km, a simple control point method is employed. Control points are taken at points 2000 km from each end of the path, and at these points the value of $F2(4000)MUF$ is determined, interpolating in R_{12} as required. The lower of these two values is taken as the median F2-layer MUF for the path.

For all path lengths, the F2-layer MUF is calculated according to the above method. For paths between 0 and 4000 km, the median basic MUF of an E-layer mode is also determined. This is done by first determining the E-layer critical frequency, $f_o E$, at the path midpoint for a path of 2000 km or less, or at points 1000 km from each end for a path between 2000 and 4000 km. At these points the solar zenith angle χ is determined and the $f_o E$ is given by (*Report to the Second Session, 1984*)

$$f_o E = 0.9 \cdot [(180 + 1.44 \cdot R_{12}) \cdot \cos \chi']^{0.25} \text{ MHz}$$

where

$$\chi' = \chi, \quad 0 \geq \chi > 80^\circ$$

$$\chi' = 90^\circ - \frac{\exp [0.13 \cdot (116 - \chi)]}{10.8}, \quad 80^\circ \leq \chi < 116^\circ$$

$$\chi' = 89.907, \quad \chi \geq 116^\circ.$$

The E-layer basic MUF for the path, E(D)MUF, is then given by

$$E(D)MUF = f_o E \cdot \sec i_{110} \quad (1)$$

where $f_o E$ is the midpoint critical frequency for paths less than 2000 km and the lesser of the two values for paths greater than 2000 km. Here i_{110} is the angle of incidence of the ray at a height of 110 km assuming mirror reflection in the ionosphere.

For most applications, the F2 layer controls the propagation characteristics on a given path, and the former method based on numerical maps is required. The number of numerical maps required to specify the value of $f_o F2$ and $M(3000)F2$ for each hour of every month at $R_{12} = 0$ on $R_{12} = 100$ is extremely large. Add to this the fact that the median behavior of these characteristics can become quite complicated, and we see that the total number of coefficients required for this method makes it impractical for micro-computer application. Consequently, techniques specifically developed for use on microcomputers are now used in many applications. Next, we describe one of the faster and shorter methods, MINIMUF-85.

MINIMUF-85

MINIMUF-85 is the latest version of the MINIMUF algorithm, which has been described many times in other documents (Rose and Martin, 1978; Sailors et al., 1986). All PROPHET systems, Advanced Classic PROPHET, APES, TDA, etc., use the MINIMUF algorithm to predict monthly median values of the F2-layer MUF. As mentioned earlier, the advantage of the MINIMUF method is its comparably fast execution time, its simplicity, and its ease of transport, which makes it particularly suitable for real-time and field use. Sailors et al. (1981) found it to be extremely accurate considering the simplicity of the method.

In MINIMUF-85, the F2-layer MUF for a path of length D(km) is given by

$$F2(D)MUF = f_o F2 \cdot M(D)$$

where

$$f_o F2 = (6 + A1 \cdot \sqrt{\cos \chi_{eff}})^{1/2} \quad (2)$$

and

$$M(D) = A_2 \cdot A_3 \cdot A_4 \cdot (1 + 2.5 \cdot \sin(2.5 \cdot \Psi))^{3/2} .$$

Here, A_1 and A_2 are linear functions of monthly median sunspot number, A_3 is a sixth-order Fourier series based on season, and A_4 is a function of time, the form of which differs between night and day. The great circle path length corresponding to D , in radians, is Ψ . The model uses a control point method for paths greater than 4000 km similar to that described earlier.

In equation 2, χ_{eff} is an effective solar zenith angle and $\cos \chi_{\text{eff}}$ is modeled as the "response of a linear first-order system driven by the actual $\cos \chi$ " as follows (Rose and Martin, 1978),

$$\tau_D \frac{d}{dt} (\cos \chi_{\text{eff}}) + \cos \chi_{\text{eff}} = \cos \chi .$$

An effective zenith angle is used to simplify the modeling technique since the F2-layer variation, unlike the E layer, is not well represented as a function of zenith angle alone. By using an effective zenith angle and fitting constants in the model to actual measured, oblique-path MUFs, the effect of the other dependencies of the F2 layer can be accounted for without explicit inclusion in the model.

As of this writing, MINIMUF-85 does not include a determination of the E-layer MUF. We anticipate in the future a calculation similar to that used in the CCIR program will be included for short (<2000 km) paths.

A statistical comparison of the accuracy of the above methods for predicting MUFs is shown in table 1. These results are based on a comparison of predicted values with over 13,000 measured oblique sounder MUFs. Table 1 shows that the two methods of MUF predictions are equally accurate for the most part and can be expected to predict, on the average, approximately equal MUFs as input to the individual field strength prediction programs. A more complete comparison of the two MUF prediction methods is presented in a NOSC technical report (Roy and Sailors, 1987).

Table 1. Summary of comparison of MINIMUF-85 and HFBC84 MUF predictions.

<u>Conditions</u>	<u>MUF85</u>	<u>HFBC84</u>
Population size	13,054	13,054
Average residual	1.282	1.165
RMS residual	4.579	4.665
MAE residual	3.451	3.472
Average relative residual	.051	.059
RMS relative residual	.239	.242
MAE relative residual	.180	.179
Average absolute relative residual	.186	.196
Standard error of estimate	3.971	3.885
Correlation coefficient	.819	.827

Next we present a description of the two field strength models. We begin with the methods used in HFBC84 and then present the PROPHET field strength model. A relatively detailed description of the models will be given since these serve to highlight the various mechanisms through which energy is reduced (or increased) for a wave propagating in the ionosphere.

FIELD STRENGTH CALCULATIONS

HFBC84 Method

Path Lengths <7000 km. The method used for these path lengths assumes great circle geometrical ray propagation with reflection from E or F2 layers in a horizontally stratified ionosphere. The restriction to path lengths less than 7000 km is due to the recognition that, while the ionosphere is dominantly horizontally stratified due to the nature of the ionization process, there is also a high degree of variability and fluctuation in the ionization levels present at all times. For a wave passing through this variable medium, the majority of the energy is refracted into the great circle path. However, scattering due to variability in the form of layer tilts or electron density irregularities causes some propagation out of this path. For long path lengths, the wave may pass into the ionosphere four or more times with correspondingly more of its energy scattered out of the great circle path, thus decreasing the received field strength. Likewise, for a given great circle transmission path, energy from adjoint rays that would not

normally be expected to contribute may be scattered to the receiver, causing an increase in the received field strength. As currently modeled, the ray path geometry method of calculation is unable to account for this non-great circle propagation, and other methods are used for longer path lengths where these effects become increasingly important.

The first step in calculating the field strength is determining the MUF for each mode to be included. The minimum hop F2- and E-layer MUFs are calculated as outlined above. The MUF for higher order modes is found, in the case of the E layer, by determining the angle of incidence for a given mode at a height of 110 km. The MUF is then found by multiplying the secant of this angle by the midpath $f_o E$ for paths less than 2000 km or by the minimum $f_o E$ at the two control points for paths greater than 2000 km.

For F2-layer modes, the MUF is found by determining the angle of incidence, assuming mirror reflection, at a height given by the Shimazaki equation (*Second CCIR Computer-based*, 1978)

$$hp = \frac{1490}{M(3000)F2} - 176 \text{ (km)}$$

where $M(3000)$ is calculated at the position of the minimum $f_o F2$ at the two control points for paths greater than 4000 km and at the midpath for paths less than 4000 km. The secant of this angle is then multiplied by the minimum $f_o F2$, or midpath $f_o F2$, to determine the mode MUF. Five modes are calculated for both the E and F2 layers.

Once the MUF for a mode is determined, the median field strength (in dB above $1\mu\text{V/m}$) for that mode is given by

$$E_{Ts} = 136.6 + P_T + G_T + 20 \log f - L_{bf} - L_i - L_g - L_h - L_m - 7.3 . \quad (3)$$

Here $136.6 + 20 \log f$ represents the reference field at 1 km for a wave of frequency f (MHz) for 1 kW input to an isotropic antenna in free space. P_T is the actual power of the transmitter in dB relative to 1 kW and G_T is the gain of the transmitting antenna in dBi in the direction of the ray for the mode. The various loss terms in equation 3 will be dealt with separately.

In general, for paths less than 7000 km, the field strength values of the two strongest F2-layer modes and the strongest E-layer mode are determined according to equation 3. The resultant field strength from these modes is obtained, assuming uncorrelated phases, by power addition. Since multiple-

hop, E-layer modes suffer substantial deviative absorption, these modes are not considered beyond 4000 km (*Report to the Second Session*, 1984). For these distances, only multiple-hop, F2-layer modes are considered.

a. Basic Free Space Loss, L_{bf} . The major source of energy reduction of the wave is usually the free space loss resulting from the geometrical spreading of energy as the radio wave progresses away from the transmitter. As a first approximation, for a one-hop path, the CCIR assumes that the earth and ionosphere are both flat and that reflection is specular (*CCIR Interim Method*, 1970). In this approximation, the energy density diminishes as the inverse square of the ray path distance (no focus gain at these path lengths).

Now for an isotropic antenna in free space transmitting P watts of power, the power flux density at a distance D (km) is $P/4\pi D^2$. For an isotropic receiving antenna in free space, the effective receiving area is $\lambda^2/4\pi$, where λ (km) is the free-space wavelength of the incident wave. Thus, the total power received by an isotropic antenna excited by an isotropic antenna at a distance D is

$$\frac{P}{4\pi D^2} \cdot \frac{\lambda^2}{4\pi} = P \left(\frac{\lambda}{4\pi D} \right)^2 .$$

The basic free-space transmission loss in this case is given by the ratio of power transmitted to power received, or in dB,

$$L_{bf} = 10 \log \left[\frac{P}{P \left(\frac{\lambda}{4\pi D} \right)^2} \right] = 20 \log \frac{4\pi D}{\lambda} .$$

This can be written as

$$L_{bf} = 21.98 + 20 \log D - 20 \log \lambda .$$

Writing λ in terms of the frequency f (MHz) this becomes

$$L_{bf} = 32.44 + 20 \log D + D \log f . \quad (4)$$

This loss is due to spatial expansion of the wave as it leaves the source and it is present in any application. In the case of an earth-based transmitter, the range is the slant path length of the ray through the ionosphere. For an equivalent triangular path, this slant path range is given by

$$d = 2R \cdot \frac{\sin \frac{D}{2R}}{\cos \left(\Delta + \frac{D}{2R} \right)}$$

for a 1-hop path. For an arbitrary n-hop path this becomes

$$d = 2R \sum_{i=1}^n \frac{\sin \frac{D}{2R}}{\cos \left(\Delta + \frac{D}{2R} \right)}$$

where D is the great circle hop length for an n-hop mode and R is the earth's radius. Here Δ is the vertical radiation angle for the mode and is given by

$$\Delta = \tan^{-1} \left[\cot \frac{D}{2R} - \frac{R}{R+h}, \cosec \frac{D}{2R} \right] ,$$

where h' is the equivalent mirror reflection height in the ionosphere determined for the mode. For E-layer modes h' is taken to be 110 km. For F2-layer modes h' is determined at the control point with the minimum value of $f_0 F2$, or the midpath point for paths less than 4000 km. It is given by

$$h' = 358 - (11 - 100a) \left(18.8 - \frac{320}{x^5} \right) + aD \left(0.03 + \frac{14}{x^4} \right) \text{ km}$$

or 500 km, whichever is less. Here a is given by

$$a = \frac{1}{M(3000)F2} - 0.24$$

or 0.04, whichever is greater. X is the ratio of F2-layer critical frequency to E-layer critical frequency, or 2, whichever is larger.

For a fixed distance D, equation 4 shows that the losses increase with frequency. This is an artifact of the assumption of the receiving characteristics of an antenna which is frequency dependent. However, the free-space loss is dependent on distance only, and this term will cancel with a similar term in the reference field and will not appear in the final field strength expression.

b. Ionospheric Absorption Loss, L_i . The next most important field strength reduction mechanism is absorption losses suffered by the wave as it propagates through the ionosphere. These losses come about through collisions, mainly between electrons and neutral particles at D-layer heights and electrons and positive ions at E- and F-layer heights.

As an electromagnetic wave travels through a plasma such as the ionosphere, the electrons in the plasma are accelerated into motion by the electric field vector of the wave. (Here we are assuming that at HF radio frequencies the motion of the much more massive ionic component of the plasma can be ignored relative to the electrons.) In the absence of collisions with other particles of the plasma, the accelerated electrons would reradiate their acquired energy, which would be restored to the passing wave. However, because the electrons have a finite mass, this radiated energy is delayed in time with respect to the exciting wave. This causes a phase difference to develop between the two energy components, resulting in a change in the phase velocity of the total wave and, hence, in the index of refraction. If we include the effects of collisions on the electrons, the above picture is significantly altered. The electrons, set into motion by the wave, collide with other particles and lose some of their acquired kinetic energy to these particles. This results in an overall increase in the effective temperature of the plasma. The energy that goes into heating the plasma is not available to be returned to the passing wave as described above in the "no collision" case. In this way energy is "absorbed" from the wave by the plasma (Davies, 1969).

Mathematically, the absorption process in the ionosphere is described by the imaginary part of the complex refractive index, χ . In terms of χ we define the absorption coefficient, K , as the imaginary part of the complex wave vector,

$$K = \frac{\omega}{c} \chi$$

where $\omega = 2\pi f$ and c is the speed of light in vacuum.

If we initially ignore the earth's magnetic field and assume an isotropic electronic plasma, the dispersion relation is given by Booker (1984)

$$n^2 = (\mu - i\chi)^2 = 1 - \frac{\omega_N^2}{\omega^2 \left(1 - i\frac{\nu}{\omega}\right)}$$

where $\omega_N^2 = \frac{Ne^2}{\epsilon_0 m}$ is the electronic plasma frequency. Then, the absorption coefficient can be written as

$$K = \frac{e^2}{2\epsilon_0 m \mu c} \cdot \frac{N\nu}{\omega^2 + \nu^2} \quad (5)$$

where e is the charge of the electron; ϵ_0 is the free-space permittivity, m is the electronic mass, N is the electron density, and ν is the effective collision frequency.

For an HF wave of frequency f_v launched vertically into an isotropic ionosphere, the total path absorption is given by

$$L(f_v) = 2 \int_{h_o}^{h_v} K dh$$

or

$$L(f_v) = \beta \int_{h_o}^{h_v} \frac{N(h') \nu(h') dh'}{\mu(h') \left\{ f_v^2 + \left[\frac{\nu(h')}{2\pi} \right]^2 \right\}}$$

where β is a constant, h_o is the height of the bottom of the ionosphere, and h_v is the height of reflection.

Equation 5 shows that, for a fixed operating frequency, the absorption coefficient can become large if the product $N\nu$ becomes large or if the index of refraction becomes small while $N\nu$ remains finite. These two limits of equation 5 are used to artificially separate the absorption suffered by an electromagnetic wave into two parts, nondeviative and deviative.

At D-layer heights the local index of refraction is approximately unity at HF frequencies and the wave suffers little refraction. However, at these heights the product $N\nu$ can become large, resulting in a maximum of the absorption coefficient. This is referred to as nondeviative absorption. In this case the absorption coefficient is given by

$$K = \frac{e^2}{8\pi^2 m \epsilon_0 c} \cdot \frac{N\nu}{f_v^2 + \left[\frac{\nu}{2\pi} \right]^2} \quad (6)$$

If the wave frequency f_v is less than the maximum critical frequency (E or F layer) of the ionosphere, the wave will propagate into the ionosphere until it reaches a height at which the plasma frequency is equal to the wave frequency. At this level $\mu = 0$ and the wave is reflected. For usual operative HF frequencies, this occurs in the E- or F-layer region of the ionosphere.

Equation 5 shows that at the level $\mu = 0$ the so-called deviative absorption becomes infinite (since $N\nu > 0$ at all ionospheric heights). This nonphysical result is due to the fact that the geometrical optics approximation upon which the above argument is based is not valid near the turning point for the wave.

At heights near the reflection level, the wave suffers considerable group retardation. Consequently, the wave spends a long time in the absorbing region, exciting an increased number of collisions and causing the total absorption to increase despite the low neutral particle density. At these heights, the collisions involve positive ions instead of neutral particles and the relations become more complex, so we will not pursue the topic here.

In summary, a vertical wave propagating through the ionosphere suffers energy loss through the absorption of the energy by collisions with neutral particles at D-layer heights (nondeviative absorption) and by collision with positive ions (deviative absorption) at E- and F-layer heights. Inspection of equation 5 also shows that this absorption is approximately inversely proportional to the square of the operating frequency for nondeviative absorption.

So far we have ignored the effect of the earth's magnetic field. Since this field greatly affects electromagnetic wave propagation in the ionosphere, especially as the wave frequency approaches the gyrofrequency, we are not surprised to encounter its effect in ionospheric absorption. In fact, a more complete analysis shows we can account for the magnetic field in our earlier results by including the longitudinal component of the gyrofrequency in our initial absorption expression, equation 5, in the following way

$$K = \alpha \frac{N\nu}{\left(f_v + f_L\right)^2 + \left[\frac{\nu}{2\pi}\right]^2} \quad (7)$$

where α is a constant and f_L is the longitudinal component of the electronic gyrofrequency. We can include the earth's magnetic field to this level of approximation (quasi-longitudinal approximation) in all of our analysis in the same way.

Also, in our analysis above, we have been interested in vertical propagation. Clearly, we wish to generalize to oblique incidence applications. This is accomplished by using the Martyn absorption theorem

(Davies, 1969). This theorem states that for a plane-parallel, horizontally stratified ionosphere in the absence of the earth's magnetic field, the absorption $L(f_{ob})$ experienced by a wave of frequency f_{ob} incident at an oblique angle i_o on the base of the ionosphere is related to that experienced by a wave at vertical incidence of frequency f_v by

$$L(f_{ob}) = L(f_v) \cos i_o . \quad (8)$$

Here the waves of frequency f_{ob} and f_v are equivalent in the sense that their true heights of reflection are equal. Under these conditions, the secant law states that (Davies, 1969)

$$f_{ob} = f_v \sec i_o .$$

Substitution of this into equation 8 shows that

$$L(f_{ob}) = \frac{L(f_v) f_v^2}{f_{ob}^2} \sec i_o . \quad (9)$$

This equation is exact for a plane-stratified ionosphere with no magnetic field. When the curvature of the earth and the magnetic field are introduced, the transformation is no longer exact. However, the quasi-longitudinal approximation remains valid. So for a curved earth with magnetic field, we can approximate the nondeviative absorption loss experienced by the oblique wave as

$$L(f_{ob}) = \frac{L(f_v)(f_v + f_L)^2}{(f_{ob} + f_L)^2} \sec i_o . \quad (10)$$

If we further assume that, for the most part, in the HF band we have $f_v \gg \nu$, we can use equation 7 to give

$$L(f_{ob}) \approx \frac{A_i \sec i_o}{(f_{ob} + f_L)^2} \quad (11)$$

where A_i is a measured index of the absorption experienced by the vertical wave of frequency f_v , which is equivalent to f_{ob} in the above sense.

For the HFBC84 program, a semiempirical approximation to the above result has been developed. Guided by the form of equation 11, measurements on a series of oblique paths have led to the following approximation for the nondeviative absorption loss term

$$L_i = \frac{677.2 \sec i_o}{(f + f_H)^2 + 10.2} \sum_{j=1}^n I_j \quad (12)$$

where

n = number of hops for the mode

i_o = angle of incidence at 100 km

f = operating frequency (MHz)

f_H = full gyrofrequency at 100 km

and

$I_j = (1 + .0037 \cdot R_{12})(\cos 881 x_j)^{1.3}$ where R_{12} is the 12-month running mean sunspot number and x_j is the solar zenith angle at the point of passage through a height of 100 km for each hop.

At night, the ionization density of the layers decreases and the absorption does not cease but falls off to a small residual value. To approximate this behavior, the value of I_j is restricted to be greater than 0.1. This assumption agrees with the work of Wakai (1961) on nighttime absorption (Lucas and Haydon, 1966).

Finally, we note that the absorption expression of equation 12 is meant to describe the median level that can be expected to exist. It is not meant to be used during times of anomalous solar activity, i.e., solar flares, when the high X-ray flux levels emitted by the sun can cause extreme levels of D-region absorption. As we mentioned earlier, since nondeviative absorption is inversely proportional to the square of the operating frequency, this increased level of absorption can cause the minimum available operating frequencies to rise to the level where it actually reaches the MUF. During this "shortwave fade" period, no skywave is available for communication. Behavior of this sort must be included independently in separate absorption models derived to handle these effects.

c. Ground Reflection Loss, L_g . For multiple-hop paths, the third major source of energy loss is that due to intermediate ground reflection. Assuming the wave incident at the ground is randomly polarized with energy equally distributed in horizontal and vertical polarization, the loss is given by (CCIR Interim Method, 1970)

$$L_g = 10 \log \left(\frac{|R_v|^2 + |R_h|^2}{2} \right) \quad (13)$$

where R_v and R_h are the vertical and horizontal polarization Fresnel reflection coefficients, respectively. They are defined as the ratio of the magnitude of the electric vector in the reflected wave to that of the incident wave. R_v and R_h are, in general, complex and are given by the Fresnel formulae

$$R_v = n^2 \sin \beta - (n^2 - \cos^2 \beta)^{1/2}$$

$$R_h = \frac{\sin \beta - (n^2 - \cos^2 \beta)^{1/2}}{\sin \beta + (n^2 - \cos^2 \beta)^{1/2}}$$

where β is the angle of the reflected wave at the earth and n is the complex refractive index of the earth.

In the HFBC84 program, these calculations are not performed since it has been determined that, to an acceptable level of accuracy, a value of 2 dB can be assigned for each ground reflection. Thus, we have

$$L_g = \begin{cases} 0, & \text{for 1-hop mode} \\ 2 \text{ dB}, & \text{for 2-hop mode} \\ 4 \text{ dB}, & \text{for 3-hop mode} \\ (n - 1) \cdot 2, & \text{for } n\text{-hop mode.} \end{cases} \quad (14)$$

d. Auroral Absorption, L_h . The absorption processes in auroral regions are somewhat different than those encountered at lower latitude. At high latitude (north and south), the principal ionization process is particle precipitation. The particle flux from the sun is carried along the earth's magnetic field lines and deposited at ionospheric heights in extremely complex patterns at the earth's magnetic poles. This flux of particles causes ionization through both collision and radiation processes. While there may be some solar control of the ionization level at these latitudes (i.e., through x , the solar zenith angle as in equation 12) particle precipitation is the major influence in polar regions.

The method for inclusion of these processes in the CCIR program is through a table of experimentally determined values which are added to the

resultant field strength (*Report to the Second Session, 1984*). This table contains dependence on path length, time, season, and geomagnetic latitude. The table also includes some small low- and mid-latitude corrections used to include effects not explicitly included in the loss terms of equation 3. In general, the values in the table peak at polar latitudes with values from 3 to 10 dB.

The next loss mechanism given in equation 3 is the over-the-MUF loss, L_m . We postpone discussion of this term until we have introduced the long path model used in HFBC84.

The numerical factor of 7.3 subtracted from equation 3 is included to account for "those effects of skywave propagation not otherwise included in this fast, simple method" (*Report to the Second Session, 1984*). It is subject to change as further comparison to measured data is completed.

The calculations outlined above are repeated for each successive higher order F2 mode until a peak in the field strength is found. Then, the two highest field strength modes are selected.

For E-region modes, the lowest order mode is a 1E for ranges of 0-2000 km and 2E for 2000-4000 km. For paths less than 4000 km, the highest field strength mode is found according to the above methods and the result is added, as power, to the two strongest F2 layer modes. The result is the predicted field strength for that frequency and hour.

Path Lengths Between 7000 and 9000 km. For paths between 7000 and 9000 km, the ray path geometry procedure for F2-layer modes is used in conjunction with the method for long paths (>9000 km) to be described below. The results from the two methods, E_{ts} and E_{tl} , are combined as follows

$$E_{ti} = E_{ts} + \frac{D - 7000}{2000} (E_{tl} - E_{ts}) \quad (15)$$

where D is the path length. This expression gives the predicted field strength in these cases.

As already mentioned, the assumptions of geometric ray propagation are not valid for long path lengths. At these distances the easiest procedure is to use an empirical model which, hopefully, has been constructed from a data base containing examples of all the loss mechanisms accounted for in the short-path model plus those losses unique to long-path propagation. The only way we can ascertain whether the model contains all the loss mechanisms is by

comparing predictions against actual measured data. The results of such a comparison appear later in this report, but, first, we describe the empirical model tested.

Path Lengths Greater Than 9000 km (the FTZ Model). The FTZ method of field strength calculation was developed by Beckmann (1967) and has been continually refined by the work of Damboldt (1975) at FTZ. At these path lengths, the effects of ionospheric tilts and scattering from irregularities cause contributions to the measured field strength from paths outside the main great circle path. These effects also complicate assigning an antenna gain to a particular path since energy may be received from many azimuths. These considerations have led to the development of the following empirical model, which is used by the CCIR for paths greater than 9000 km and is used, in an altered form to be described later, for all path lengths by PROPHET programs.

Another propagation mode that is always present to some degree is at frequencies exceeding the MUF for the path. The ray path geometry methods described earlier would predict that a ray at such a frequency would penetrate the ionosphere and, thus, not be received by a ground-based receiver. It has been found experimentally however that usable field strength is available at frequencies that exceed the MUF. Some factors that contribute to this phenomenon are forward scatter via F reflection, lateral ground scatter from great circle paths with a higher F2-layer MUF, sporadic-E scatter, supermodes, and extremely long Pederson (high angle) rays (Beckman, 1967).

Beckmann determined that the measured field strength was a function of both the lowest usable frequency (f_L) for the path, which he defines as that frequency for which the field strength is some low limiting value, and the MUF. Experiments showed that the field strength rises with frequency from f_L to a peak at some intermediate frequency somewhat below the MUF and then decreases to the same low limiting value at a frequency somewhat greater than the MUF, which he calls the operational MUF. The operational MUF (f_o) is obtained as the product of a numerical factor, determined from geographical and diurnal characteristics of the path, times the MUF. The $f_L - f_o$ combination then defines the transmission frequency range (TFR) for the path, or that range of frequencies for which usable field strength may exist, depending on system parameters such as noise level and receiver sensitivity.

a. FTZ Long-Path Model. Given the above behavior of the field strength with frequency, Beckmann (1967) used the following equation

$$E_{t\ell} = F_o \left(1 - \frac{(f_L + f_H)^2}{(f + f_H)^2} \right) \quad (16)$$

to represent the rise of field strength, with frequency, from f_L . Here F_o is the free-space field strength given by

$$F_o = 20 \log \frac{3 \times 10^5 / \text{Perp}}{d}, \quad (17)$$

where Perp is the effective radiated power in kilowatts and d is the slant path range in kilometers for mirror reflection from a height of 300 km.

Equation 16 is exactly valid for nondeviative absorption and can be derived in the following way. As we saw earlier, the D-region (nondeviative) absorption is inversely proportional to the square of the operating frequency. At low frequencies, the D-region absorption is greatest and is the dominant factor in determining operational frequencies. So we can approximate the field strength at the low frequencies by

$$E_{t\ell} = F_o \cdot L_i \quad (18)$$

where L_i is the ionospheric absorption discussed earlier. Now from equation 11, L_i has the approximate form for oblique propagation

$$L_i \approx \frac{A \sec i_o}{(f + f_H)^2}, \quad (19)$$

where we have replaced the longitudinal component of the gyrofrequency with the full gyrofrequency, which introduces only a slight error. We then define f_L as the frequency that produces a field strength of 0 dB ($\mu\text{V}/\text{m}$) for 10^3 kW effective radiated power. Equation 18 then becomes

$$0 = F_o (10^3 \text{ kW}) - \frac{A \sec i_o}{(f_L + f_H)^2} \quad (20)$$

or

$$F_o (10^3 \text{ kW}) (f_L + f_H)^2 = A \sec i_o. \quad (21)$$

Putting this expression into equation 19, equation 18 becomes

$$E_{t\ell} = F_o (10^3 \text{ kW}) \left(1 - \frac{(f_L + f_H)^2}{(f + f_H)^2} \right).$$

Although exact for nondeviative absorption, use of this expression in general is adequate since at low frequencies nondeviative absorption dominates other loss mechanisms.

To include the effects of the operational MUF in the field strength, Beckmann (1967) introduced the following changes in equation 16 to produce the decline in field strength with frequency from the peak

$$E_{t\ell} = F_o \left[1 - C \left(\frac{(f + f_H)^2}{(f_o + f_H)^2} + \frac{(f_L + f_H)^2}{(f + f_H)^2} \right) \right] \quad (22)$$

where

$$C = \frac{(f_o + f_H)^2}{(f_o + f_H)^2 + (f_L + f_H)^2} .$$

Note this expression for field strength satisfies the requirement that for $f = f_L$ and $f = f_o$ the field strength for 10^3 kW effective radiated power is 0 dB. The field strength peaks at a frequency f_p given by the geometric mean of f_L and f_o ,

$$f_p = \sqrt{(f_L + f_H)(f_o + f_H)} .$$

To derive the expression for the field strength from f_L to the peak, we assumed an effective radiated power of 1000 kW. Equation 22 can be adjusted for arbitrary power levels and antenna gains by including the actual power level used and by addition of the transmitter antenna gain. For example, for 100 kW radiated power we have

$$E_{t\ell} = (139.6 - 20 \log d) \left[1 - C \left(\frac{(f + f_H)^2}{(f_o + f_H)^2} + \frac{(f_L + f_H)^2}{(f + f_H)^2} \right) \right] - 14.8 + G_T$$

where G_T is the maximum transmitting antenna gain in dB in the range of 8° to 10° elevation angle. Since Beckmann originally used a reference field due to an isotropic antenna over perfect ground, which has a gain of 4.8 dB with respect to an isotropic antenna in free space, 4.8 is subtracted to go from effective radiated power to radiated power.

Likewise, the field strength for a 1-kW transmitter would be

$$E_{tl} = (139.6 - 20 \log d) \left[1 - C \left(\frac{(f + f_H)^2}{(f_o + f_H)^2} + \frac{(f_L + f_H)^2}{(f + f_H)^2} \right) \right] - 34.8 + G_T .$$

In general, for arbitrary radiated power, we have

$$E_{tl} = (139.6 - 20 \log d) \left[1 - C \left(\frac{(f + f_H)^2}{(f_o + f_H)^2} + \frac{(f_L + f_H)^2}{(f + f_H)^2} \right) \right] - 4.8 + G_T \\ + 10 \log \left(\frac{P_T}{1000} \right) \quad (23)$$

where P_T is the transmitted power in watts.

The operational MUF used by Beckman has been changed to include more geographical and diurnal effects by Damboldt (1975). The constants that appear in the expression below have been changed, and continue to change, as comparison with data warrants. For completeness, we also describe the FTZ extension to paths less than 7000 km, although this is not used in the HFBC84 program.

The current expression for the operational MUF is (Bradley and Liu, 1982)

$$f_o = K \cdot \text{MUF}$$

where, for E-layer modes, $K = 1$. For F2-layer modes

$$K = k_o \left[1.2 + W \cdot \left(\frac{f_g}{f_{g,\max}} \right) + X \cdot \left(\left(\frac{f_{g,\max}}{f_g} \right)^{1/3} - 1 \right) + Y \cdot \left(\frac{f_{g,\min}}{f_{g,\max}} \right)^2 \right] \quad (24)$$

with $k_o = 1$ for total path ground range, D , greater than 3600 km and

$$k_o = 1.25 + .25 \cos \left[3.935 \ln \left(\frac{D + 1500}{1500} \right) - 2 \right]$$

for $D < 3600$ km.

In equation 24, f_g , $f_{g,\max}$, and $f_{g,\min}$ are, respectively, the MUF for the hour of interest and the maximum and minimum MUF for the 24-hour day. W , X , and Y are empirical constants, which are functions of raypath azimuth at the

midpath point derived by linear interpolation with angle between $W = .1$, $X = 1.2$, $Y = 6$ for east-west paths and $W = .2$, $X = .2$, $Y = .4$ for north-south paths.

To determine the operational MUF for a particular path, the general technique is as follows: first, the ionospheric reflection positions of the least order, equal hop length F mode having a hop length of less than 3600 km are determined, along with those of the least order, equal hop length E-mode with a hop length of less than 1800 km. If the ground range will support the single-hop F mode, the ionospheric reflection is taken at the midpath and K is determined at that point. Otherwise, four control points are defined, each being a position of ionospheric reflection for the E and F modes closest to the transmitter and receiver. At each control point the K factor is determined by the above method, and the operational MUF for the hop is determined at each control point. Then the larger of the two operational MUFs is chosen as the value for the path. The minimum of these two values is used as the value of f_o for the path at that hour (Bradley and Liu, 1982).

The other input to the field strength expression is the frequency f_L . Referring to equation 20 we have

$$f_L = \left(\frac{A \sec \phi}{F_o} \right)^{1/2},$$

and we see that the f_L depends on the ionospheric absorption loss term. Since Beckmann originally developed the technique, the actual equation used has changed several times, again as new developments have demanded (Damboldt, 1975). The form of the equation is, however, still that given in equation 19. Currently, the expression used for the daytime f_L in the FTZ models, for path lengths greater than 2000 km (Bradley and Liu, 1982), is

$$f_L = \left[(5.3 + I) \left(\frac{1 + .009R_{12}}{20 \log \left(\frac{3.5 \cdot 10^5}{d} \right) \cos \phi} \right)^{1/2} \cdot \left(\sum_{i=1}^N \sqrt{\cos \chi_i} \right)^{1/2} \cdot f_H \right] \cdot w \quad (25)$$

where for F and E modes alike:

I = seasonal factor with values in the range of 1.0 to 1.1, depending on the transmitter/receiver latitude combination and month

R_{12} = 12-month running mean sunspot number
 ϕ = angle of incidence at 90 km, assuming mirror reflection from 300 km
and hop span D for the great circle path ray
d = slant path length for mirror reflection from 300 km
N = number of legs of least order mode (twice the number of hops)
 x_i = solar zenith angle at a height of 90 km where the i th leg of the
raypath achieves a height of 90 km
W = winter anomaly term determined at path midpoint
W is unity for geographic latitudes of 0° to 30° and at 90° , and peaks at
 60° latitude with values ranging from 1.0 to 1.30 depending on season. If
some of the hop legs are in darkness, x_i is taken as 90° in the summation for
those legs (Bradley and Liu, 1982).

At night the solar-driven ionization process ceases and the absorption is greatly reduced. During this period, the frequency f_L is given by

$$f_{LN} = \frac{D}{\sqrt{3000}}$$

where D is ground range in km. For the evening transition hours, f_L is assumed to fall exponentially with time from a value $f_L = 2 f_{LN}$ at a reference time T to twice the nighttime value, as

$$f_L = 2 f_{LN} \exp[-.23(t - T)]$$

giving a decay to f_{LN} in roughly 3 hours (Bradley and Liu, 1982).

This completes the specification of the FTZ long-path model. As mentioned above, the CCIR recommends use of this method exclusively for paths greater than 7000 km. At these long distances, we are also liable to see focusing of energy due to layer tilts and irregularities. This results in an increase of measured field strength. This effect is included in HFBC84 with the addition of a term, G_{ap} , to equation 23. For propagation to distances D (great circle distance) greater than $\pi R/2$, where R is the earth's radius, focusing is taken into account through the formula

$$G_{ap} = -20 \log \left(\left| 1 - \frac{n\pi R}{D} \right| \right) \text{ dB}$$

for

$$\left(\frac{2n-1}{2} \right) \pi R \geq D \geq \left(\frac{2n+1}{2} \right) \pi R, \quad n = 1 \text{ and } 2.$$

As G_{ap} tends to infinity for $D = n\pi R$, its value is limited to 30 dB (Report to the Second Session, 1984).

FTZ originally used the model we have outlined for all path lengths, and all PROPHET programs now use a modified version of the model. Recently, however, FTZ has developed an improved model for paths less than 2000 km and, together with the above long-path model, covers the entire range of path lengths. Although this model is not implemented in HFBC84 or PROPHET, we present it here for reference and as a possible addition to future PROPHET field strength prediction models.

b. FTZ Short-Path Model. The form of the model for short paths (<2000 km) is similar to the long-path model with the following modifications. An important input is the frequency f_{MAX} at which the field strength is a maximum. This frequency is given by (Bradley and Liu, 1982)

$$f_{MAX} = f_g \left(1 - .24 \frac{f_{g,min}}{f_g} \right) \cdot \frac{D}{3000 f_L^2} \quad (26)$$

where f_g is the MUF for the 1-hop E or F2 mode to ground range D, whichever is greater. Note that $D/3000$ is the square of the nighttime f_L .

The operational MUF is given by

$$f_o = \frac{f_{MAX}}{.35 \left(\frac{D}{2000} \right) + .24 - .5 \left(1 - \left[\frac{f_{MAX}}{f_{g,MAX}} \right]^{1/2} \right)} ,$$

and again we have different equations for f_L depending on time of day.

For daytime periods, the f_{LD} is given by

$$f_{LD} = 1.1 \cdot \sqrt{1 - 0.003 \cdot R12} \cdot f_L$$

where f_L is the daytime f_L used for the long-path model assuming a 1-hop F2 mode reflected from a height of 300 km. For nighttime and evening transition hours, the methods outlined for the long-path model are used with the above expression for the daytime frequency f_L , replacing the earlier expression in the calculation of the evening transition f_L .

The field strength for $f < f_{MAX}$ is then given by

$$F = \left(\frac{f - f_L}{f_{MAX} - f_L} \right) \left(\frac{f_{MAX}}{f} \right) \cdot F_o \cdot \left[1 - \frac{f_L + \left(\frac{D}{2000} \right)^2}{f_{MAX} + \left(\frac{D}{2000} \right)^2} \right] - 4.8 + G_T + 10 \log \left(\frac{P_T}{1000} \right)$$

and for $f > f_{MAX}$ we have

$$F = \left(1 - \frac{f - f_{MAX}}{f_o - f_{MAX}} \right) \left(\frac{f_{MAX} + f/2}{f + f/2} \right) \cdot F_o \cdot \left[1 - \frac{f_L + \left(\frac{D}{2000} \right)^2}{f_{MAX} + \left(\frac{D}{2000} \right)^2} \right]^2 - 4.8 + G_T + 10 \log \left(\frac{P_T}{1000} \right).$$

The parameters G_T and P_T are the same as in the long-path model.

Over-the-MUF Field Strength Model. As mentioned earlier, the observed field strength does not abruptly vanish as the operating frequency begins to exceed the basic MUF for a path. In fact, measurable field strengths are frequently observed at frequencies two or more times the MUF.

If we ignore MUF prediction errors and the monthly median nature of the parameters involved, we can identify several factors that can contribute to this over-the-MUF propagation. Some of these mechanisms are blanketing sporadic E layers that support skywave propagation at higher frequencies, ground scatter from off great circle paths that may have larger MUFs, and forward scatter via F-layer reflection (Beckmann, 1967).

As the operating frequency rises, some field strength reduction is noticeable even at frequencies below the path MUF. This is because frequencies near the MUF penetrate deeper into the reflecting layer and are subject to more scattering out of the great circle path. The peak field strength is then seen at a frequency somewhat below the MUF.

There is experimental evidence that the rate of decrease of field strength at frequencies greater than the MUF may also be dependent on path length (Dieminger and Rose, 1961). This is because for a longer path length a wave is more likely to encounter ionization density irregularities and ionospheric tilts. So there is an increased capability for energy at higher frequencies to be scattered to the receiver. This results in measurable field strength at increased frequencies and a slower roll-off with frequency from the peak field strength.

Overall then, we can have usable field strength at frequencies greater than the path MUF, although the level of the field strength is highly variable. This variability depends on the state of the ionosphere, the length of the path, and, possibly, on terrain in the case of ground scatter.

Some of these considerations are inherent in the empirical FTZ method of field strength prediction. By employing the operational MUF, recognition is given to the fact that there is propagation at these higher frequencies. Some controversy remains, however, as to the correct form this roll-off in field strength takes in this model. We shall have more to say on this subject in the discussion section.

In our earlier discussion of the HFBC84 model for paths less than 7000 km, we did not discuss the over-the-MUF loss term in equation 3. We now take up this topic and present the model used in that program. This model, as are most over-the-MUF loss calculations, is based on the Philips-Abel theory (Wheeler, 1966).

In this theory, the reflecting layers are considered to be composed of individual ionization patches. Each patch consists of subpatches with varying ionization levels, for each of which there exists a classical MUF. The median of the MUFs for the subpatches is the MUF for a patch. The number of patches supporting wave reflection falls with increasing frequency and so there is no abrupt signal cutoff (Wheeler, 1966).

Wheeler (1966) has suggested that for a wave of frequency f greater than the MUF, the median signal power can be taken as proportional to the number of patches of F-region ionization that support transmission at f . That is, proportional to the number of patches such that $f < \text{MUF}$. With the frequency distribution of the MUFs of the sub-patches taken to be Gaussian we have (Report by the Chairman, 1975)

$$L_m = \log P \text{ dB} \quad (27)$$

where

$$P = 1 - \frac{1}{\sqrt{2\pi}} \int_{-\infty}^x \exp\left(\frac{-x^2}{2}\right) dx$$

and $x = \frac{f - \text{MUF}}{\sigma}$. Here σ is the standard deviation of the MUF distribution given by

$$\sigma = .78 (F_u - 1) \cdot \text{MUF}$$

where F_u is the 90-percentile (highest possible frequency (HPF)) factor for the MUF distribution (Barghausen et al., 1969), and the MUF is the median value predicted by the methods presented earlier.

A much simplified method based on the model described above is used in HFBC84. This method is based on a fit to a limited set of over-the-MUF data collected by Wheeler (Bradley et al., 1982). The loss term is given by

$$L_m = 130 \left(\frac{f}{MUF} - 1 \right)^2 \text{ dB} \quad (28)$$

and is not allowed to become larger than 85 dB. There is some question as to the accuracy of this simple method, and we will have more to say on this subject in the discussion section.

This completes the specification of the HFBC84 field strength model. We have given a detailed description to point out the various mechanisms for energy reduction that contribute to the field strength.

The parent program of HFBC84 contains a more elaborate ionospheric loss calculation and also contains several more loss terms in the field strength equation (polarization loss, E_s obscuration loss, etc.) (*Second CCIR Computer-based*, 1978). Since they are not included in HFBC84, we will not discuss them here. The reader wishing information about these loss mechanisms is directed to the aforementioned reference.

Next we describe the field strength model used in the PROPHET family of propagation prediction programs. This model is based on the FTZ method, which we have already described. In this case, the FTZ model, or the modified version of it used in PROPHET, is used at all path lengths. Further, all references to the MUF will be understood to refer to that value predicted by the MINIMUF algorithm. Since there is currently no E-layer model in PROPHET, these values will refer to F2-layer MUFs only.

PROPHET Field Strength Model

The model employed here is the same as that presented for the long-path method used in HFBC84, with several modifications.

The model employed in PROPHET uses the ionospheric absorption index used in the QLOF routine in PROPHET. This is an empirical LUF prediction program and uses an ionospheric absorption term based on the work of Schultz and

Gallet (1970) to predict that parameter. The expression used in QLOF, which replaces the index A_i in equation 11, is

$$A_i = A \left(\frac{CH(921.0, x)}{CH(921.0, (\phi_s - \phi))} \right)^{-2.0 \cdot M}$$

where

$$A = 286 \cdot W \cdot (1.0 + .5|\phi|) \cos^N(\phi_s - \phi) . \quad (29)$$

Here CH is the Chapman function, ϕ_s is the subsolar geographic latitude, ϕ is geographic latitude, and x is the solar zenith angle measured at ϕ . W is a winter anomaly term defined by

$$W = 1.0 + 0.0275[30.0 - |(60 - |\phi|)|] ,$$

M is defined by,

$$M = \begin{cases} .5 (.58 + (|\phi|/18.0).08) & , \quad 0 \leq |\phi| \leq 18^\circ \\ .5 (.66 + .22(|\phi| - 18.0)/6.0), & 18^\circ \leq |\phi| \leq 24^\circ \\ .44 & , \quad |\phi| > 24^\circ \end{cases}$$

and

$$N = \begin{cases} 1.4 - |\phi|/2.44 & , \quad |\phi| < 25.8^\circ \\ .3 & , \quad 25.8^\circ \leq |\phi| < 62.3^\circ \\ (|\phi| - 62.3^\circ)1.07 + .3, & 62.3^\circ \leq |\phi| < 78.3^\circ \\ 0 & , \quad |\phi| \geq 78.3^\circ \end{cases}$$

For paths less than 4000 km, all calculations are done at a single control point, the path midpoint. For paths greater than 4000 km, control points are established at the midpoint and at points 1000 km from each end point. A_i is then determined at each control point, and the average of these values determines the absorption index for the path. A more detailed description of QLOF is available in Argo and Hill (1977) and Sailors and Moision (1987).

The LUF-MUF combination defines the rise in field strength with frequency up to the MUF, as outlined earlier. Now we must determine the operational MUF, which appears in the FTZ model and relates to the field strength we observe at frequencies larger than the MUF.

As we have discussed above, the field strength measured at frequencies greater than the MUF is due to various scattering mechanisms, both in the ionosphere and on the earth's surface. As such, the Wheeler method of predicting over-the-MUF loss, which we described earlier, bears no physical connection to the true causes of this type of propagation. It does, however, provide a convenient means of treating this phenomenon in terms of the relevant parameter, i.e., frequency to MUF ratio.

The data on which the empirical PROPHET field strength model and the FTZ model are based were collected over a number of years at the FTZ facility. Since there is likely to be geographic dependence in over-the-MUF propagation phenomenon, we believe the operational MUF determination used in the FTZ model may contain aspects that are specific to that site.

For these reasons, a simplified method of determining the operational MUF has been implemented in the PROPHET field strength calculation. As in the Wheeler method, we assume that the MUF value at a given time, season, geographic position, and sunspot number is a statistical parameter and has a Gaussian distribution around a mean. This mean value is that predicted by MINIMUF. Given this assumption, the operational MUF in PROPHET is determined by the product of the MUF and the 99.1 percentile value of the MUF distribution

$$f_o = 1.85 \cdot (\text{HPF}) \cdot \text{MUF},$$

where HPF is the 90-percentile value factor for an assumed Gaussian MUF distribution (Barghausen et al., 1969). This technique for determining f_o provides a value that is somewhat between the two methods outlined earlier in its philosophy. Its adequacy for determining f_o and, hence, for predicting field strength at frequencies greater than the MUF will be discussed in the data comparison results presented next.

With these differences, the field strength calculation in PROPHET is the same as that described for the long-path model in HFBC84.

FIELD STRENGTH DATA BASE AND SCREENING PROCEDURE

For the comparison of predicted values to measured data, we employed a statistical data screening program, DASCR3, which has been described in several previous NOSC technical reports (Sailors et al., 1981 and 1986). This program allows the data base to be separated at run time into blocks that satisfy certain screening conditions. In this way we can delineate subsets of a large data base for independent testing. Using this feature of the program, we partitioned the data base into blocks corresponding to path length ranges, sunspot ranges, time ranges, etc. These were then screened separately to test accuracy under these conditions.

The data base used in this analysis is a modified version of CCIR Data Base C. It consists of 12,277 median skywave field strength (dB above $1 \frac{\mu V}{m}$) data values normalized to 1 kW erp. This differs from the full Data Base C in that all "long paths" have been removed. These are paths for which the radiowave travels the long way around the world. This was done because PROPHET does not currently have the option to calculate field strength on that type of path.

Table 2 gives a complete summary of the measured data set used in this analysis. Shown here are circuit identification number, transmitter and receiver site names and geographic coordinates, midpath latitude, azimuth from transmitter to receiver, path length, number of path hours, and frequencies for each circuit. We include circuit number and midpath latitude for later referral, as these are variables used as a means to partition the data base for screening.

The data, collected from 1964 to 1984, represent almost two complete solar cycles and contain data samples representing 12-month running mean sunspot numbers in the range 13 to 165.

For each circuit in table 2 there are, in general, several frequencies for which data were obtained, and these are also indicated. In some instances, the frequency was greater than the MUF determined for that circuit-time combination. Thus we could, to some extent, separately investigate the over-the-MUF models used by the respective programs. Since there are differences in the MUF prediction routines, a particular frequency may be over the MUF for one model and under the MUF for the other. Thus, population sizes will differ between models in these comparison results.

Table 2. Summary of transmission circuits contained in the field strength data base.

ID	TRANSMITTER	RECEIVER	TAT	TION	MAT	RAT	RION	AZIM	RANGE	HOURS	FREQUENCIES (MHz)
1	LUXEMBURG	BOCKHACKEN	49.4	-6.2	50.2	51.1	-7.2	20.3	175	54	6.1
2	SANWA	AKITA	36.1	-139.5	37.8	39.4	-140.1	7.8	396	380	5.0
3	KOCANEI	AKITA	35.4	-139.3	37.4	39.4	-140.1	8.6	454	960	5.0
4	KURSEONG	CALCUTTA	26.5	-88.2	24.4	22.3	-88.2	179.8	497	4	7.2
5	BRACKNELL	NORDEICH	52.0	1.1	52.8	53.3	-7.1	75.2	585	1169	4.8, 8.0, 11.1, 14.4, 18.3
6	BRACKNELL	BOCKHACKEN	52.0	1.1	51.6	51.1	-7.2	100.6	595	50	8.0
7	ALOUTS	BOCKHACKEN	47.0	-2.0	49.1	51.1	-7.2	39.7	597	58	6.2
8	OSLO	NORDEICH	59.3	-10.4	56.3	53.3	-7.1	197.0	686	415	6.4, 12.7, 17.1, 22.4
9	OSLO	ILIECHOW	59.3	-10.4	55.9	52.6	-11.1	176.3	718	89	6.4, 12.9, 16.9, 22.4
10	BRACKNELL	ILIECHOW	52.0	1.1	52.5	52.6	-11.1	85.7	847	967	4.8, 8.0, 9.2, 11.1, 14.4, 18.3
11	XIAN	BEIJING	34.1	-108.5	36.9	39.6	-116.3	48.5	925	12	7.3
12	HYDERABAD	TRIVANDRUM	17.2	-78.3	12.7	8.3	-76.6	190.8	999	12	4.8
13	SANWA	WAKANAI	36.1	-139.5	40.7	45.2	-141.4	8.9	1035	170	5.0, 8.0
14	BEIJING	SHANGHAI	39.6	-116.3	35.4	31.1	-121.3	154.2	1069	145	4.8, 5.0, 6.2, 7.3, 9.7, 11.7, 12.0
15	FLEUCHOW	ILIECHOW	50.2	4.5	51.7	52.6	-11.1	76.4	1139	246	6.4, 12.8, 16.9, 22.4
16	XIAN	SHANGHAI	34.1	-108.5	32.8	31.1	-121.3	105.5	1221	108	7.1, 7.3, 11.7, 15.3
17	DERBY	ALICE SBR.	-17.2	-123.4	-20.3	-23.3	-133.4	123.2	1253	154	6.8, 13.6
18	BOMBAY	TRIVANDRUM	19.1	-72.5	13.7	8.3	-76.6	159.9	1272	2	11.8
19	SHANNON	ILIECHOW	52.4	8.5	52.9	52.6	-11.1	89.2	1347	312	5.5
20	PORT	BOCKHACKEN	61.3	-21.5	56.4	51.1	-7.2	217.1	1455	39	6.1
21	ALGER	BOCKHACKEN	36.4	-3.1	43.8	51.1	-7.2	11.1	1635	4	7.2
22	ERIALA	CALCUTTA	7.1	-79.5	14.7	22.3	-88.2	28.6	1930	6	11.8
23	MESIRAH	DEHLI	20.4	-58.5	24.7	28.4	-77.1	64.3	2056	35	12.0, 15.3, 17.8
24	ANKARA	CHATTOYAYE	39.5	-30.4	43.6	46.5	-6.6	292.1	2057	6	15.2
25	KAVALLA	CROWSLEY HK	40.6	-24.2	46.6	51.3	-6	302.8	2255	2	11.7
26	MASIRAH	TRIVANDRUM	20.4	-58.5	14.5	8.3	-76.6	124.8	2365	8	12.0, 15.3
27	ANKARA	JURBISSE	39.5	-30.4	45.7	50.3	-3.6	300.5	2389	8	15.2
28	ERIALA	DEHLI	7.1	-79.5	17.7	28.4	-77.1	353.9	2420	3	15.1
29	PHO	BEIJING	16.4	-120.2	28.0	39.6	-116.3	351.8	2621	11	9.6, 17.8
30	TINANG	TRIVANDRUM	15.2	-120.4	27.4	39.6	-116.3	351.7	2765	53	9.6, 11.7, 12.0, 15.4
31	MAHE	CALCUTTA	-4.4	-55.3	2.0	8.3	-76.6	59.0	2795	12	15.3
32	KRANTJ	TRIVANDRUM	1.2	-103.4	11.9	22.3	-88.2	325.0	2873	5	9.7, 11.7
33	KRANTJ	TRIVANDRUM	1.2	-103.4	4.9	8.3	-76.6	284.9	3064	14	9.7
34	JEZELALM	CROWSLEY HK	32.0	-34.5	43.0	51.3	.6	308.3	3611	10	9.4
35	TEHERAN	ILIECHOW	35.4	-51.3	45.8	52.6	-11.1	302.8	3665	89	15.1
36	TEHERAN	BOCKHACKEN	35.4	-51.3	45.4	51.1	-7.2	298.0	3886	106	9.0, 15.1
37	TEHERAN	NORDEICH	35.4	-51.3	46.5	53.3	-7.1	302.0	3945	488	9.0, 15.1
38	KRANTJ	DEHLI	1.2	-103.4	15.2	28.4	-77.1	317.9	4139	23	9.7, 12.0, 15.4
39	KRANTJ	BEIJING	1.2	-103.4	20.5	39.6	-116.3	16.5	4474	65	6.2, 9.7, 12.0, 15.4
40	ZACKVILLE	BALDOCK	45.5	64.2	53.4	52.0	.1	79.8	4582	1	17.9
41	KUWAIT	CROWSLEY HK	29.2	-47.5	42.7	51.3	.6	304.0	4700	1	21.7
42	ASCENSION	PANCRAWA	-7.5	14.2	-17.9	-26.1	-27.5	115.7	4902	24	6.0, 9.7, 15.4, 21.7

Table 2. Summary of transmission circuits contained in the field strength data base
(continued).

ID	TRANSMITTER	RECEIVER	TIAF	TION	MIAT	RION	AZIM	RANGE	HOURS	FREQUENCIES (MHz)	
43	SPCKVILLE	BOCKPACKEN	45.5	64.2	54.1	-7.2	81.9	5095	16	15.3,21.7	
44	SPCKVILLE	CHATTOWAYE	45.5	64.2	51.8	-6.6	88.7	5277	3	15.3	
45	NEW YORK	NORDEICH	41.4	70.0	54.1	-7.1	73.8	5632	756	6.4, 8.6,13.0,17.0,22.5	
46	SPCKVILLE	JOKELA	45.5	64.2	61.4	60.3	-25.0	68.0	5671	4	15.3,17.8
47	KIWI	HIRASO	22.0	159.5	32.7	36.2	-140.4	286.6	5906	710	15.0
48	NEW YORK	ILIECHOW	41.4	70.0	54.6	52.6	-11.1	75.2	5910	166	6.4, 8.6,13.0,17.0,22.5
49	DARWIN	BEIJING	-12.2	-130.4	13.8	39.6	-116.3	346.4	6004	1	7.1
50	GREENVILLE	BALDOCK	35.3	77.2	50.5	52.0	.1	69.2	6150	1	9.7
51	GREENVILLE	JURBSE	35.3	77.2	50.5	50.3	-3.6	72.0	6468	3	15.4
52	NAIROBI	ILIECHOW	-1.2	-36.5	26.2	52.6	-11.1	339.9	6497	435	9.0,17.4
53	NORFOLK	ILIECHOW	36.5	76.3	53.5	52.6	-11.1	70.5	6690	655	5.0, 8.1,10.9,16.4,20.0
54	DAVENTRY	DEHLI	52.2	1.1	47.2	28.4	-77.1	117.1	6756	7	17.7,17.8
55	LIMASSOL	PANORAMA	34.4	-33.2	4.2	-26.1	-27.5	184.8	6787	8	17.9,21.7
56	GREENVILLE	CHATTOWAYE	35.3	77.2	49.2	46.5	-6.6	77.3	6825	2	9.7
57	ANTIGUA	BOCKPACKEN	17.1	61.5	39.0	51.1	-7.2	53.6	7082	23	6.2
58	CARAVRON	DEHLI	-24.5	-113.4	2.0	28.4	-77.1	328.0	7126	18	9.8,21.6,21.7
59	CARAVRON	BELMING	-24.5	-113.4	7.5	39.6	-116.3	2.2	7217	14	11.8
60	GREENVILLE	JOKELA	35.3	77.2	59.3	60.3	-25.0	58.2	7238	2	9.7
61	WERTACHIAL	BEIJING	48.0	-10.4	57.7	39.6	-116.3	100.0	7807	14	11.8,15.3,17.8,21.6
62	ASCENSION	JOKELA	-7.5	14.2	27.6	60.3	-25.0	21.3	8355	3	9.7,11.8
63	SHEPPARTON	TRIVANDRUM	-36.2	-145.3	-16.7	8.3	-76.6	307.5	8689	13	9.8
64	MELVERTON	BOCKPACKEN	-26.4	-28.1	12.6	51.1	-7.2	347.9	8879	14	21.5,25.8
65	SHEPPARTON	BEIJING	-36.2	-145.3	1.7	39.6	-116.3	342.2	8985	8	15.1
66	TOKIO	NRUEICH	35.5	-139.4	66.4	53.3	-7.1	295.0	9083	945	7.3,10.0,13.6,18.2,22.8
67	FORT COLLINS	HIRASO	40.4	105.0	55.6	36.2	-140.4	265.6	9144	307	15.0
68	DAVENTRY	PANORAMA	52.2	1.1	13.4	-26.1	-27.5	164.1	9159	3	21.7
69	MEYERTON	BALDOCK	-26.4	-28.1	13.2	52.0	.1	344.3	9163	1	25.8
70	MARUTTUS	ILIECHOW	-20.2	-57.3	17.5	52.6	-11.1	334.3	9287	717	8.6,13.0,17.0,22.6
71	SKELTON	PANORAMA	54.4	2.5	14.6	-26.1	-27.5	164.2	9459	4	21.7
72	QUITO	JURBSE	-.1	78.2	31.3	50.3	-3.6	47.9	9483	4	11.8
73	QUITO	BOCKPACKEN	-.1	78.2	32.4	51.1	-7.2	47.9	9721	15	9.7
74	DEIANO	BEIJING	35.5	119.2	58.8	39.6	-116.3	274.5	9849	17	21.5
75	SHEPPARTON	DEHLI	-36.2	-145.3	-4.7	28.4	-77.1	318.6	10151	15	21.7
76	QUITO	JOKELA	-.1	78.2	40.6	60.3	-25.0	39.7	10754	2	11.8
77	WASHINGTON	HIRASO	39.0	76.5	67.7	36.2	-140.4	266.1	10798	48	15.0
78	DARWIN	JOKELA	-12.2	-130.4	34.1	60.3	-25.0	323.7	12059	6	15.4,17.7
79	CARAVRON	ILIECHOW	-24.5	-113.4	23.4	60.3	-25.0	328.5	12332	6	5.1,11.0,13.9,19.7
80	CANEERRA	NORDEICH	-35.2	-149.1	21.7	52.6	-11.1	320.5	16206	822	5.1,11.0,13.9,19.7
81	CANEERRA	NORDEICH	-35.2	-149.1	24.1	53.3	-7.1	321.8	16448	169	5.1,11.0,13.9,19.7

The data base used to assess these models, Data Base C from the CCIR, has no frequencies below 4.8 MHz. There is currently a new data base available from the CCIR, called Data Base D, which has frequencies down to about 2 Hz. We recommend that this data base be obtained for further efforts.

The procedure followed was to generate separate predicted data bases using each of the models described in this report. These were then compared, using DASCR3, to the measured data in blocks corresponding to specified screening conditions as described earlier.

RESULTS OF COMPARISON TO DATA

We present here the results of the comparison of the PROPHET and HFBC84 field strength prediction programs to measured data. Throughout this section, table 2 should be consulted as the relative lack of data in some cases makes the validity of statistical analysis questionable. A limited analysis of the results and recommendations for further investigations will be presented in the next section.

The following quantities are referred to in the accompanying figures (Sailors et al., 1981):

- residual = observed datum - predicted value
- relative residual = residual/observed datum
- absolute relative residual = absolute residual/observed datum.

Here the observed datum and predicted value correspond to a complete set of identical conditions, i.e., time, month, year, sunspot number, path, etc. From these parameters, the following six statistical quantities derived from the residual distributions are plotted:

- average residual (bias)
- root mean square residual (rms res)
- average relative residual (av rel res)
- root mean square relative residual (rms rel res)
- average absolute relative residual (av abs rel res)
- correlation coefficient between observed and predicted values.

Each of these statistical quantities is calculated by the DASCR3 program. Examples are shown in figures 1 to 6 where each of these quantities is plotted as a function of the operating frequency to MUF ratio.

OVERALL RESULTS AS A FUNCTION OF F/MUF RATIO

As we pointed out earlier, there is some question as to the adequacy of current models for field strength prediction when the frequency exceeds the MUF for the mode. The series of plots in figures 1 to 6 show clearly that for f/MUF ratios of ~1.5 or larger neither model provides satisfactory predictions.

The average residual, figure 1, and the average relative residual, figure 2, locate the center of the distributions for these quantities and are

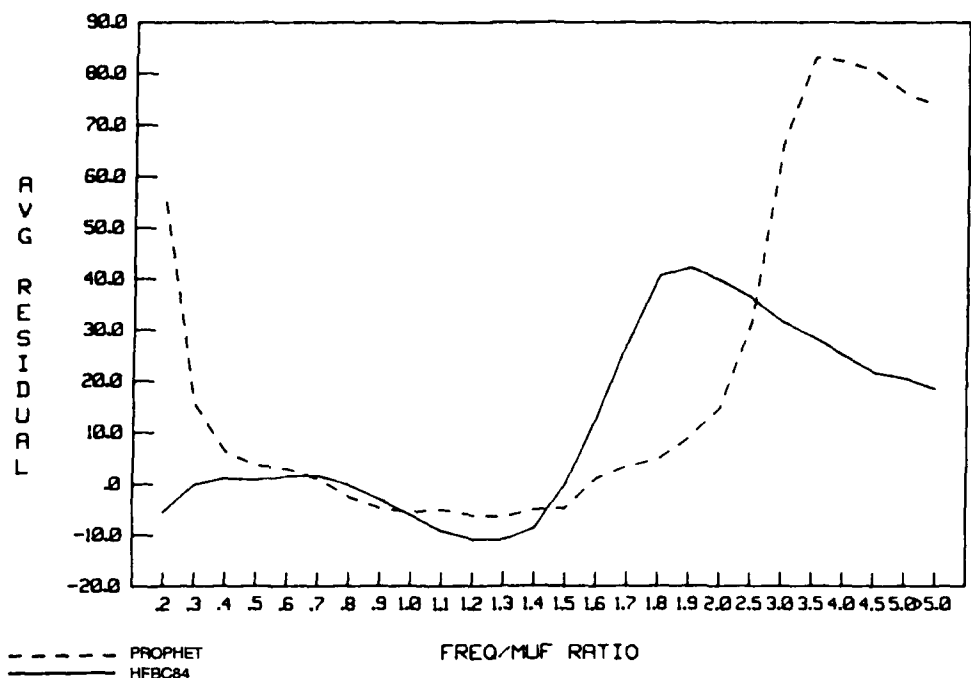


Figure 1. Average relative residual as a function of frequency-to-MUF ratio.

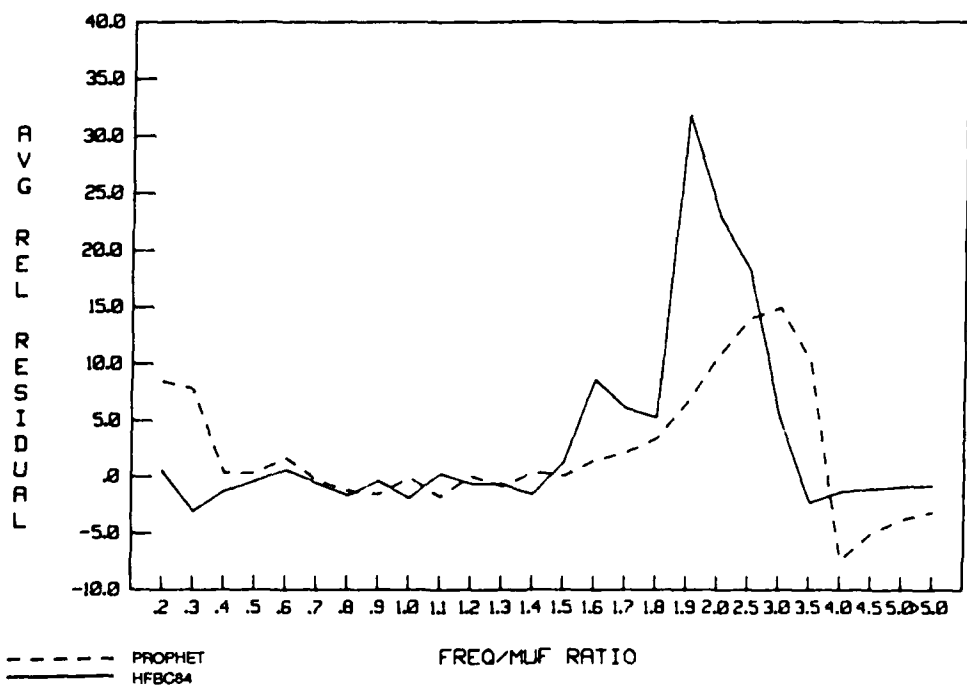


Figure 2. Average relative residual as a function of frequency-to-MUF ratio.

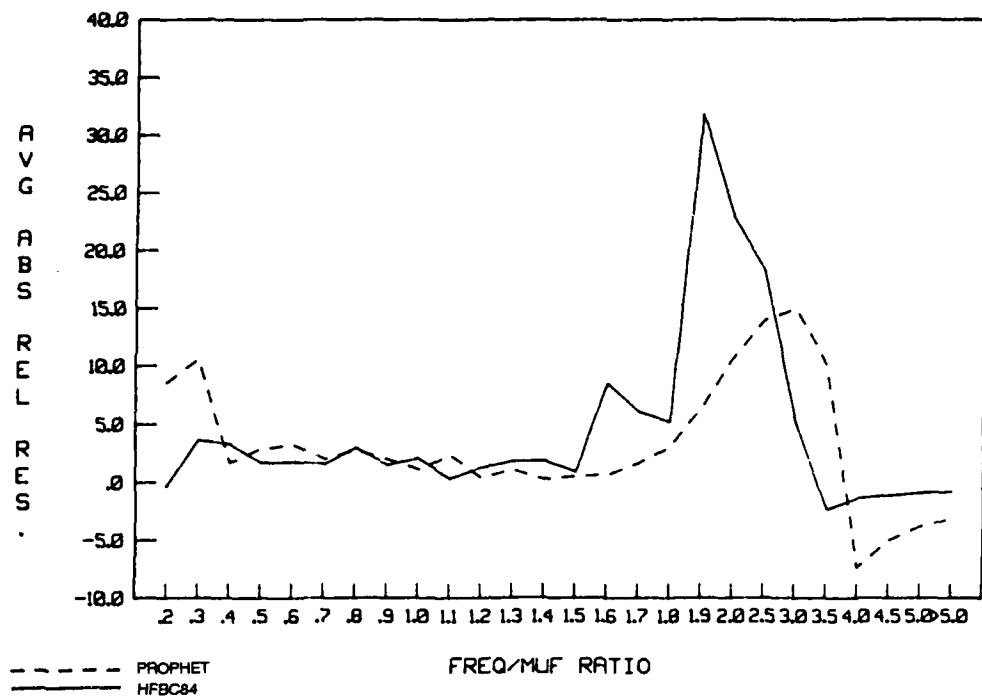


Figure 3. Average absolute relative residual as a function of frequency-to-MUF ratio.

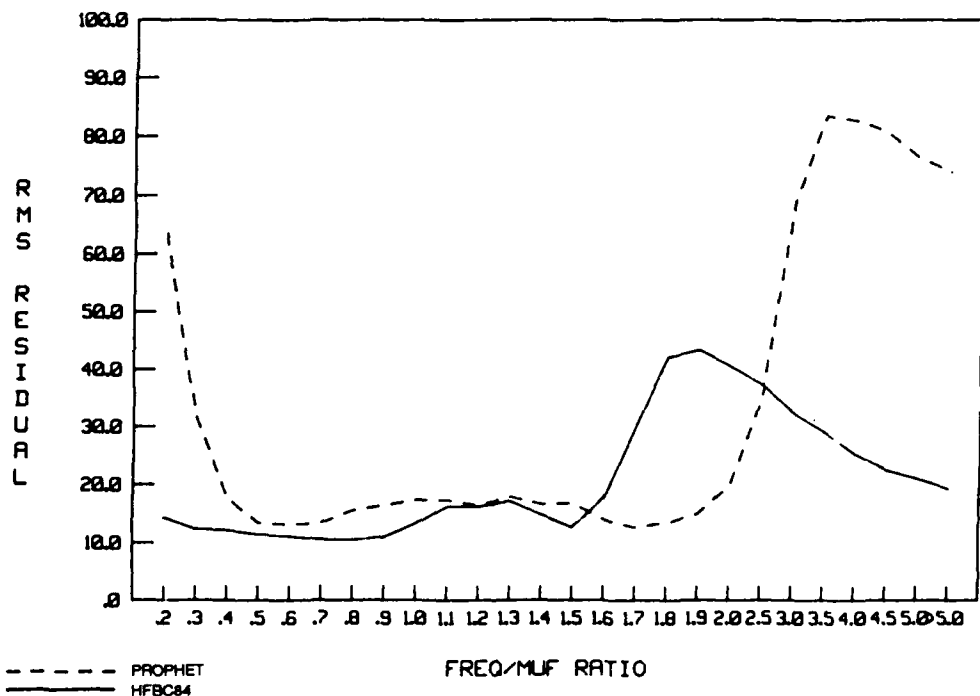


Figure 4. Root mean square residual as a function of frequency-to-MUF ratio.

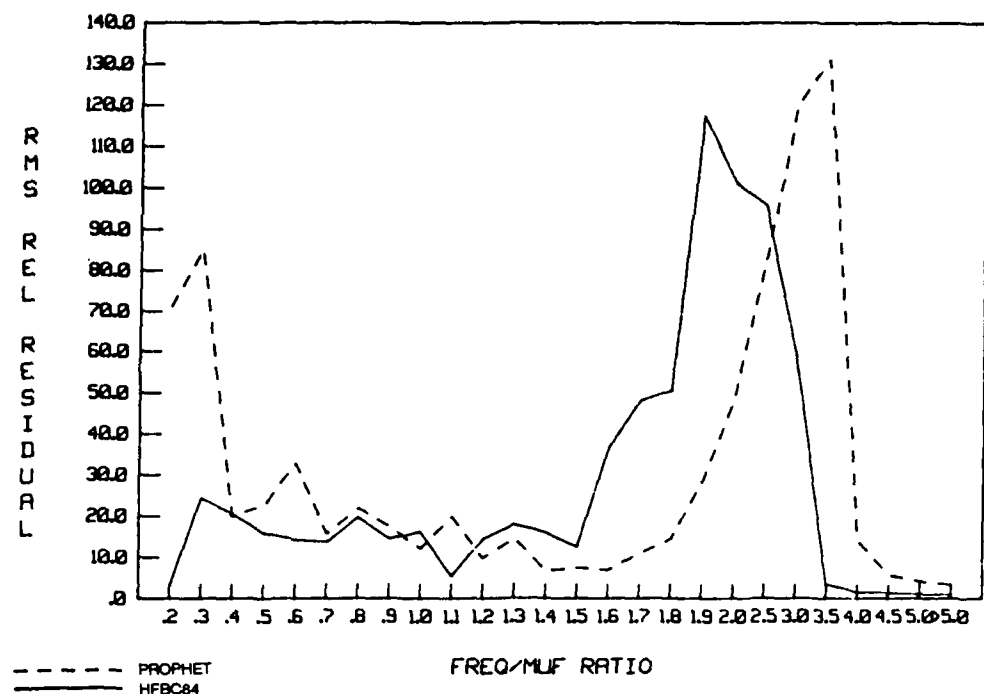


Figure 5. Root mean square relative residual as a function of frequency-to-MUF ratio.

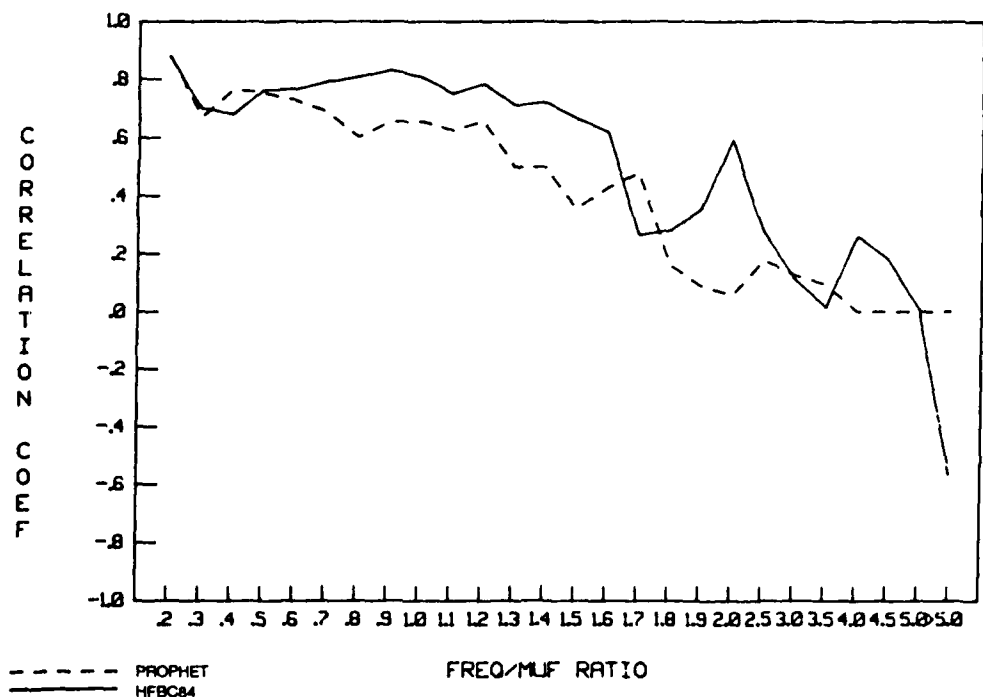


Figure 6. Correlation coefficient as a function of frequency-to-MUF ratio.

referred to as the bias in the estimate (Sailors et al., 1981). Both of these figures show large errors at ratios greater than approximately 1.5. Also, the PROPHET model shows a relative peak in the error at low frequencies.

The average absolute relative residual is a measure of the average magnitude of the error (bias). Figure 3 shows the same characteristic behavior as the earlier figures. Both models show quite good results for frequencies of approximately 0.5 to 1.5 of the MUF. However, both models show poor performance at higher frequencies. Again, the PROPHET model shows some problems at low frequencies.

The root mean square residual and root mean square relative residual are measures of the dispersion in the error (Sailors et al., 1981). They represent the standard deviation of the error about the origin. So for a model with zero bias in the error, the standard deviation and rms values are identical. Figures 4 and 5 show these quantities as a function of f/MUF ratio. They both display large dispersion in the predictions.

The correlation coefficient is a measure of the degree of association of the closeness of fit between the observed and predicted values. It indicates the strength of the tendency for high (low) values of one variable to be associated with high (low) values of the other (Sailors et al., 1981). Figure 6 shows the correlation coefficient in the current case. Both models show similar behavior in that they tend to decrease almost uniformly as the frequency to MUF ratio increases. HFBC84 shows an offset that increases its correlation over most of the frequency range, but it shows the same overall tendency as PROPHET.

These results show that, in general, neither method of predicting over-the-MUF field strength is adequate. For this reason the following plots and tables have been screened according to whether the operating frequency is greater or less than the MUF. Results are presented for each case. In this way other aspects of the models' performance can be investigated, independent of the effects of the poor over-the-MUF models. In the appendix we give the overall results in tabular form.

INDIVIDUAL CIRCUIT RESULTS

In figures 7 to 18 we show the performance of the models for the individual circuits listed in table 2. In figures 7 to 12 the operating frequencies are less than (or equal to) the MUF for the path, and in figures 13 to 18 the frequencies are greater than the MUF.

Figure 7 shows considerable variation (± 20 dB) in the average residual (bias) around a value near zero for most circuits. However, for circuit identification numbers less than about 18, PROPHET tends to underpredict the field strength relative to HFBC84 predictions. For circuit numbers 55 and greater, HFBC84 tends to underpredict relative to PROPHET. Referring to table 2, circuit numbers less than 18 refer to paths less than 1200 km, while those greater than 55 refer to paths approximately 7000 km and longer. Since PROPHET uses a variation of the FTZ method at all path lengths, both of these path length regions point to a problem with that model.

The average residual for frequencies greater than the MUF is shown in figure 13. The tendency here is for both models to underpredict at short (≤ 2000 km) path lengths. Both models overpredict for longer (≥ 4000 km) paths with PROPHET showing a decreasing linear trend with path length.

In figures 8 to 12, the plots for the remaining statistical parameters are presented for frequencies less than the MUF. Figure 8 shows that the rms residual averages approximately 10 dB for short to midlength paths for both models. Again we see a small long path deviation in HFBC84.

Figures 9 to 11 all show similar behavior. The dominant feature is the erratic performance for circuit 22. Although the data sample is extremely small for this circuit, the failure of both models tends to make the quality of the data suspect.

Figure 12 shows the correlation coefficient for each model. Both models show variation over the entire range from 1.0 to -1.0. No clear trend is discernible from this plot.

For completeness, figures 13 to 18 show the results for frequencies greater than the MUF. As we have indicated, the poor performance of the over-the-MUF models in general make isolating other effects difficult.

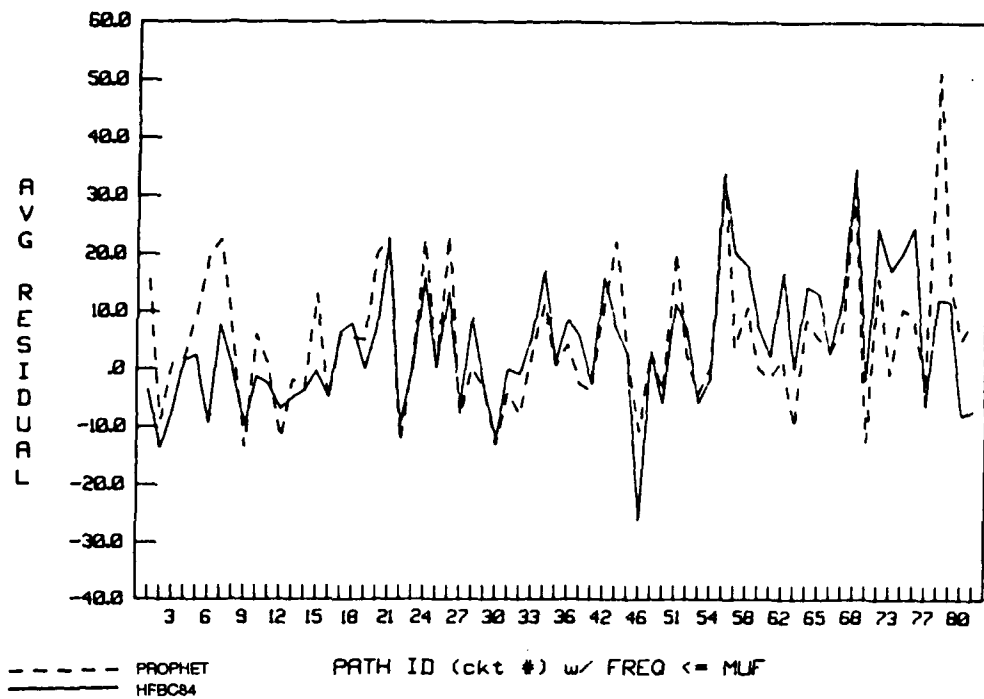


Figure 7. Average residual for each circuit with frequency less than or equal to the MUF.

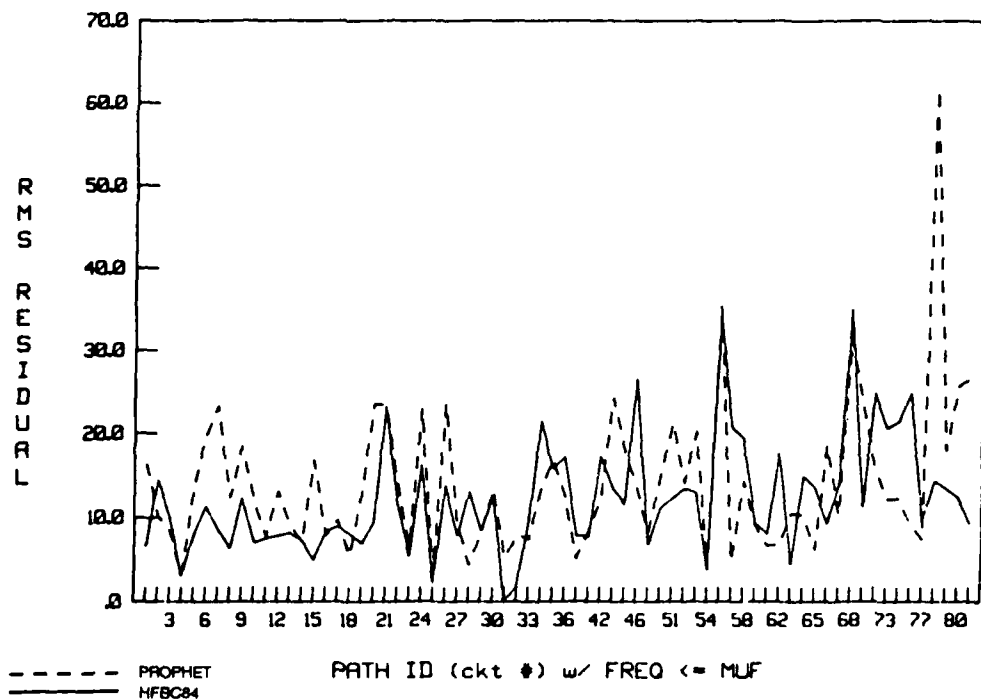


Figure 8. Root mean square residual for each circuit with frequency less than or equal to the MUF.

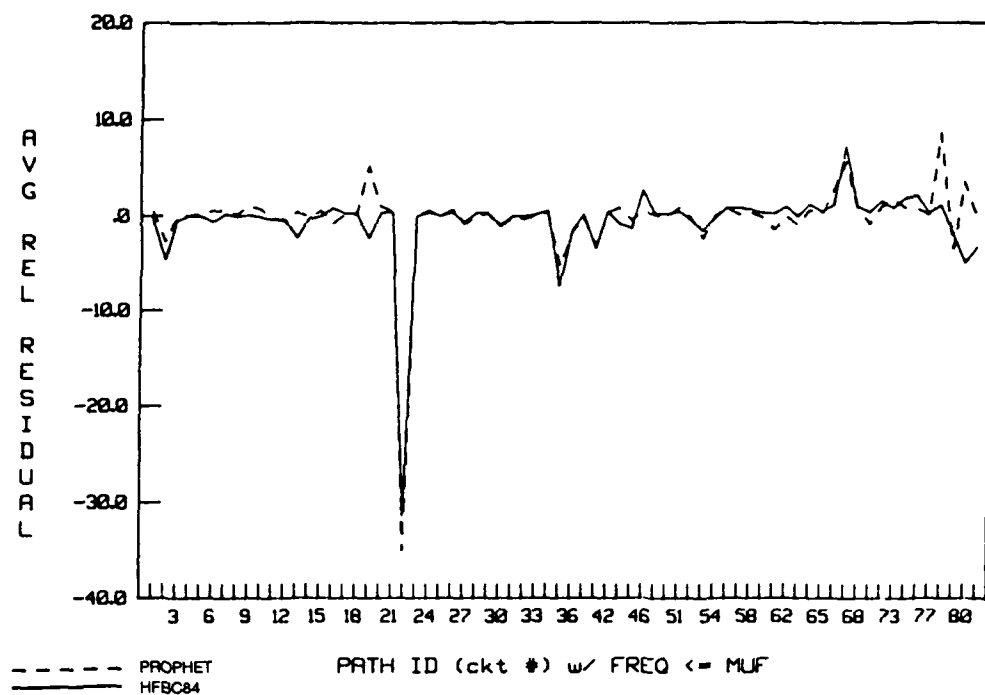


Figure 9. Average relative residual for each circuit with frequency less than or equal to the MUF.

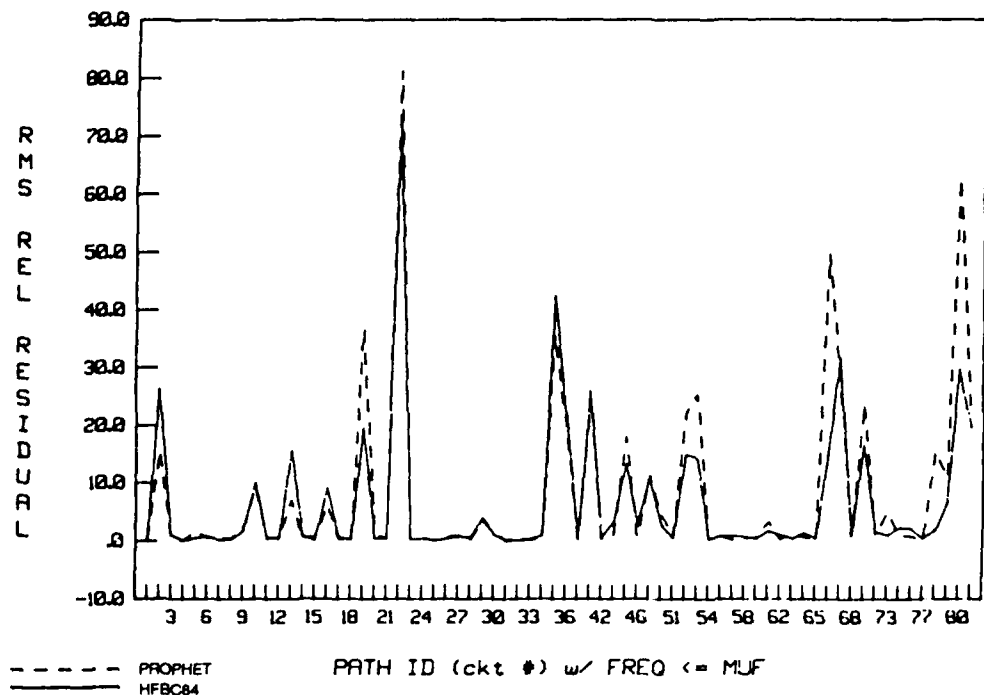


Figure 10. Root mean square relative residual for each circuit with frequency less than or equal to the MUF.

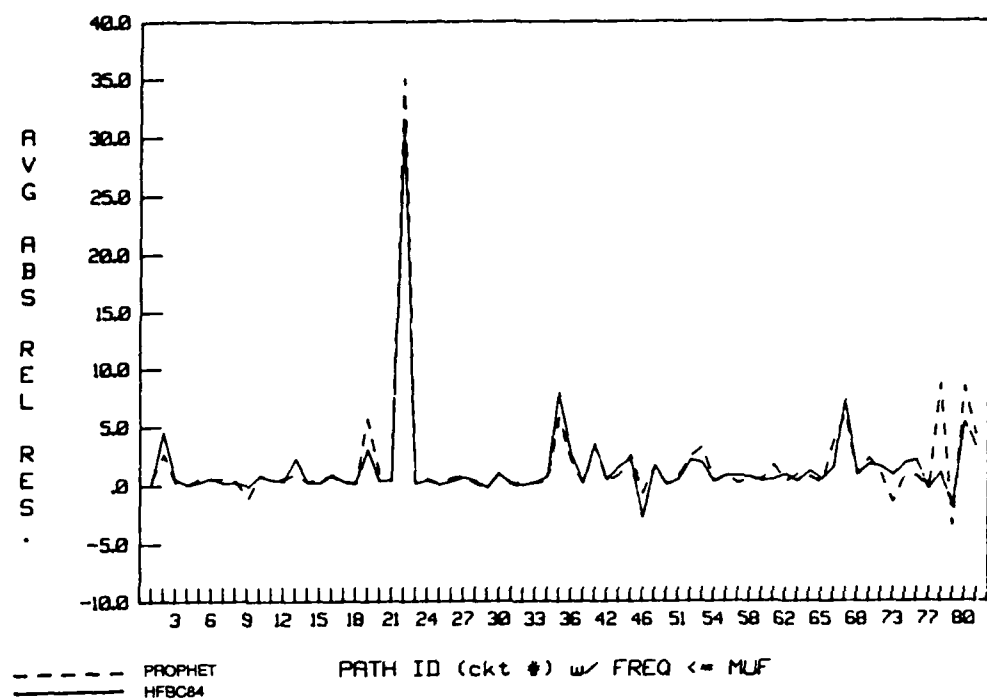


Figure 11. Average absolute relative residual for each circuit with frequency less than or equal to the MUF.

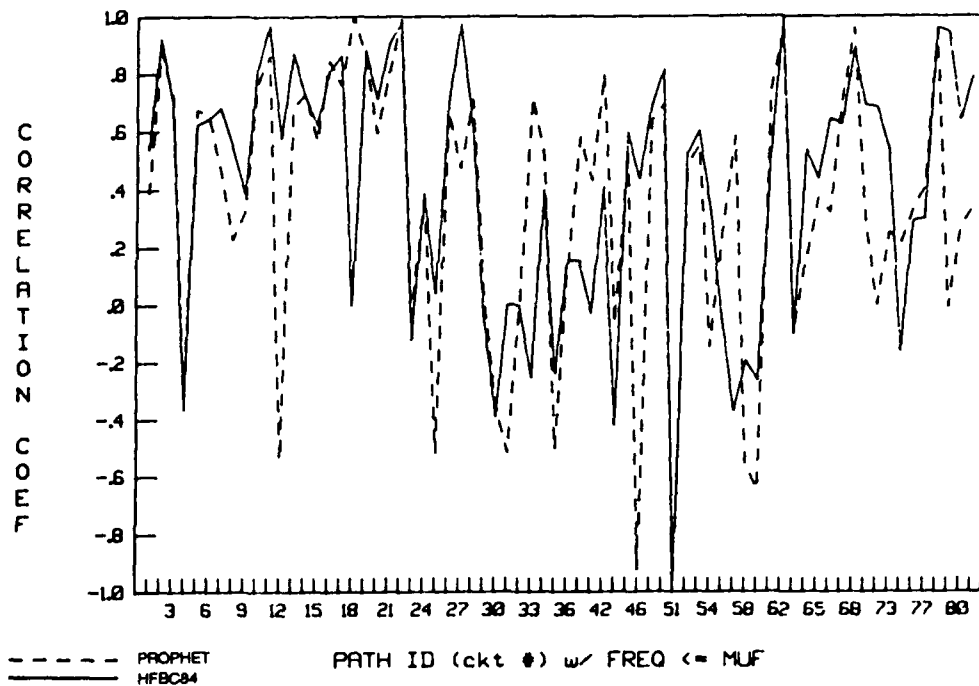


Figure 12. Correlation coefficient for each circuit with frequency less than or equal to the MUF.

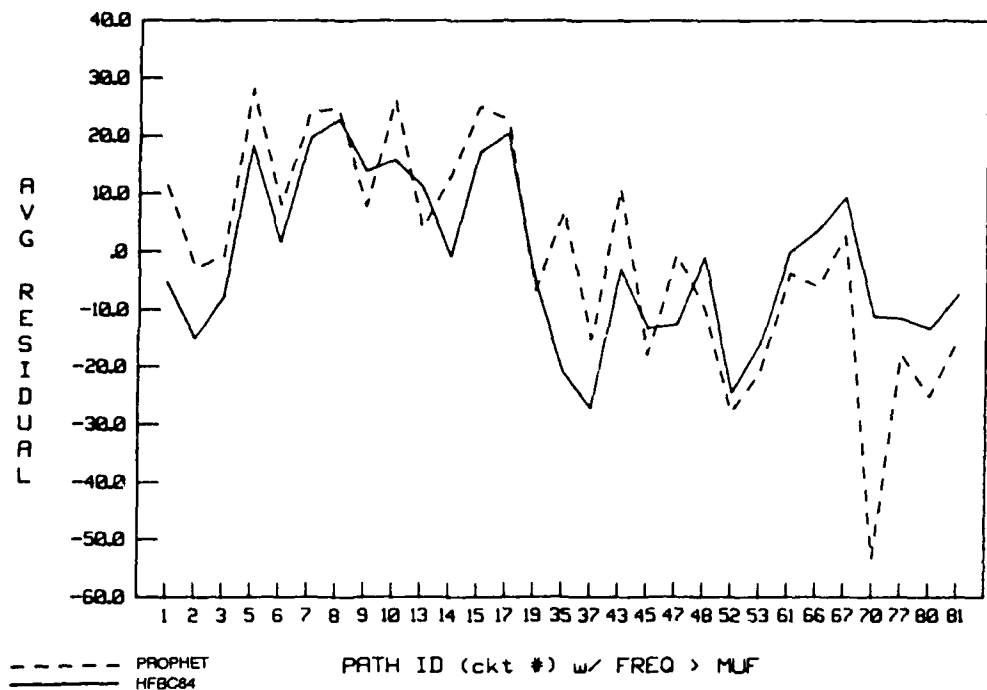


Figure 13. Average residual for each circuit with frequency greater than the MUF.

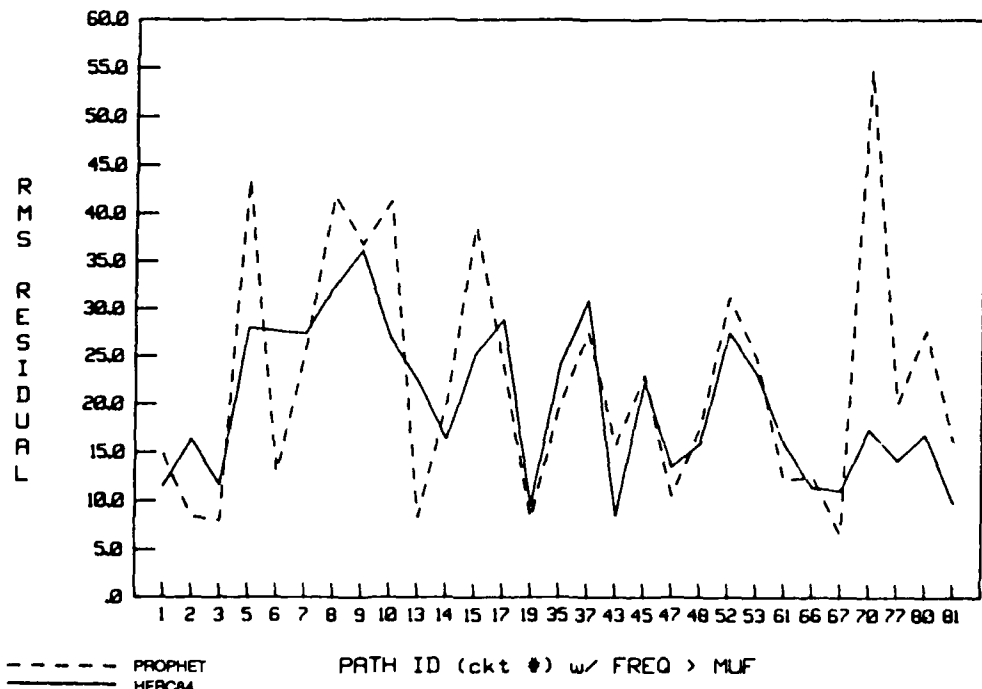


Figure 14. Root mean square residual for each circuit with frequency greater than the MUF.

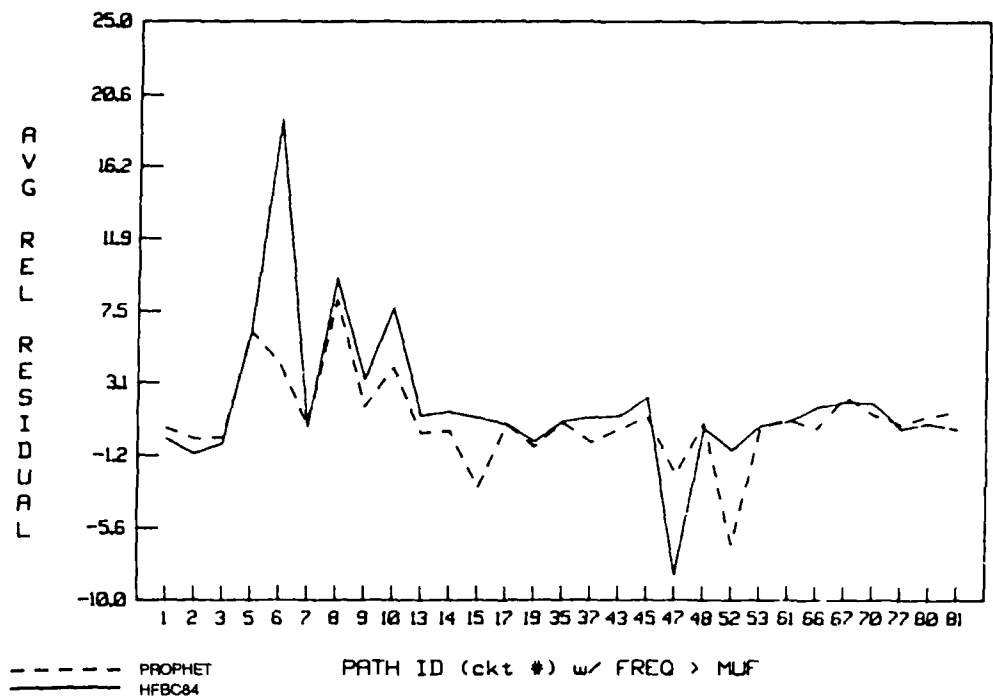


Figure 15. Average relative residual for each circuit with frequency greater than the MUF.

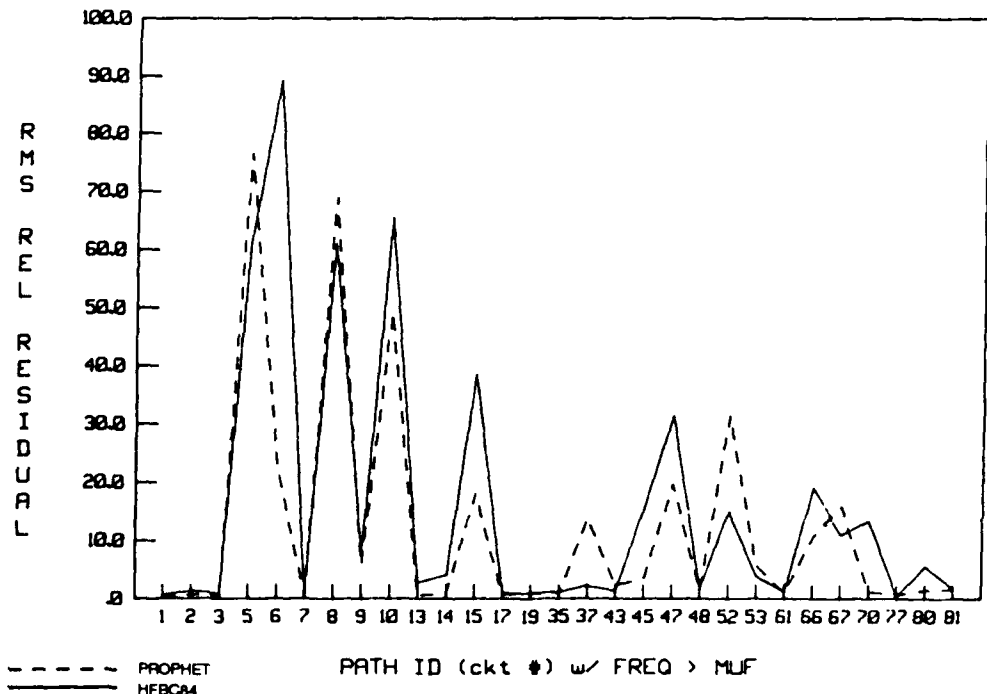


Figure 16. Root mean square relative residual for each circuit with frequency greater than the MUF.

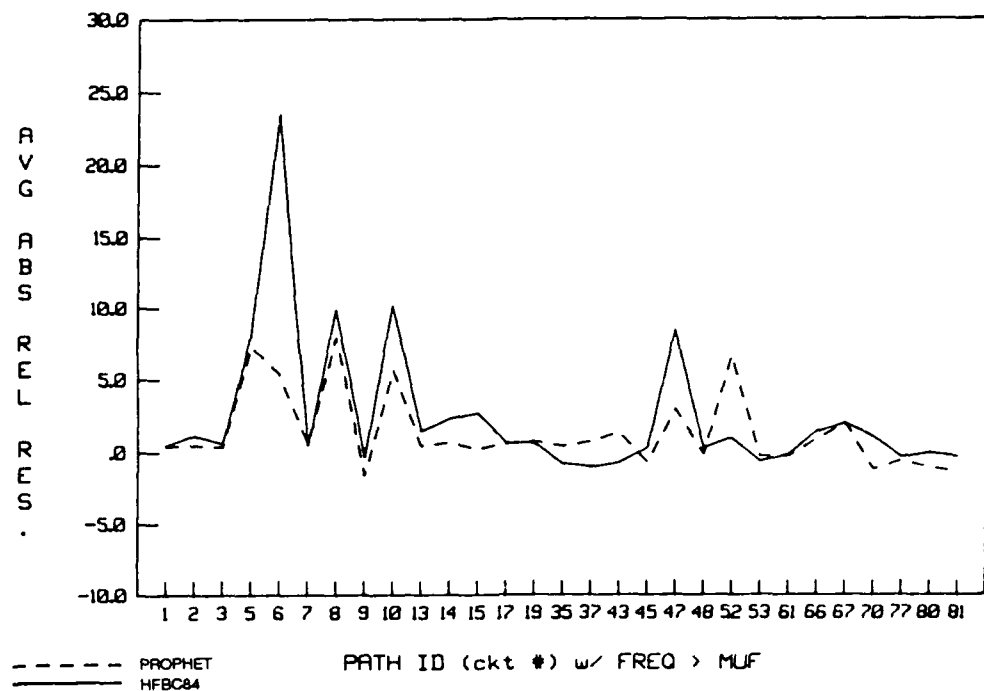


Figure 17. Average absolute relative residual for each circuit with frequency greater than the MUF.

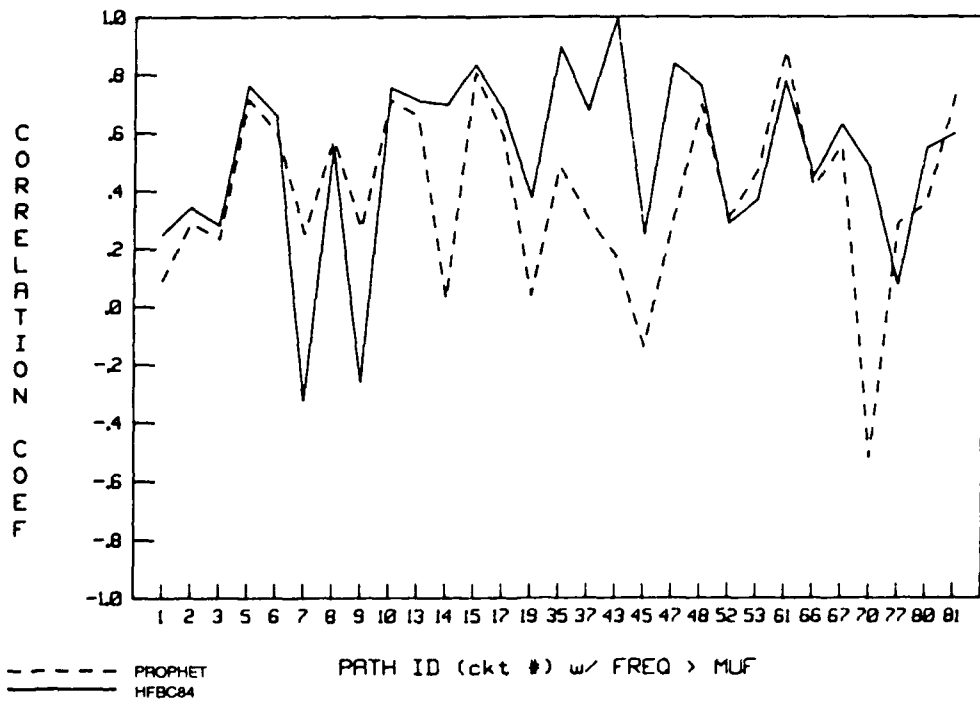


Figure 18. Correlation coefficient for each circuit with frequency greater than the MUF.

CIRCUIT LENGTH RESULTS

The results presented in the previous section indicate the relatively poor performance of the HFBC84 model for paths longer than ~7000 km. The results presented here are consistent in that HFBC84 again shows, in figure 19, an increased bias for these path lengths at frequencies below the MUF. Except for the very longest paths (>11,000 km), PROPHET is relatively consistent with an average bias of ± 5 dB across all range.

Results for the rms residual are shown in figure 20. Both models vary between approximately 10 to 20 dB over most of the ranges. PROPHET shows even larger variation at the extreme path lengths.

Figure 21 shows the average relative residual for frequencies less than the MUF. Again we see HFBC84 performs relatively poorly at longer path ranges. In this case, PROPHET also shows large variation at longer path lengths.

Results for the other statistical parameters for frequencies less than the MUF are shown in figures 22 to 24. In particular, the correlation coefficient, figure 24, shows a large amount of variation for both models. No clear systematic trends are discernible from these results.

Figures 25 to 30 show plots of the statistical parameters for frequencies greater than the MUF. The broken lines in these figures indicate a lack of data for that particular model. Neither model performs well in this series of plots. One feature that does stand out is the similarity in the results in each case, which makes specifying the "better" model for these conditions difficult.

SEASONAL RESULTS

Both models described in this report are functions of season. In PROPHET, the seasonal dependence is contained in the LUF and MUF predictions. For HFBC84, seasonal dependence is found in the MUF and in the ionospheric absorption loss term. There is also seasonal dependence in the auroral absorption table, as discussed above.

To investigate the accuracy of the modeled dependency on season in both models, we partitioned the data bases with respect to the four seasons and compared predictions with data for each case. The results for frequencies less than the MUF are shown in figures 31 to 36.

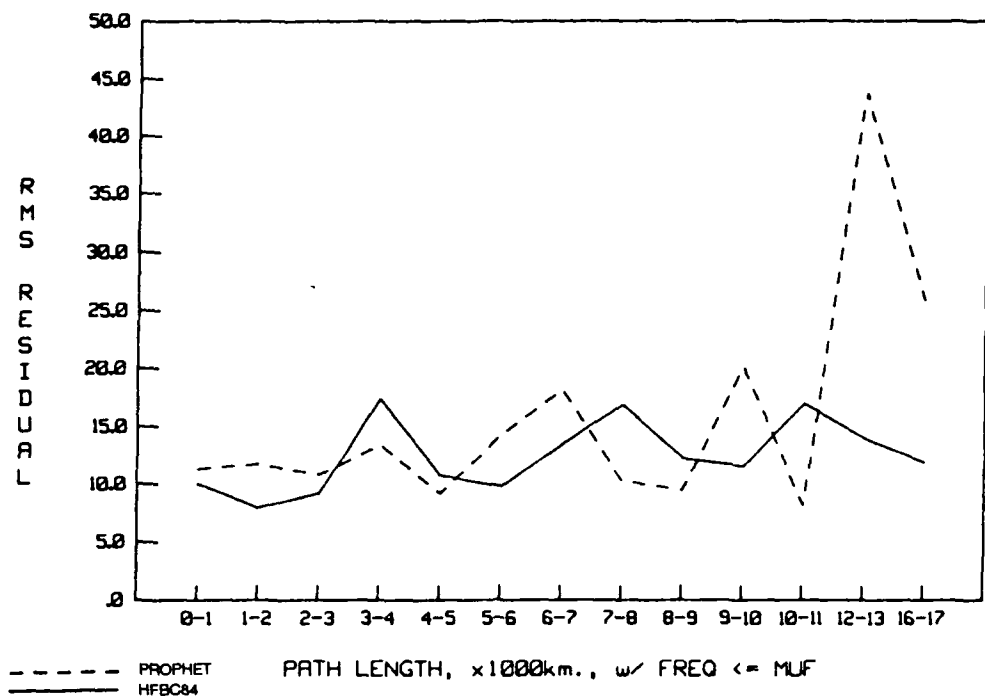


Figure 19. Average residual as a function of circuit length for frequencies less than or equal to the MUF.

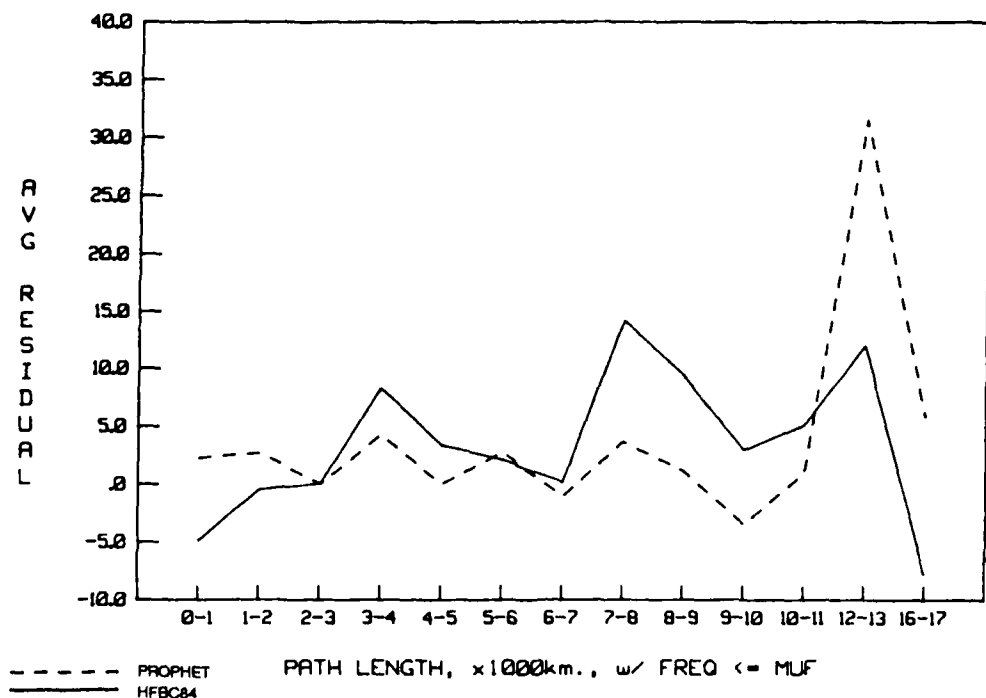


Figure 20. Root mean square residual as a function of circuit length for frequencies less than or equal to the MUF.

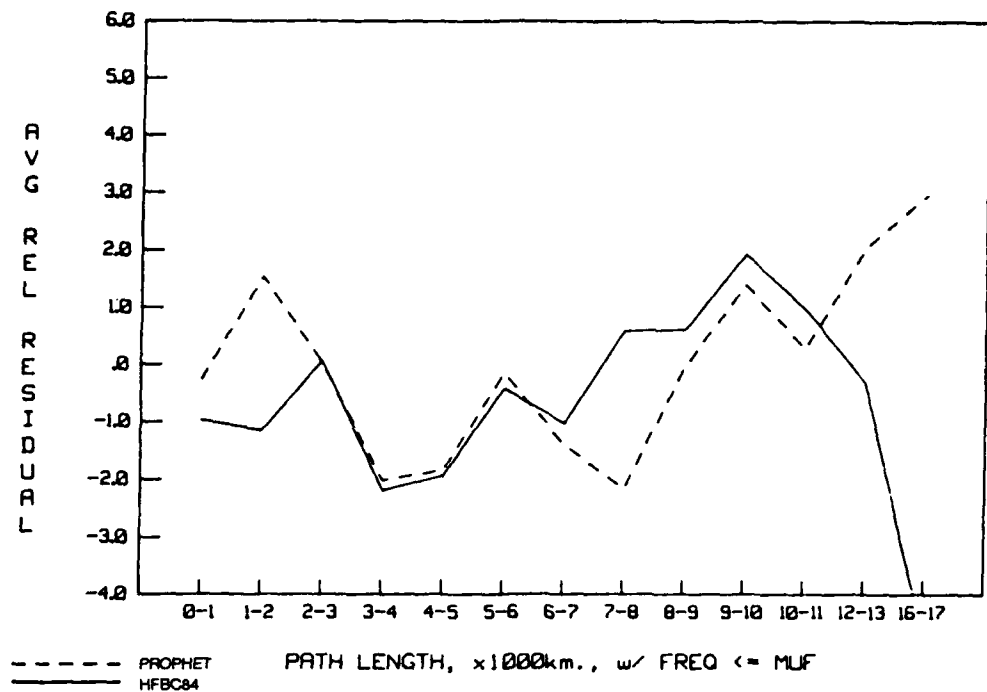


Figure 21. Average relative residual as a function of circuit length for frequencies less than or equal to the MUF.

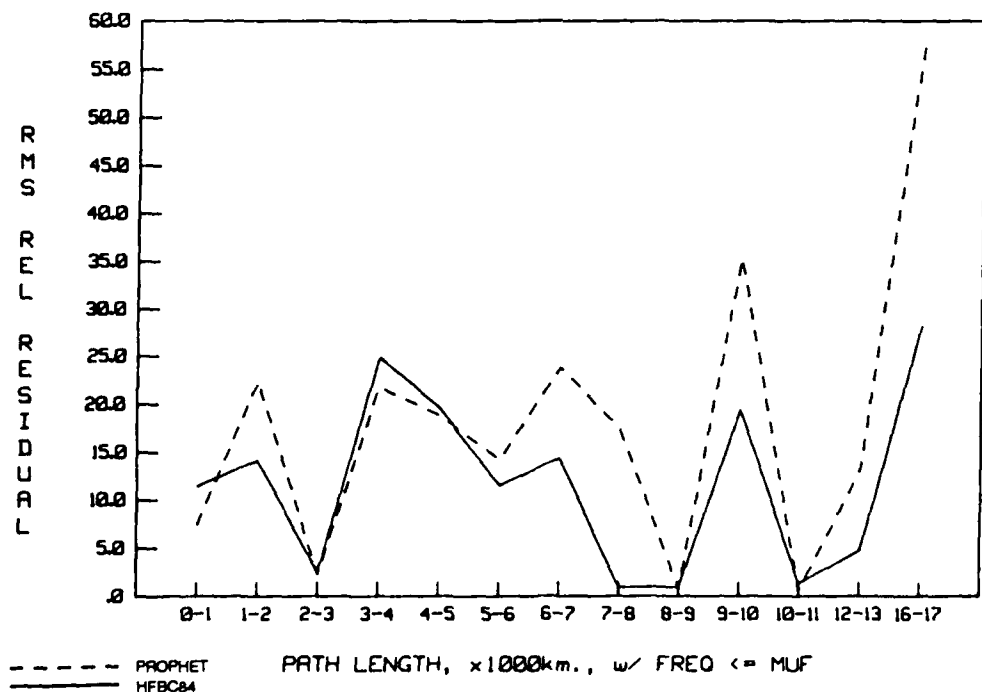


Figure 22. Root mean square relative residual as a function of circuit length for frequencies less than or equal to the MUF.

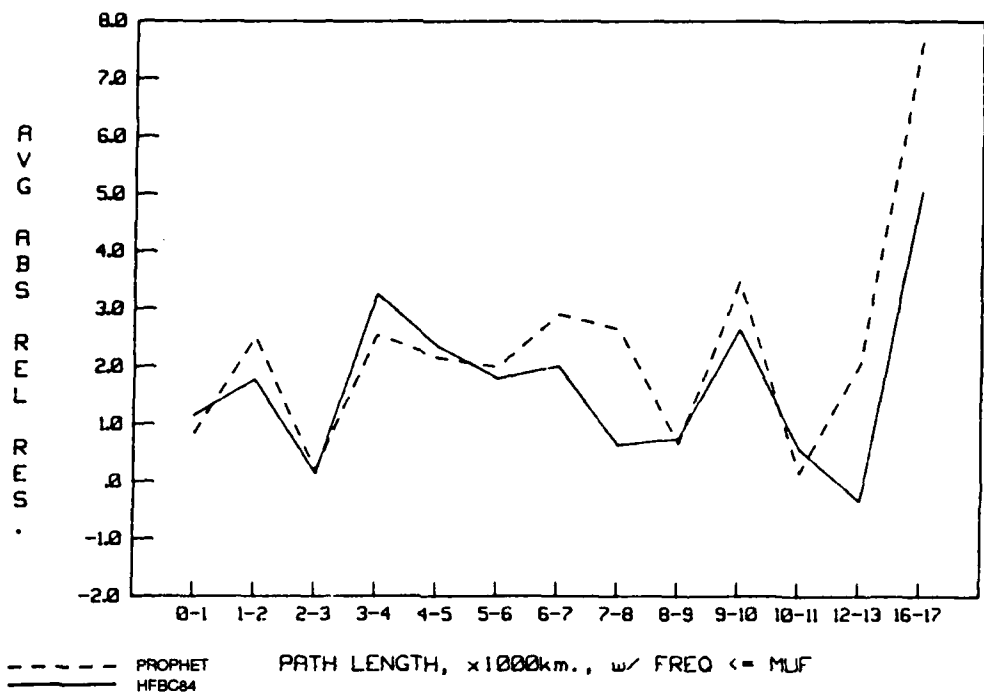


Figure 23. Average absolute relative residual as a function of circuit length for frequencies less than or equal to the MUF.

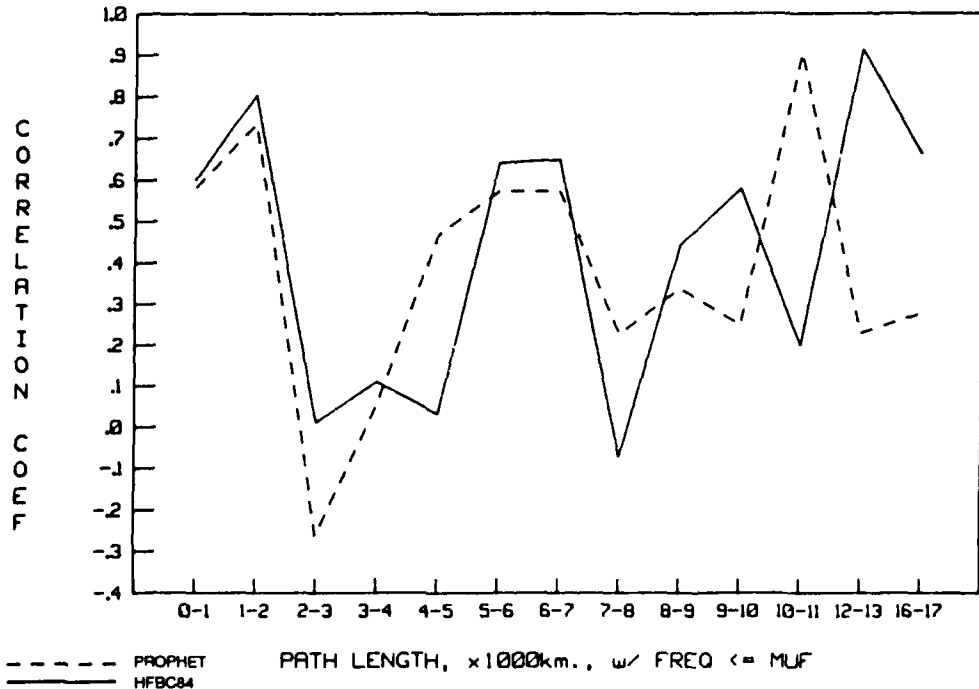


Figure 24. Correlation coefficient as a function of circuit length for frequencies less than or equal to the MUF.

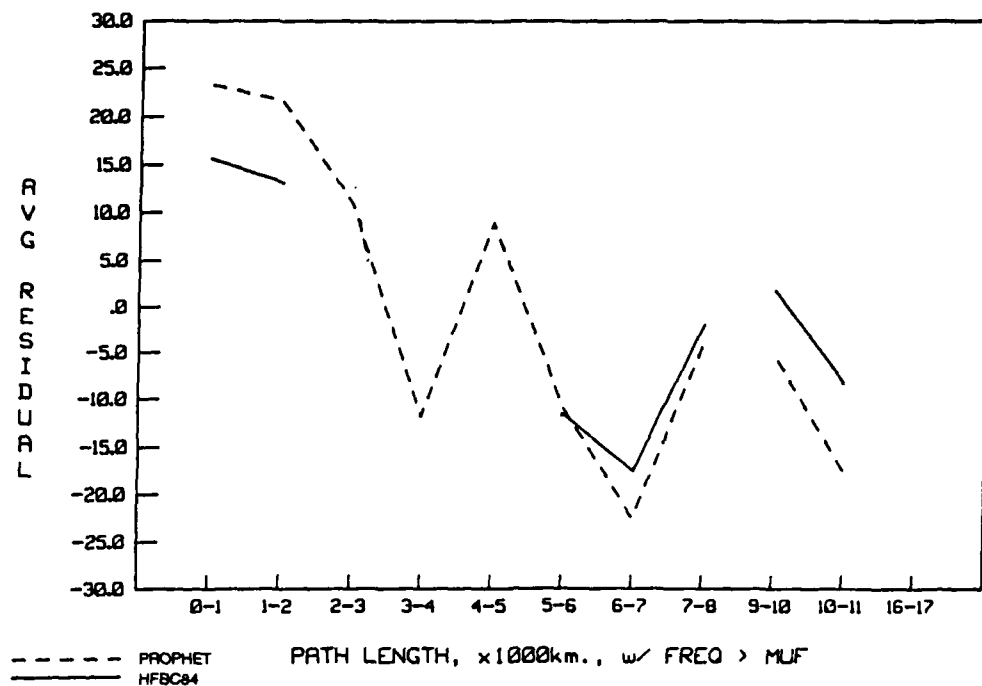


Figure 25. Average residual as a function of circuit length for frequencies greater than the MUF.

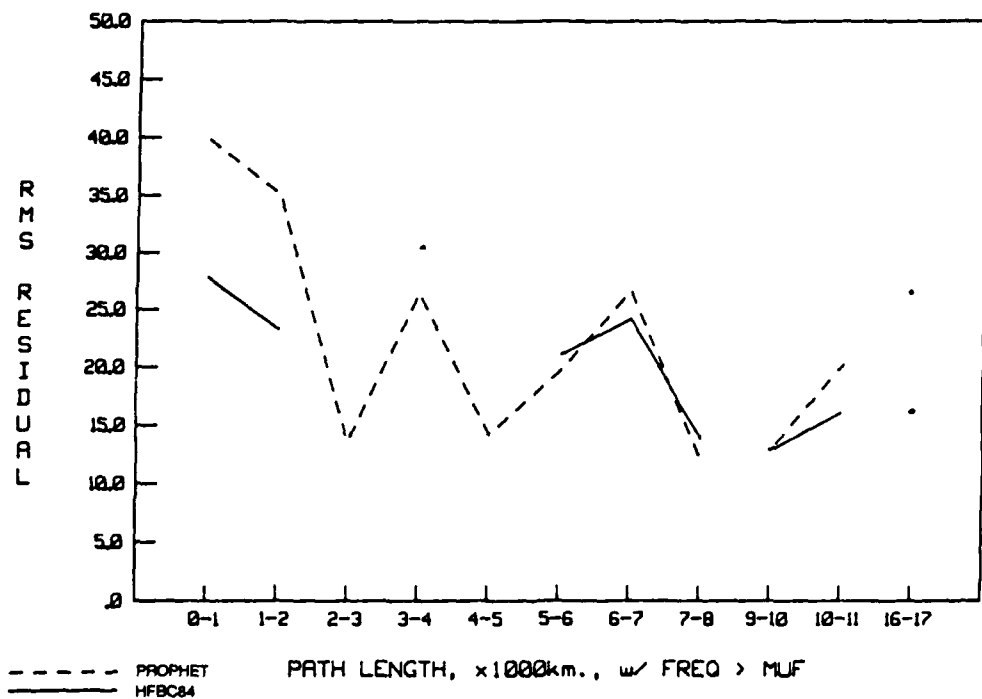


Figure 26. Root mean square residual as a function of circuit length for frequencies greater than the MUF.

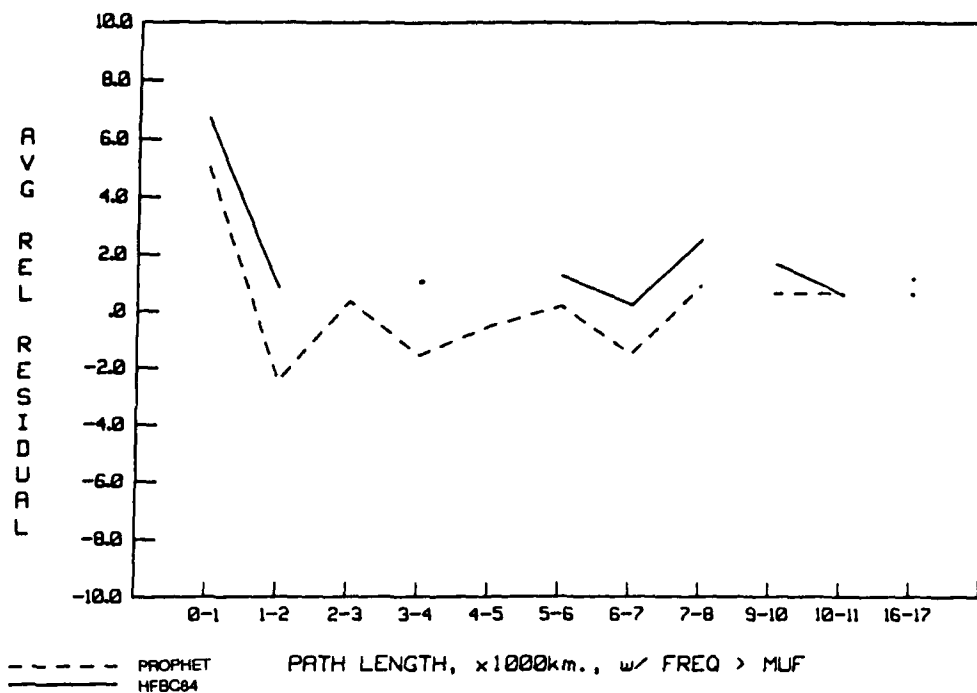


Figure 27. Average relative residual as a function of circuit length for frequencies greater than the MUF.

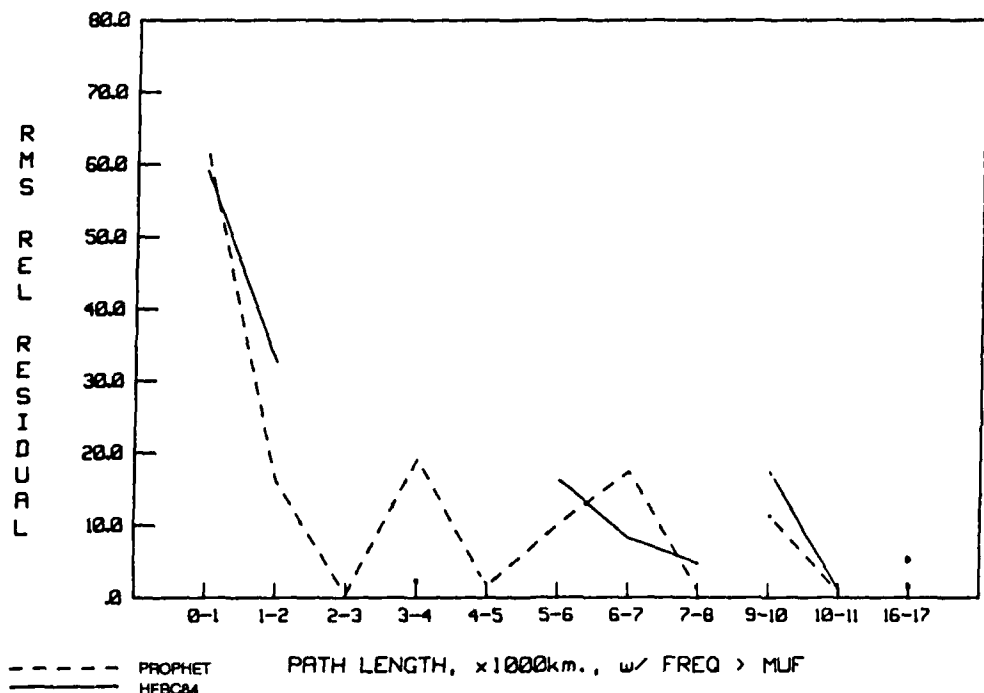


Figure 28. Root mean square relative residual as a function of circuit length for frequencies greater than the MUF.

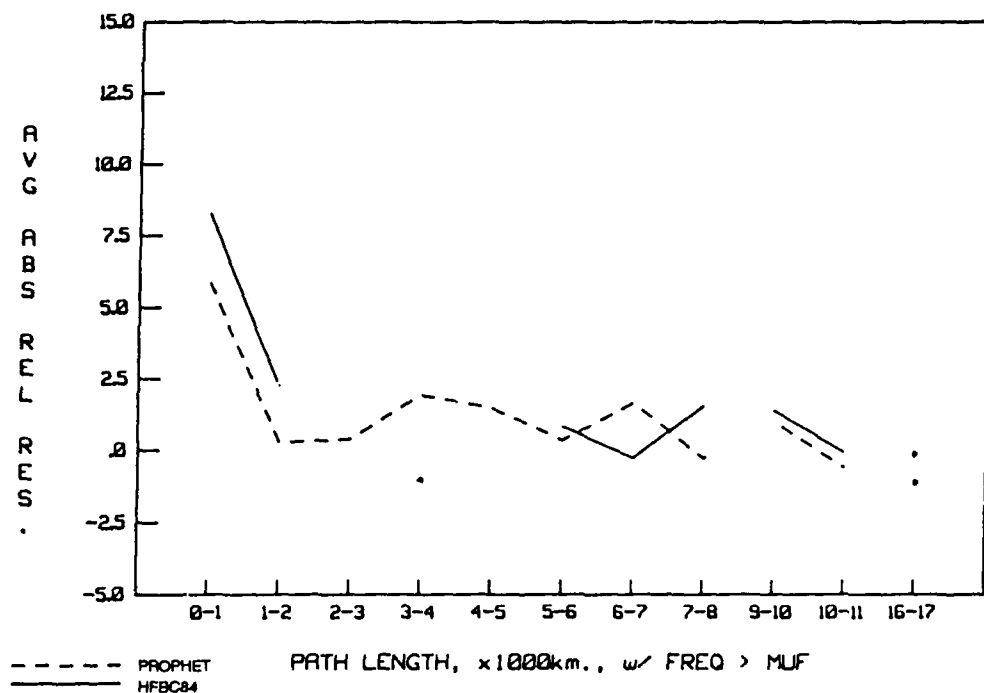


Figure 29. Average absolute relative residual as a function of circuit length for frequencies greater than the MUF.

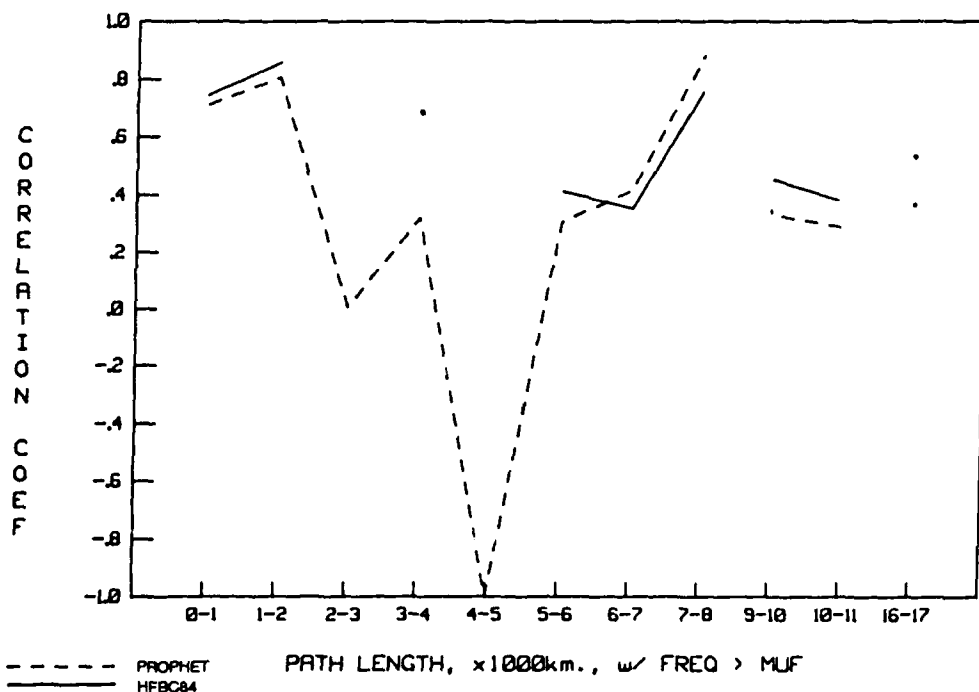


Figure 30. Correlation coefficient as a function of circuit length for frequencies greater than the MUF.

In figure 31 we show the average residual for both models. Each model shows a peak in the winter, although of differing sign. Smaller peaks also occur in summer.

On the other hand, figure 32 shows that the dispersion of the error, rms residual, is much larger in PROPHET than in HFBC84, with a peak in the winter of 21 dB. The HFBC84 model remains approximately constant around 12 dB throughout the year.

Similar results are shown in figures 33 to 36 for the remaining statistical parameters. In all cases, we see that PROPHET shows large deviations in the winter. For each of these parameters, HFBC84 performs quite well throughout the four seasons, with relatively high correlation as shown in figure 36.

In figures 37 to 42 we show a companion set of plots for frequencies exceeding the MUF. Inspection of these figures shows, in each case, behavior similar to that described above. The PROPHET model shows large error and variation in the winter, while HFBC84 is approximately uniform over all seasons in most cases.

SUNSPOT NUMBER RESULTS

In HFBC84 the ionospheric absorption loss term, equation 12, shows dependence on 12-month running mean sunspot number, R_{12} . Dependence on R_{12} is also contained in the long-path model through the absorption equation used to determine f_L .

Conversely, the PROPHET model contains no dependence on R_{12} . Inspection of equation 29 shows the QLOF absorption index contains no sunspot-dependent component.

To determine the necessity of such dependence in the models, we performed data comparison based on the R_{12} parameter. The results for frequencies less than the MUF are contained in figures 43 to 48.

The average residual shown in figure 43 indicates there is no strong dependence on R_{12} in the bias for field strength predictions. We might expect such a dependence to be most notable for large values of R_{12} , however, such behavior is not indicated in this figure.

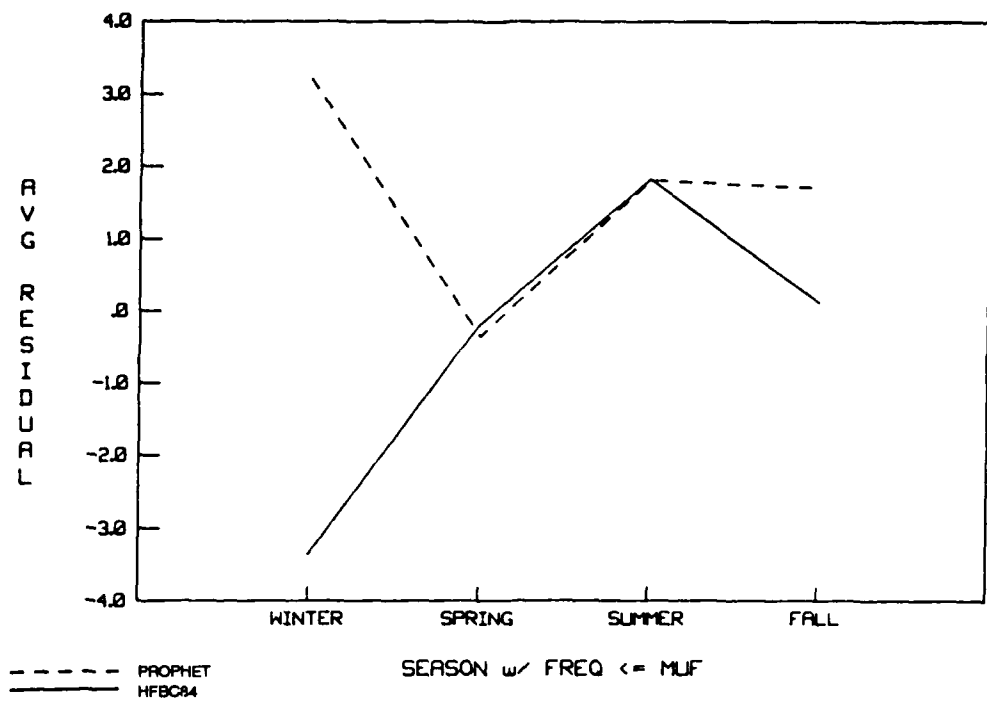


Figure 31. Average residual as a function of season for frequencies less than or equal to the MUF.

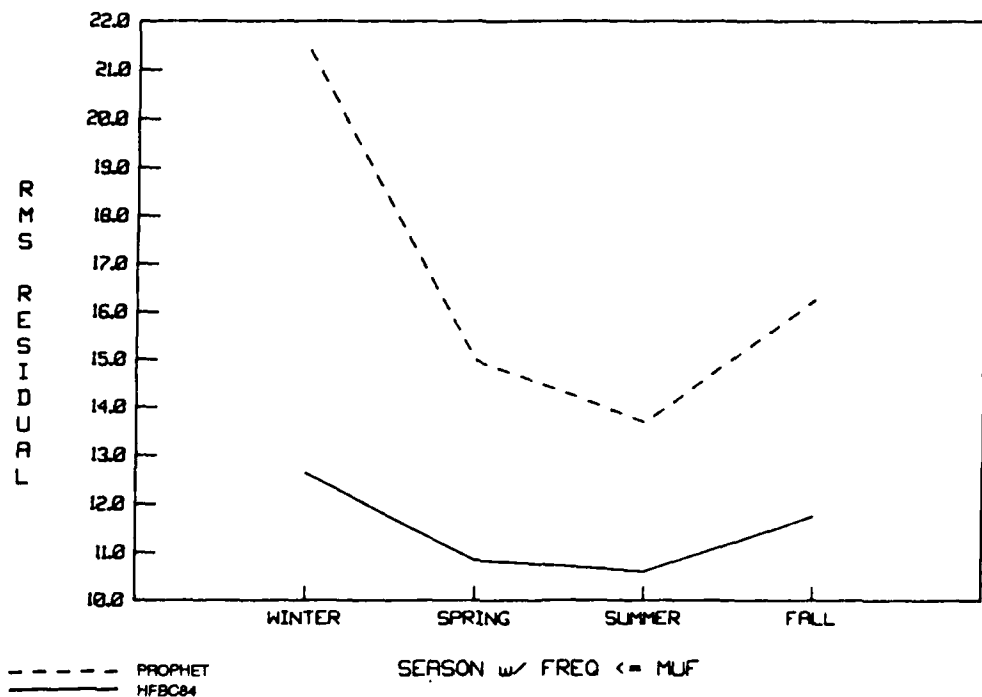


Figure 32. Root mean square residual as a function of season for frequencies less than or equal to the MUF.

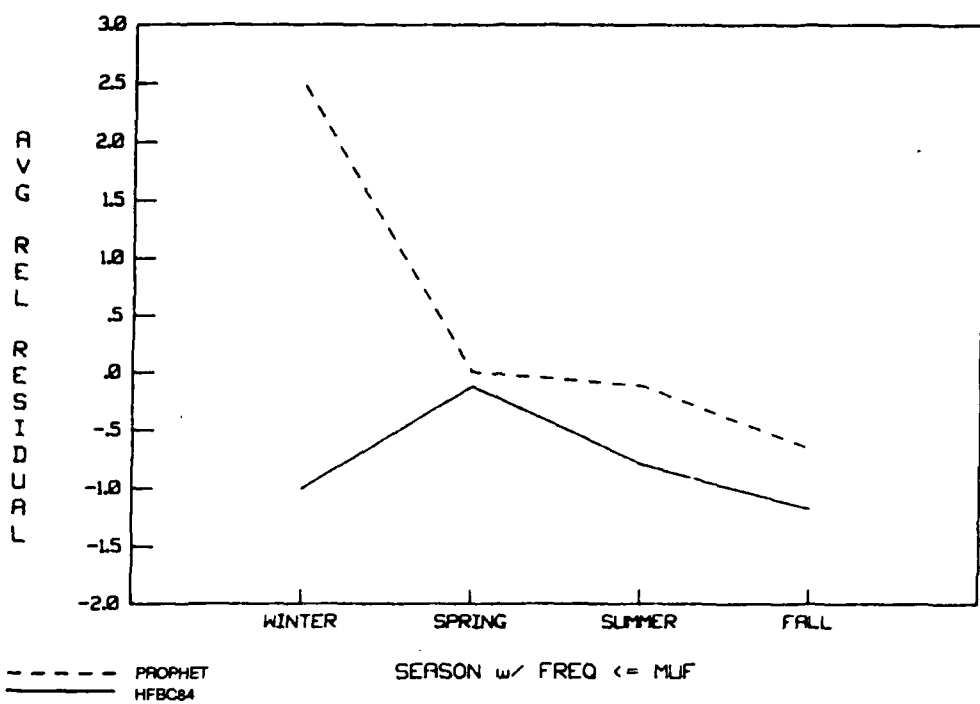


Figure 33. Average relative residual as a function of season for frequencies less than or equal to the MUF.

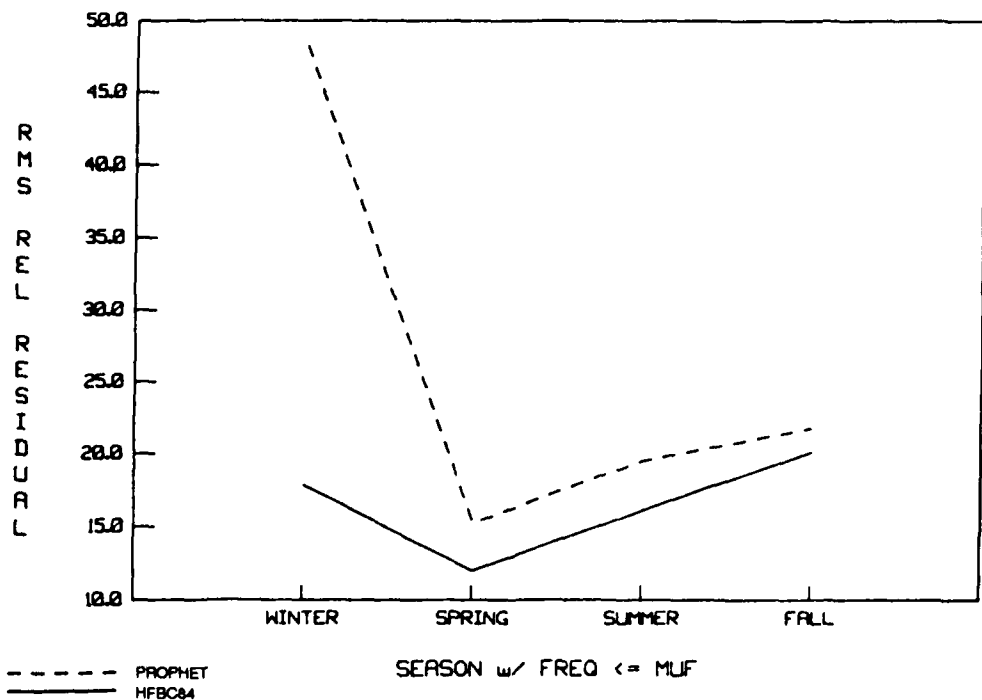


Figure 34. Root mean square relative residual as a function of season for frequencies less than or equal to the MUF.

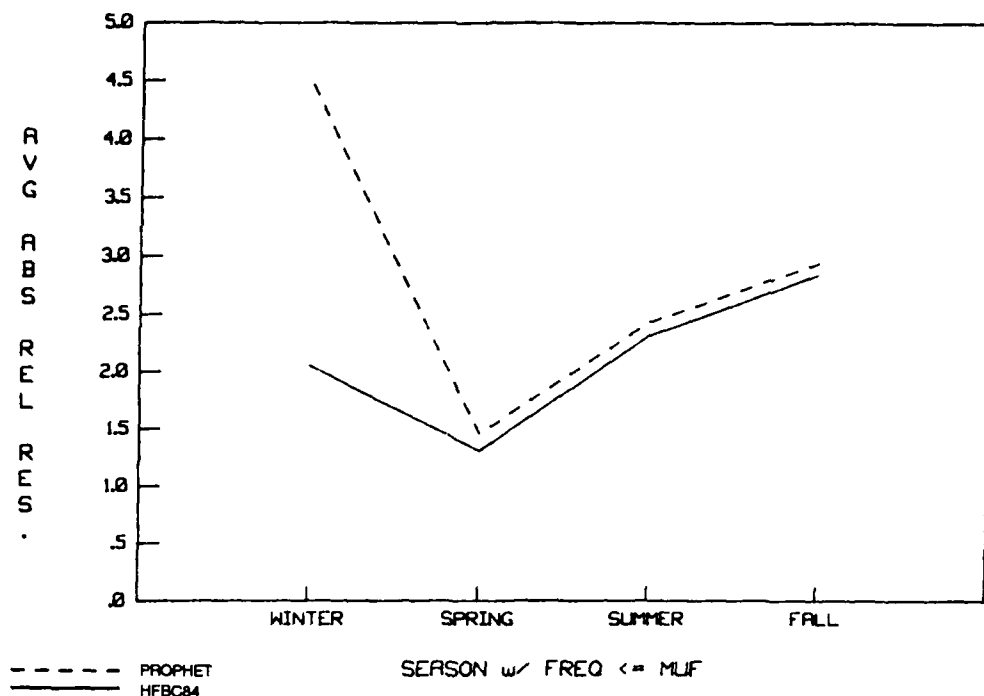


Figure 35. Average absolute relative residual as a function of season for frequencies less than or equal to the MUF.

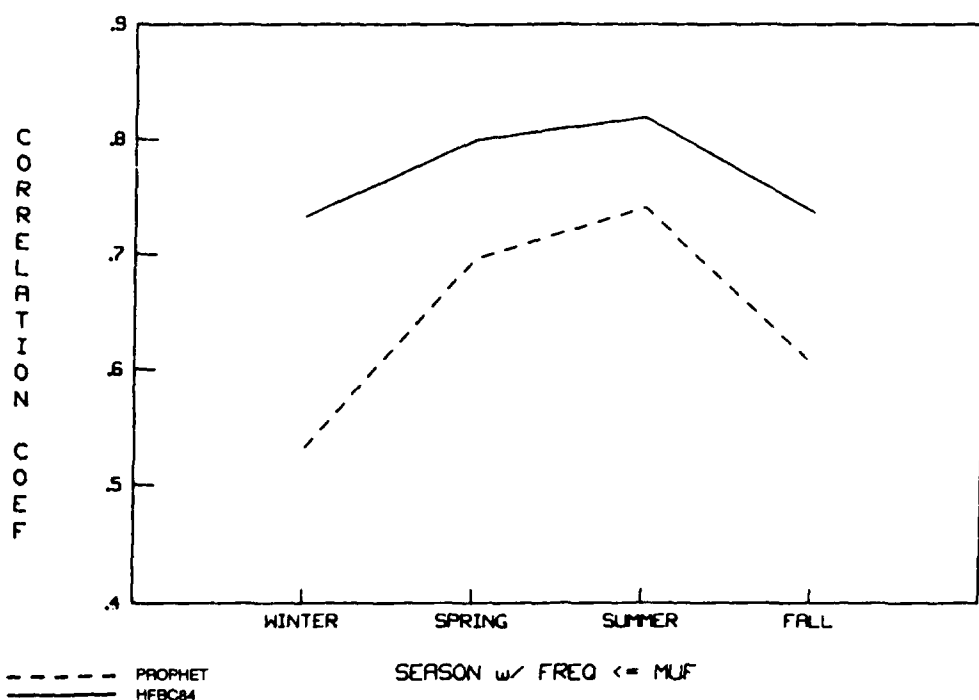


Figure 36. Correlation coefficient as a function of season for frequencies less than or equal to the MUF.

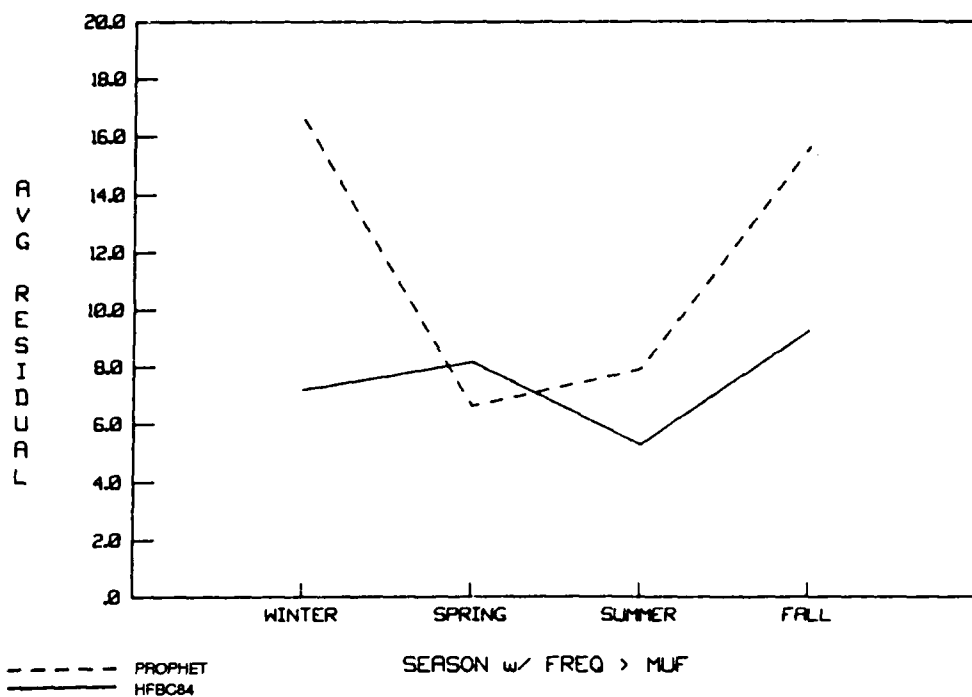


Figure 37. Average residual as a function of season for frequencies greater than the MUF.

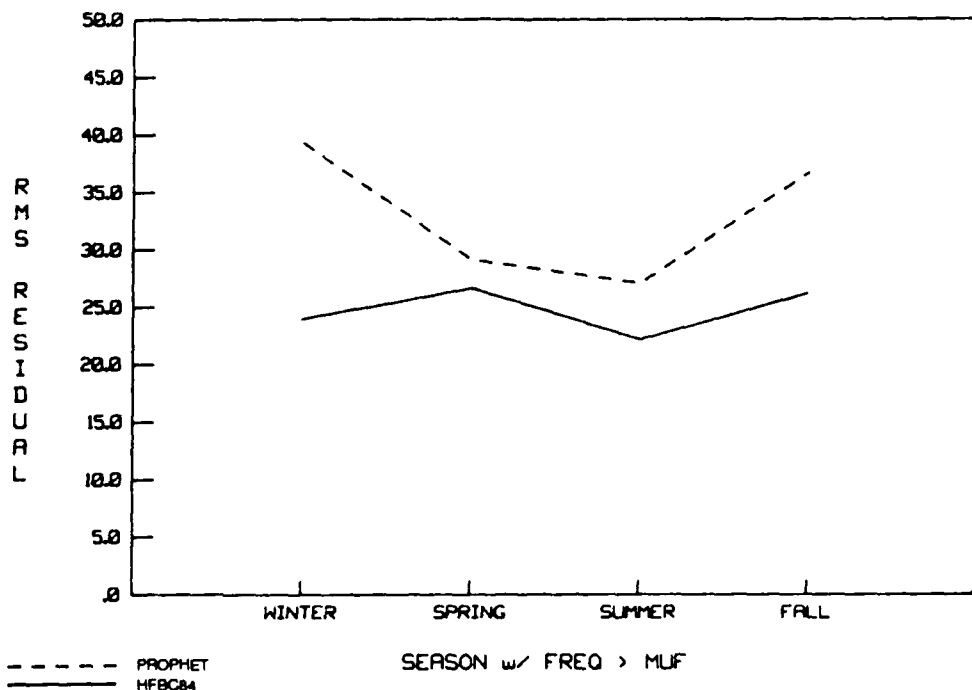


Figure 38. Root mean square residual as a function of season for frequencies greater than the MUF.

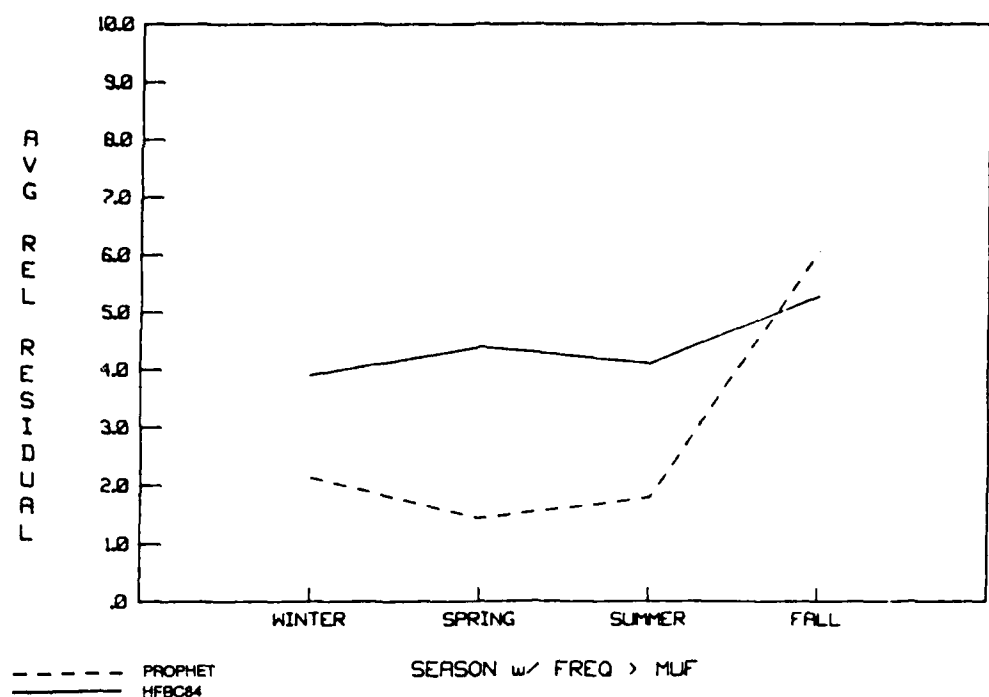


Figure 39. Average relative residual as a function of season for frequencies greater than the MUF.

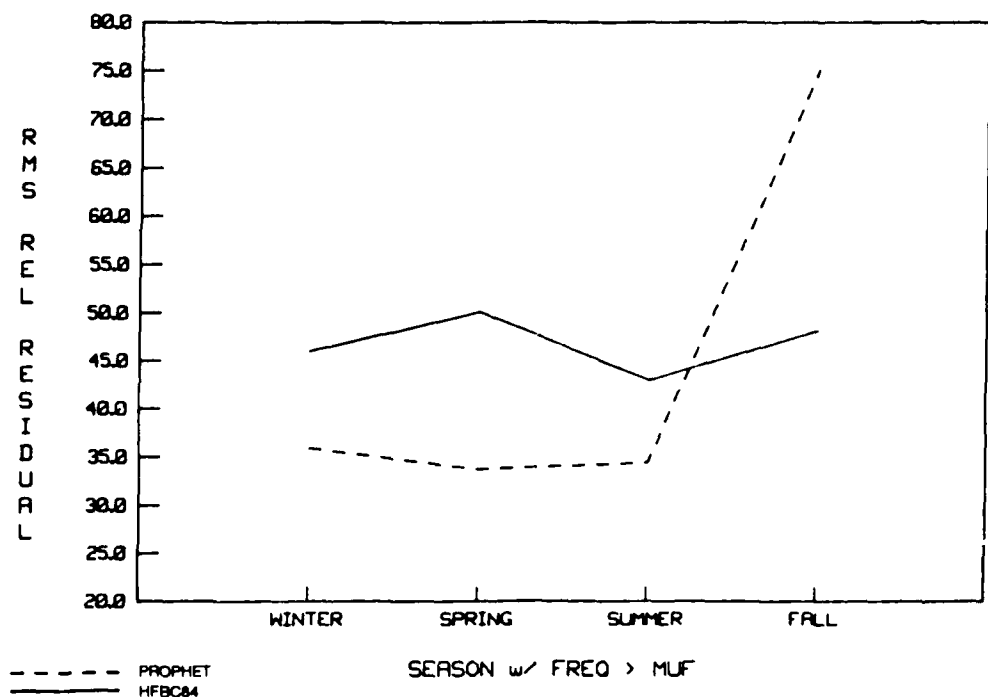


Figure 40. Root mean square relative residual as a function of season for frequencies greater than the MUF.

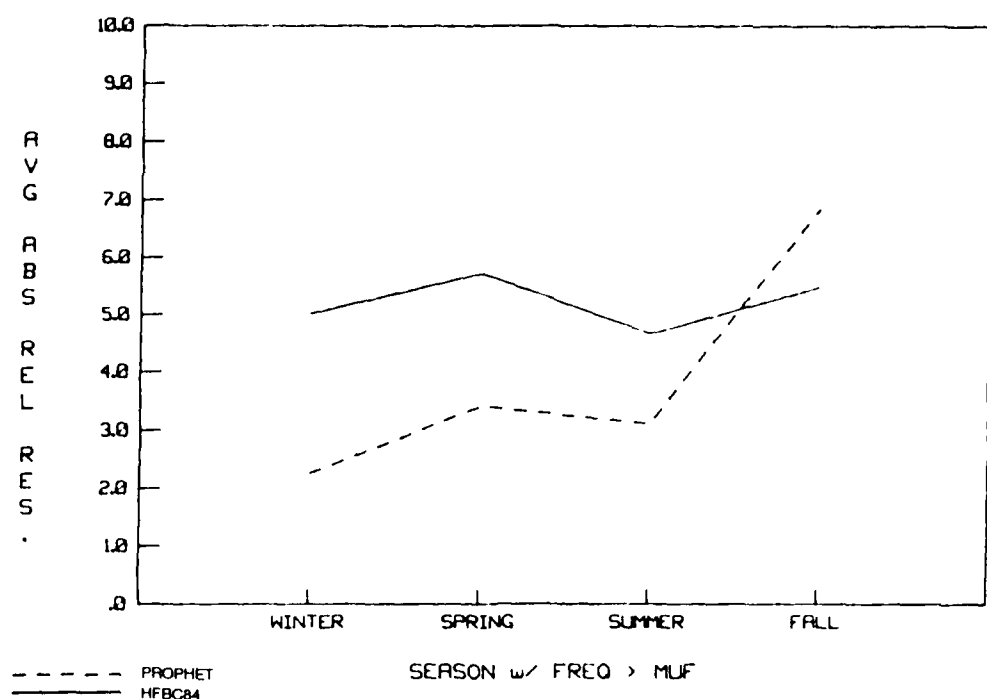


Figure 41. Average absolute relative residual as a function of season for frequencies greater than the MUF.

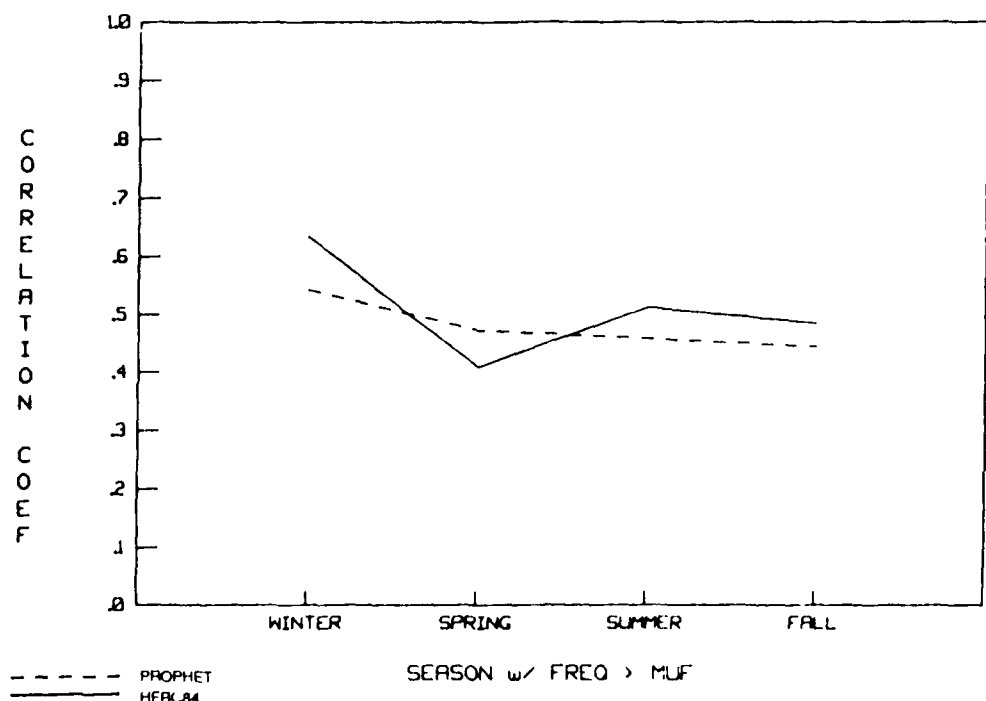


Figure 42. Correlation coefficient as a function of season for frequencies greater than the MUF.

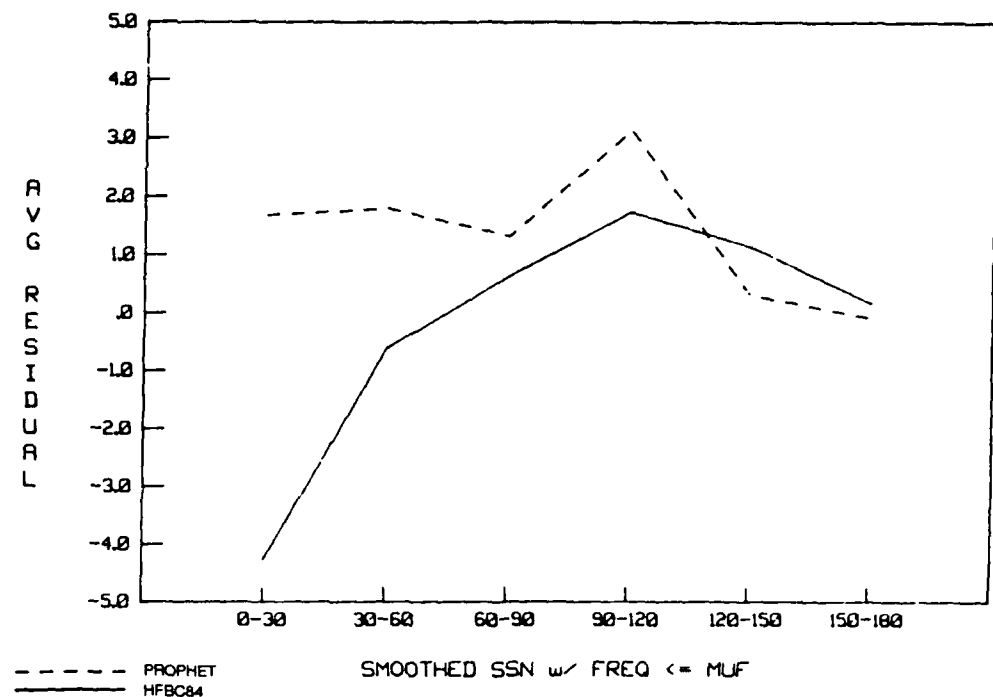


Figure 43. Average residual as a function of smoothed sunspot number for frequencies less than or equal to MUF.

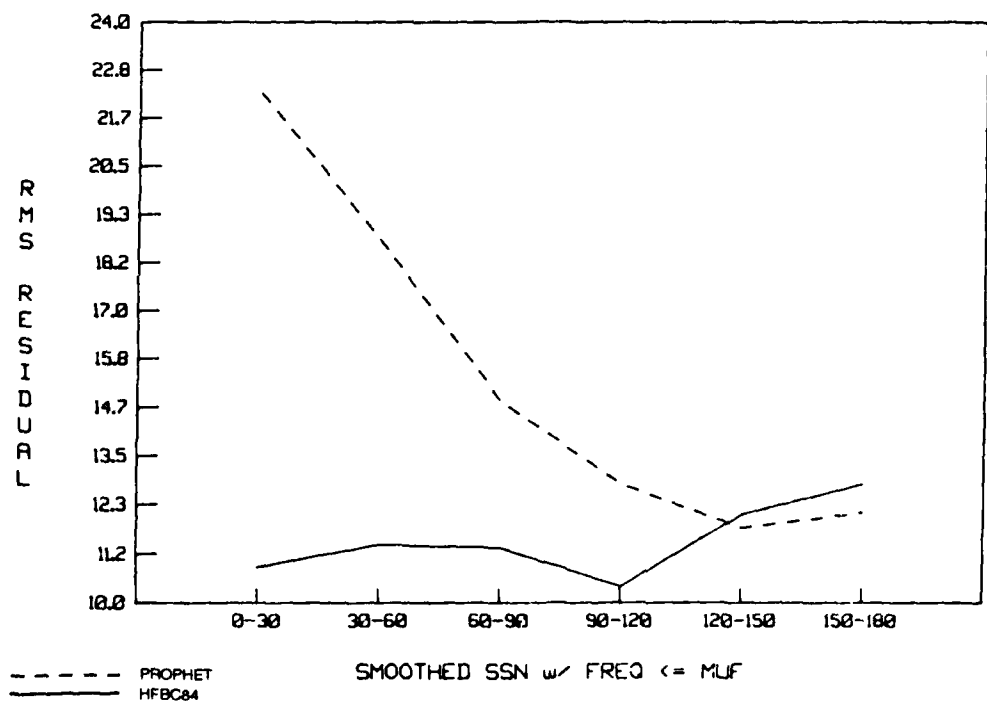


Figure 44. Root mean square residual as a function of smoothed sunspot number for frequencies less than or equal to MUF.

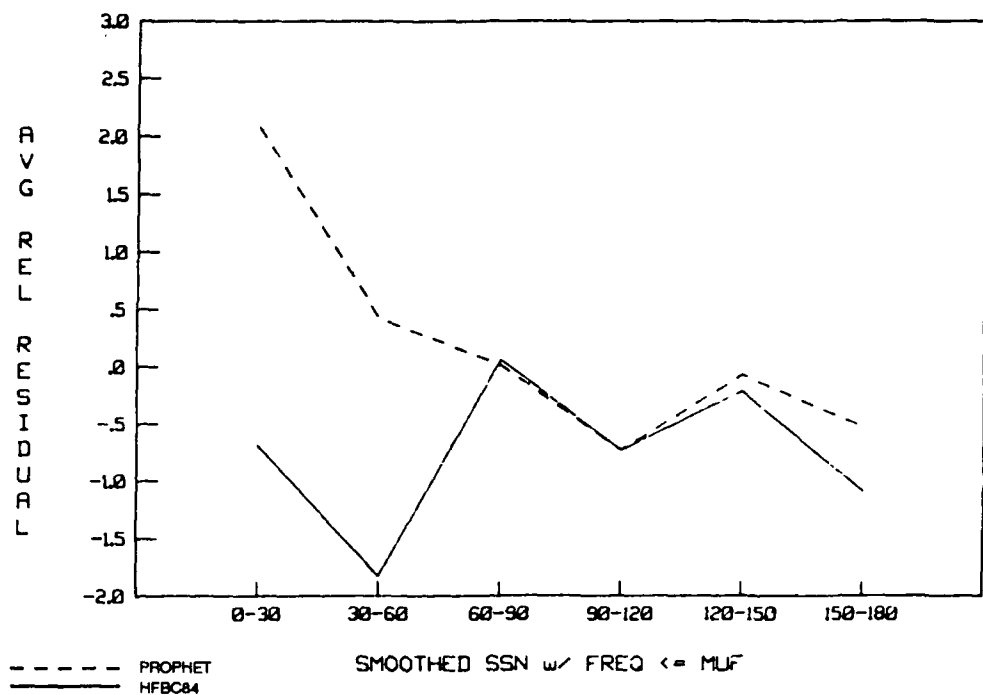


Figure 45. Average relative residual as a function of smoothed sunspot number for frequencies less than or equal to the MUF.

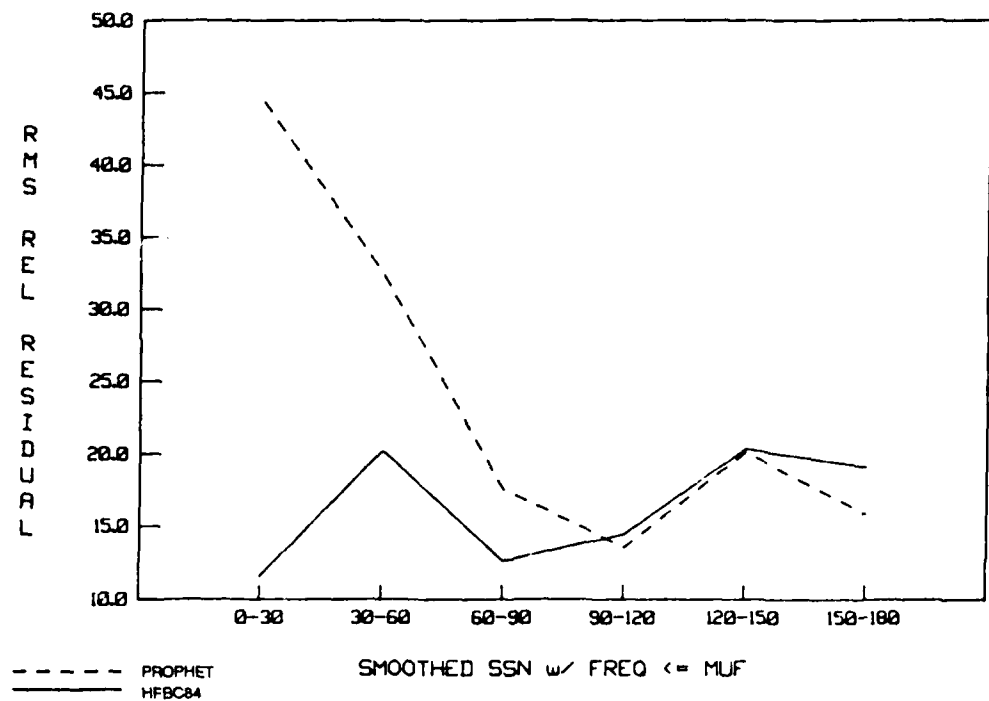


Figure 46. Root mean square relative residual as a function of smoothed sunspot number for frequencies less than or equal to the MUF.

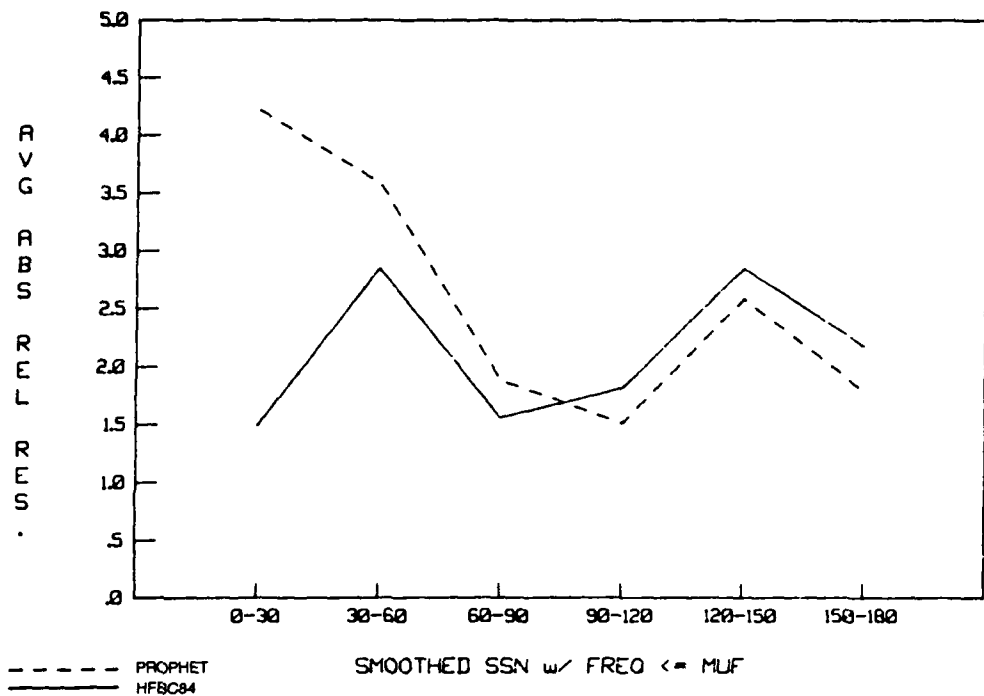


Figure 47. Average absolute relative residual as a function of smoothed sunspot number for frequencies less than or equal to the MUF.

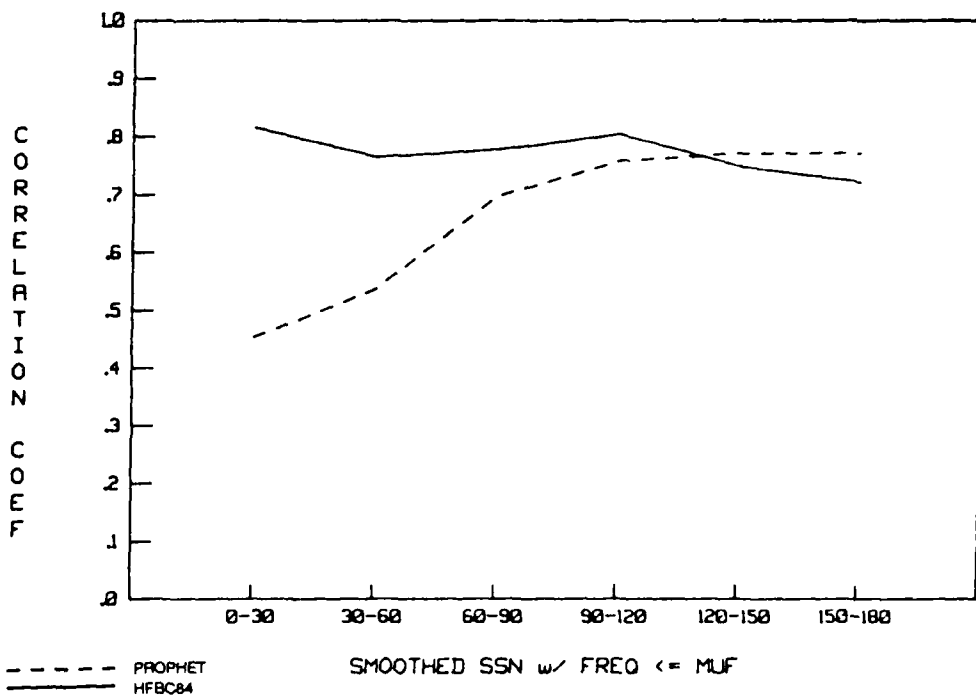


Figure 48. Correlation coefficient as a function of smoothed sunspot number for frequencies less than or equal to the MUF.

Figure 44, however, shows a definite dependence on R_{12} in the rms residual. Performance at low sunspot numbers is very poor in the PROPHET model, while HFBC84 is approximately uniform over all ranges.

The remaining statistical parameters are shown in figures 45 to 48. These figures show that the strongest dependence for field strength calculations may be for low sunspot numbers as, in each case, the performance of PROPHET improves for high sunspot numbers. In each case, HFBC84 performs quite well with only minor excursions in specific sunspot number ranges.

For completeness, we present in figures 49 to 54 the companion plots for frequencies greater than the MUF.

MIDPATH LOCAL TIME RESULTS

Lastly, to determine the adequacy of the time-dependent aspects of each model, we looked at the performance as a function of midpath local time. For long paths this comparison test may not be very informative. However, for short (1-hop) paths these results highlight deficiencies in the models.

Figure 55 shows the average bias as a function of midpath local time for frequencies less than the MUF. The figure shows a diurnal effect in PROPHET that causes overprediction in the morning hours (~12 dB) and underprediction in the afternoon and night (-12 dB). HFBC84 shows quite good results throughout the day.

Figures 56 to 59 show no clear trends in the other statistical quantities. Figure 57, however, shows a small effect similar to that seen in the residual. That is, a tendency to overpredict in morning hours and underpredict in afternoon and evening hours.

Figure 60 shows the correlation coefficient. In this figure we see that PROPHET shows fair performance during daylight and early evening hours. However, its nighttime performance is again quite poor.

Figures 61 to 66 show a companion set of figures for frequencies greater than the MUF. In this set of figures, neither model shows any clear systematic trends. For the most part, performance is equally poor in both cases.

In the next section we briefly discuss possible explanations for the results we have presented here. We also suggest areas of research to improve these results.

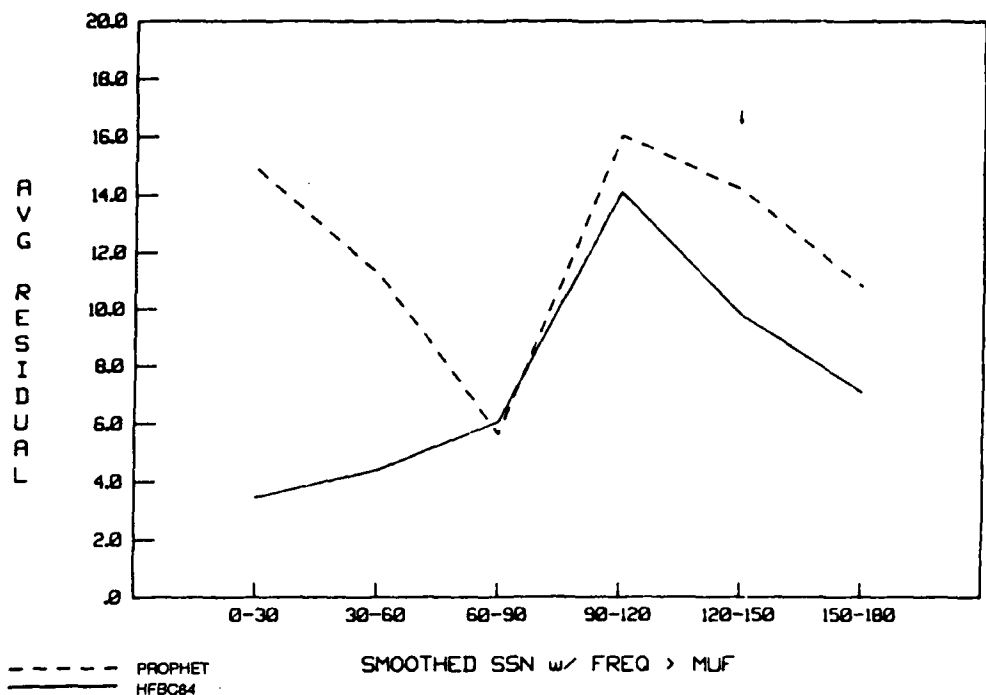


Figure 49. Average residual as a function of smoothed sunspot number for frequencies greater than the MUF.

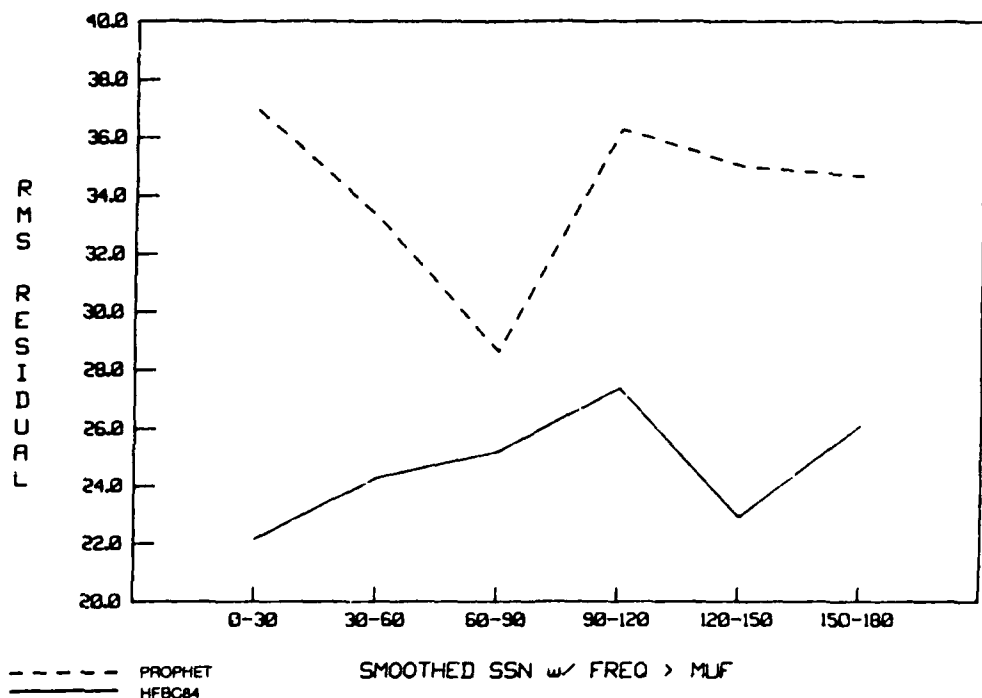


Figure 50. Root mean square residual as a function of smoothed sunspot number for frequencies greater than the MUF.

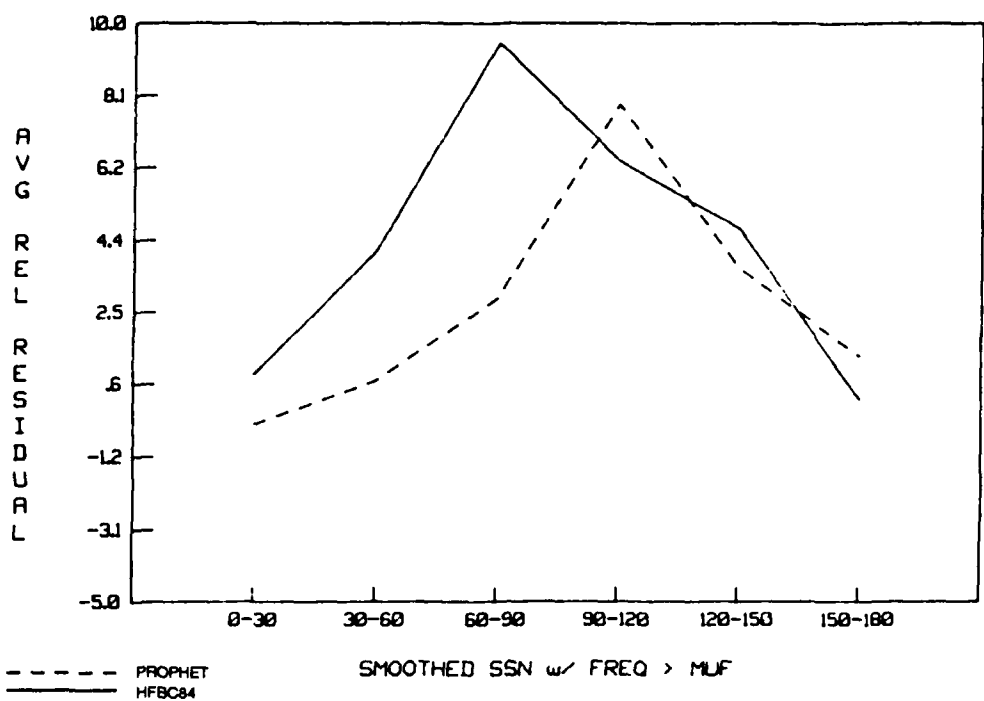


Figure 51. Average relative residual as a function of smoothed sunspot number for frequencies greater than the MUF.

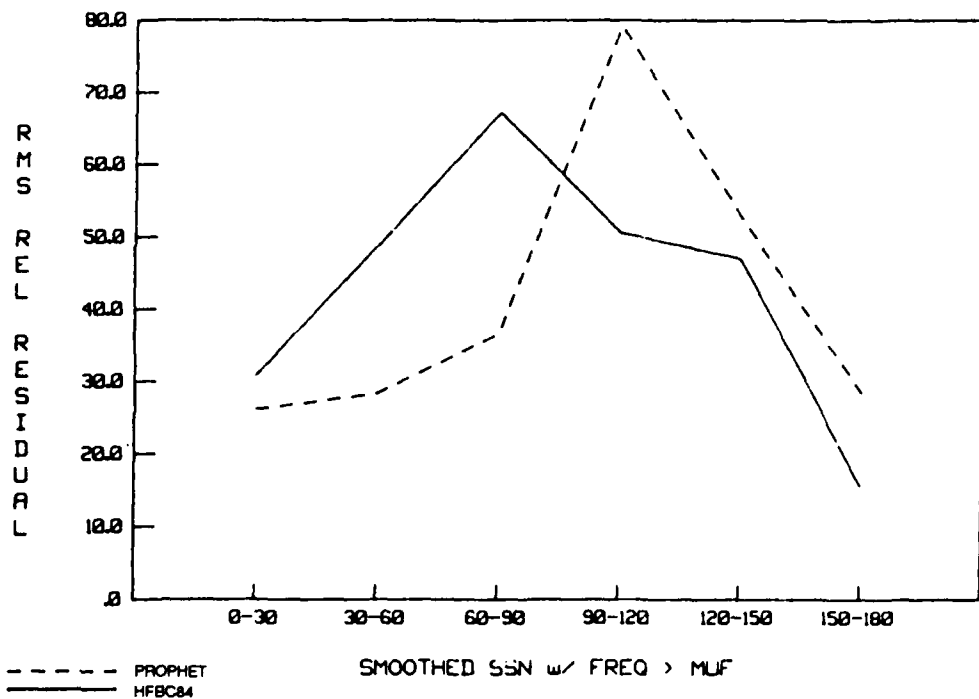


Figure 52. Root mean square relative residual as a function of smoothed sunspot number for frequencies greater than the MUF.

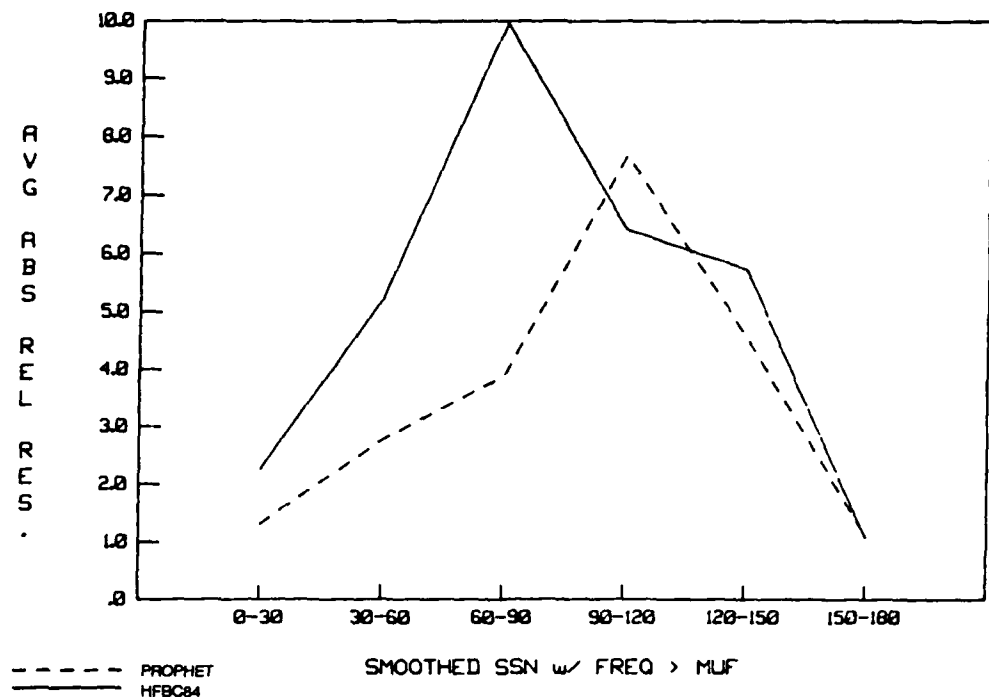


Figure 53. Average absolute relative residual as a function of smoothed sunspot number for frequencies greater than the MUF.

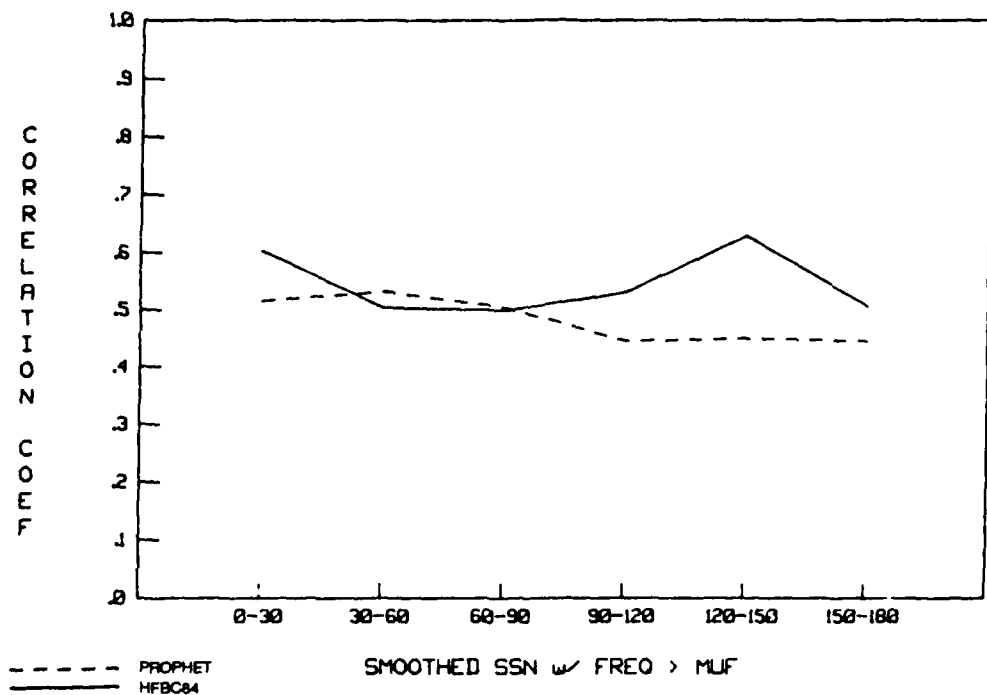


Figure 54. Correlation coefficient as a function of smoothed sunspot number for frequencies greater than the MUF.

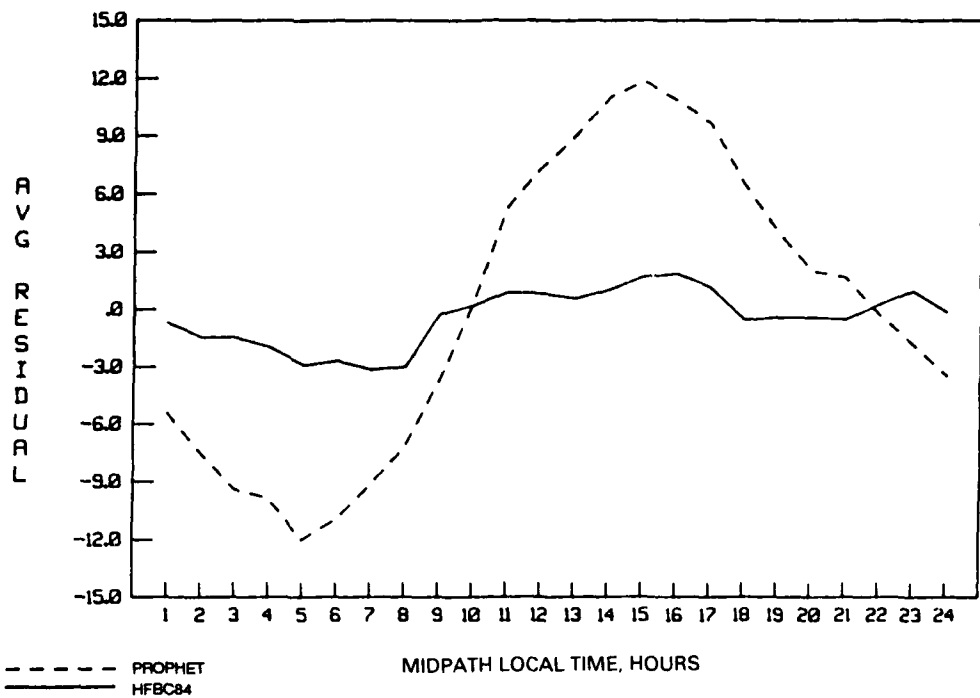


Figure 55. Average residual as a function of midpath local time for frequencies less than or equal to the MUF.

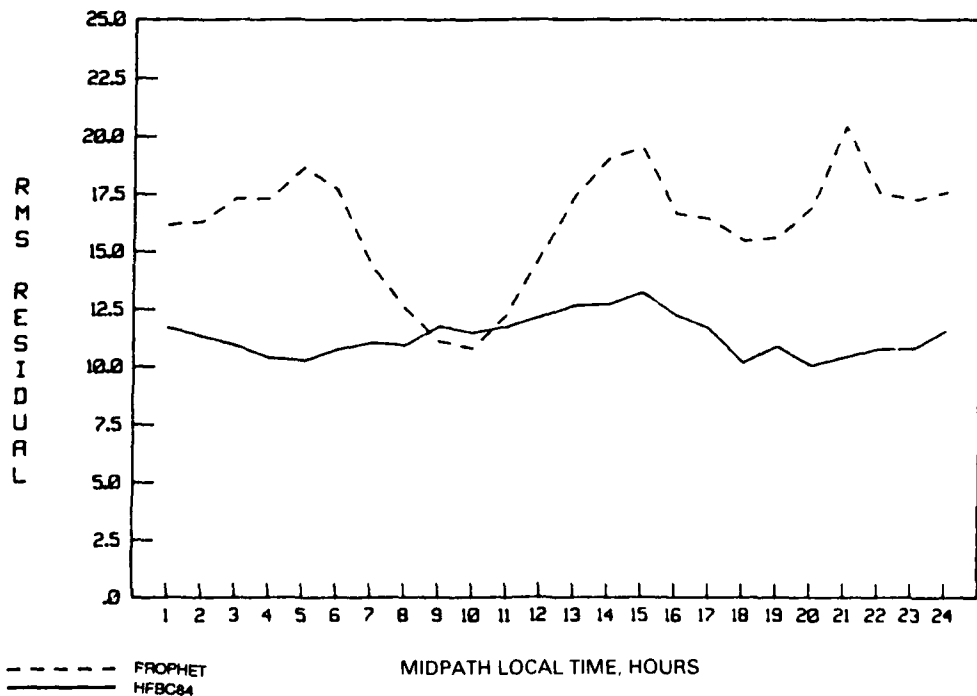


Figure 56. Root mean square residual as a function of midpath local time for frequencies less than or equal to the MUF.

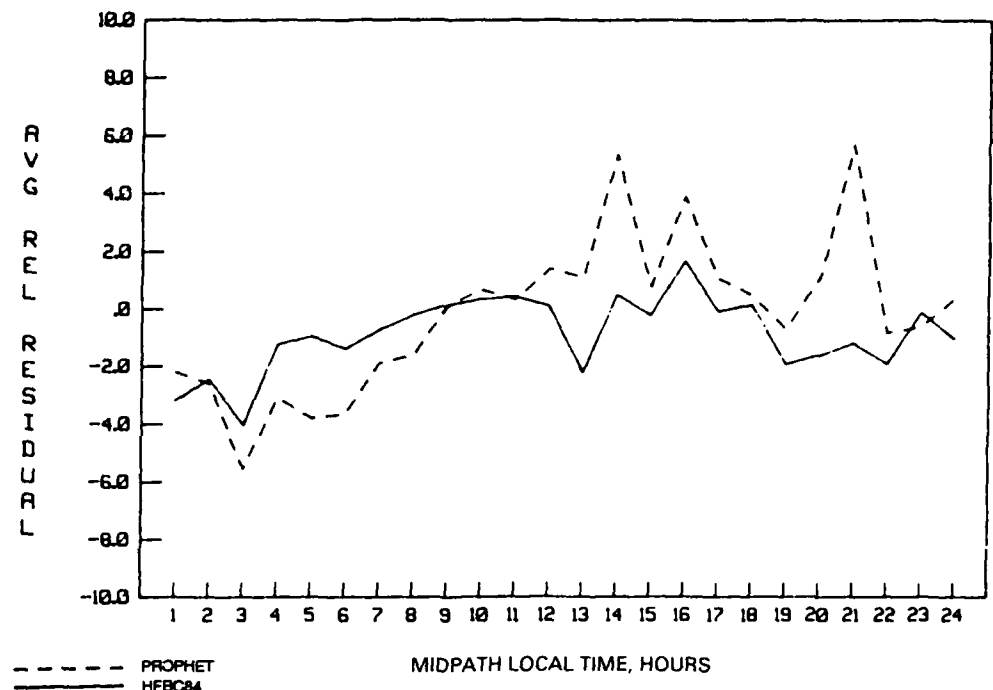


Figure 57. Average relative residual as a function of midpath local time for frequencies less than or equal to the MUF.

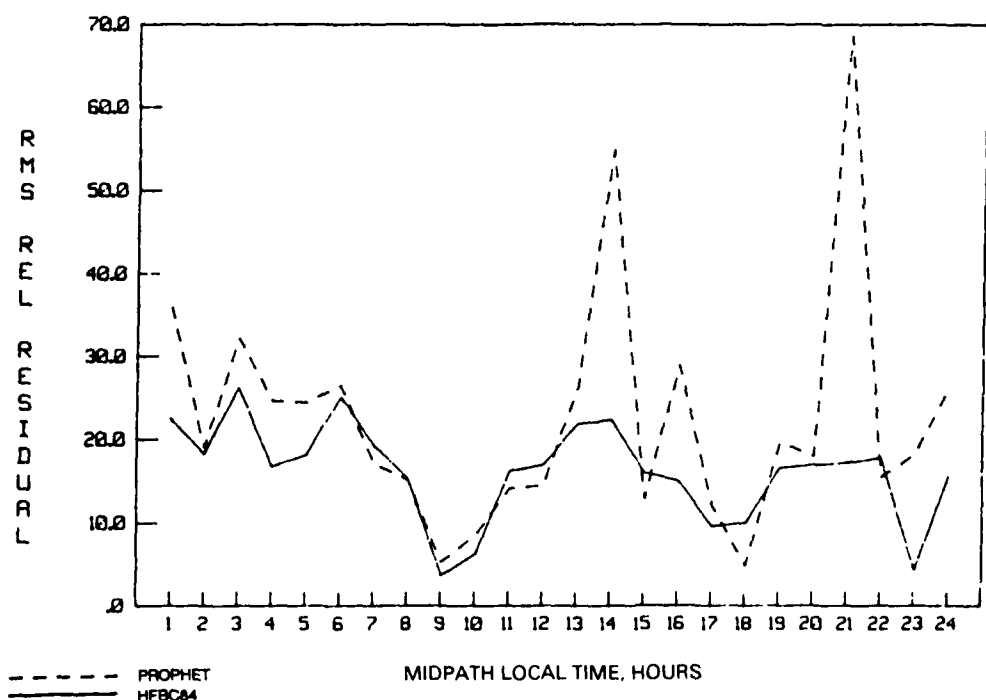


Figure 58. Root mean square relative residual as a function of midpath local time for frequencies less than or equal to the MUF.

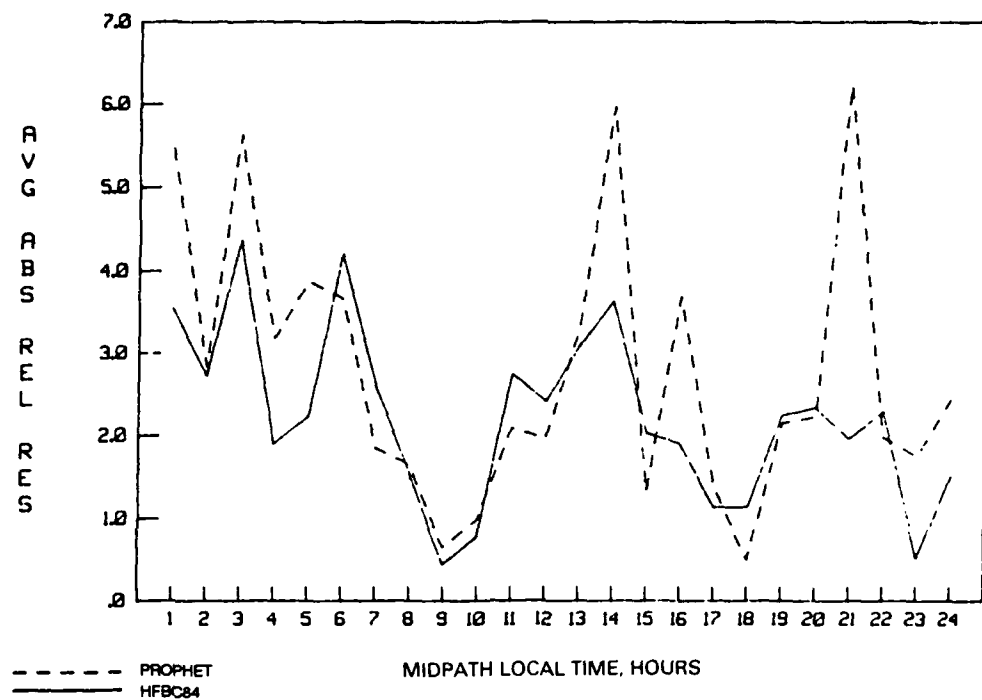


Figure 59. Average absolute relative residual as a function of midpath local time for frequencies less than or equal to the MUF.

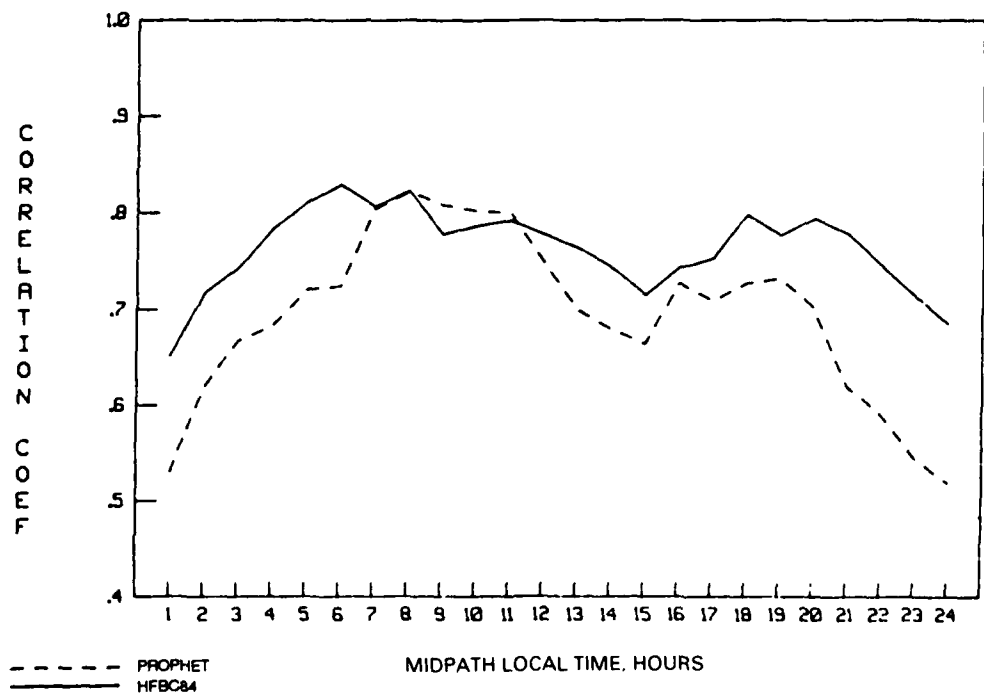


Figure 60. Correlation coefficient as a function of midpath local time for frequencies less than or equal to the MUF.

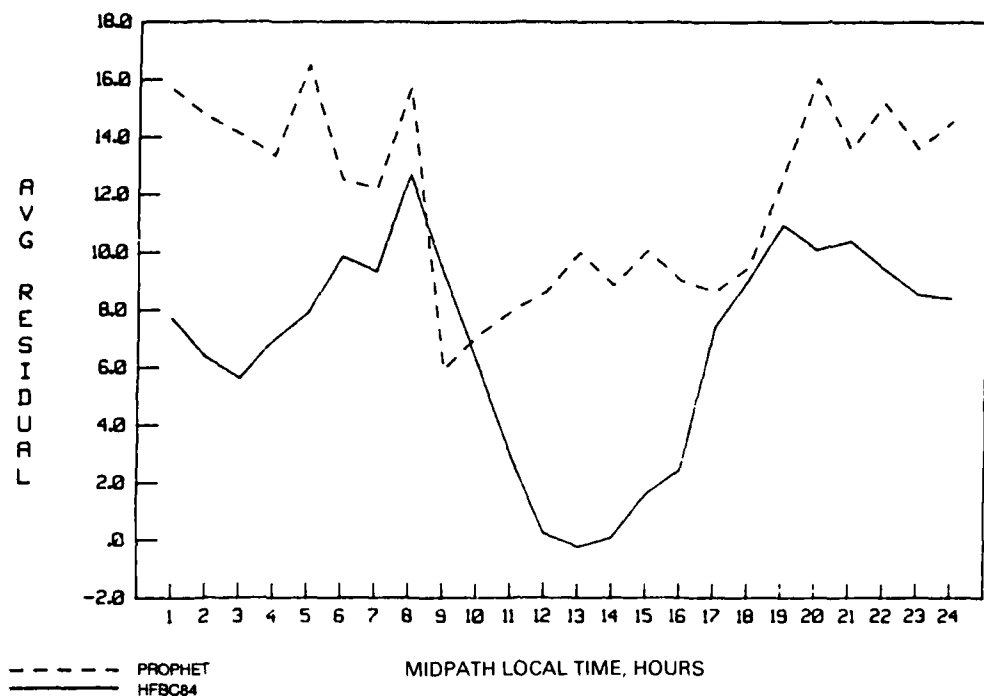


Figure 61. Average residual as a function of midpath local time for frequencies greater than the MUF.

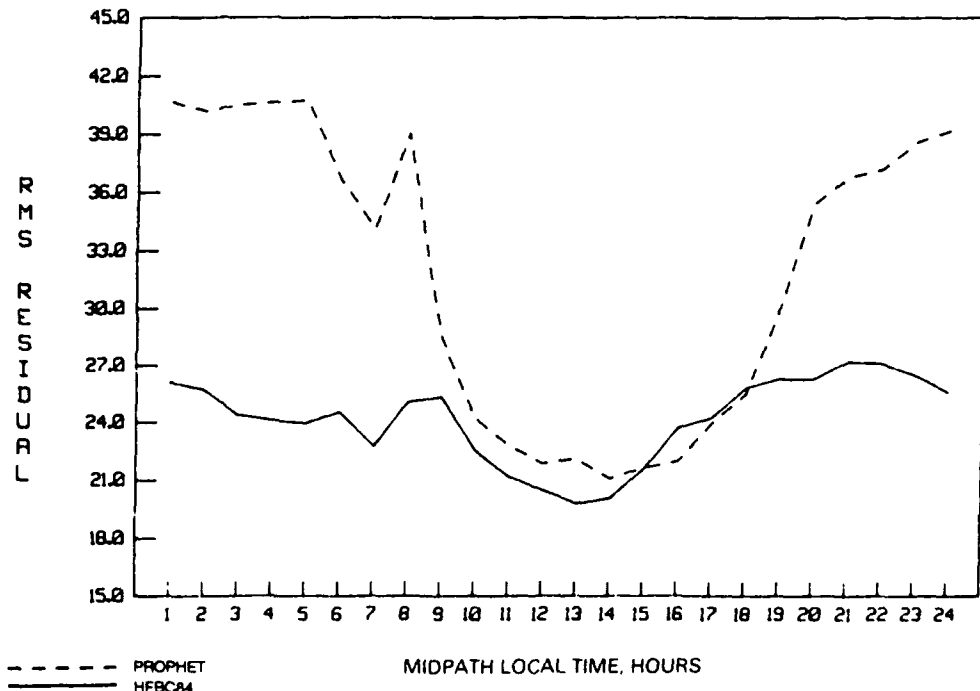


Figure 62. Root mean square residual as a function of midpath local time for frequencies greater than the MUF.

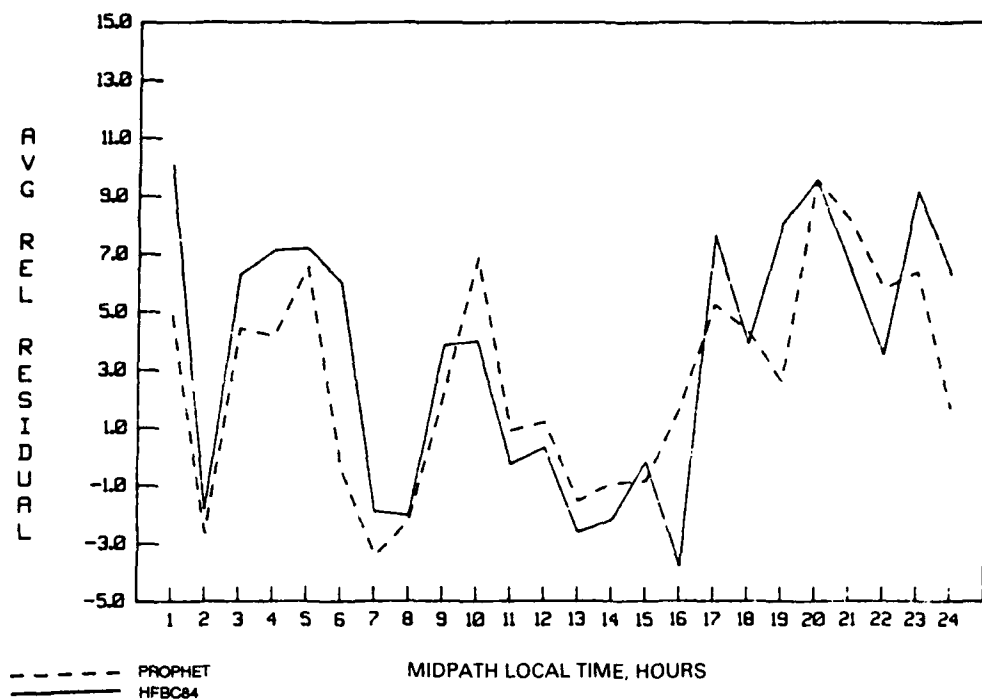


Figure 63. Average relative residual as a function of midpath local time for frequencies greater than the MUF.

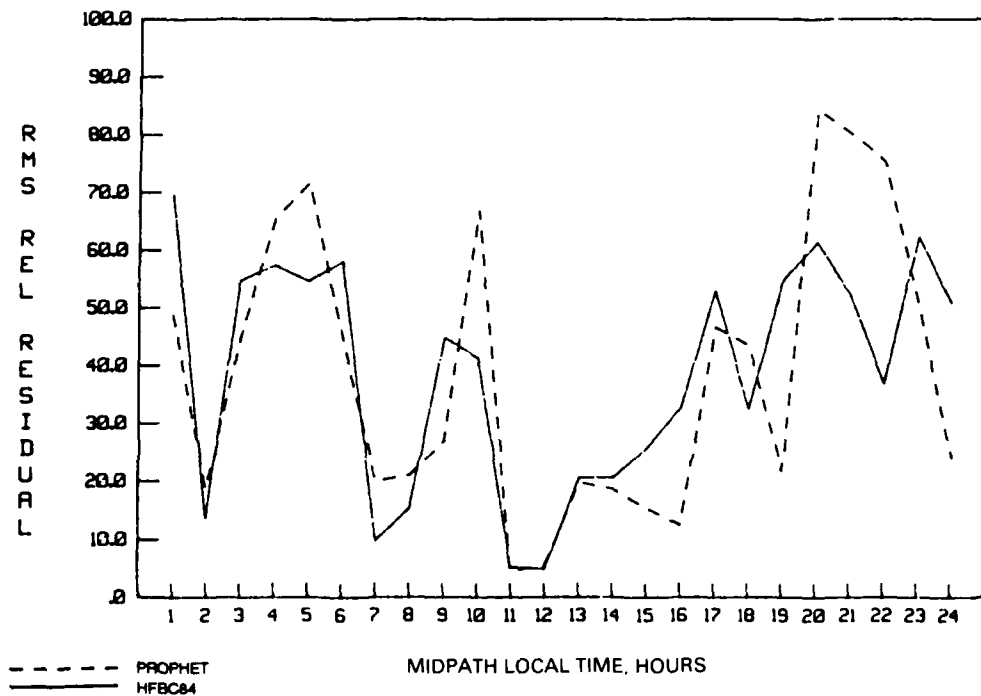


Figure 64. Root mean square relative residual as a function of midpath local time for frequencies greater than the MUF.

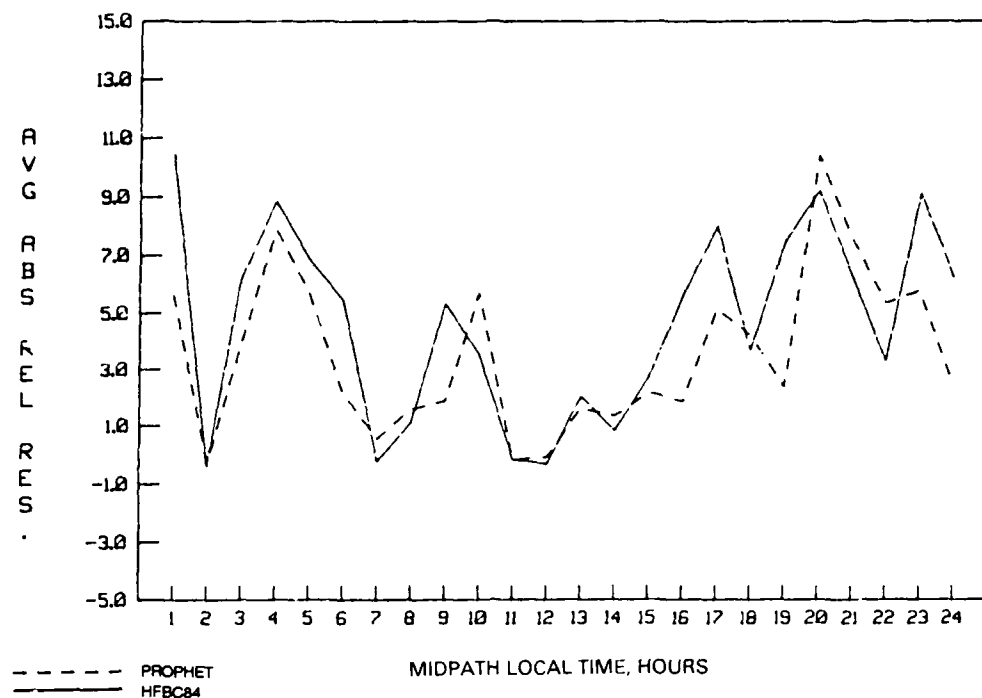


Figure 65. Average absolute relative residual as a function of midpath local time for frequencies greater than the MUF.

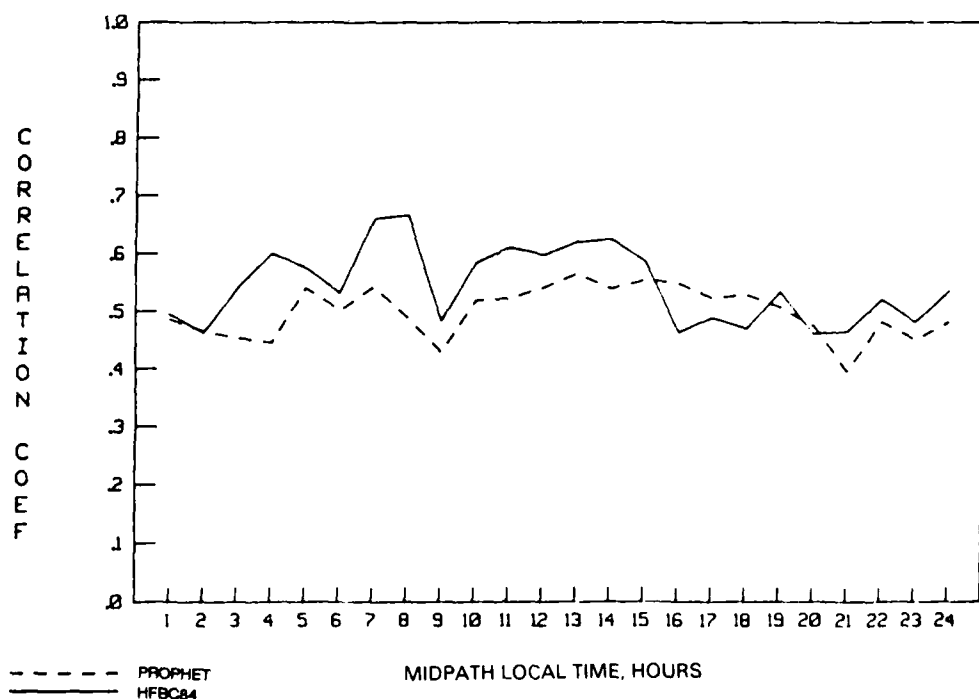


Figure 66. Correlation coefficient as a function of midpath local time for frequencies greater than the MUF.

DISCUSSION AND RECOMMENDATIONS

In the previous section we presented the results of a comparison of the PROPHET and HFBC84 field strength predictions to measured data. In this section we briefly discuss these results and present recommendations for future work aimed at improving them.

First, we should realize that comparison of predictions of monthly median field strengths to uncontrolled observed data, as we have done here, is, in some ways, a task of limited validity. Unlike ionospheric characteristics such as the MUF or $f_0 F2$, which are scaled from ionograms in the same way throughout the world, procedures used to obtain field strengths vary both in method and in quality.

An accurate measurement of received field strength requires detailed knowledge of the losses inherent in both receiving and transmitting systems. This includes cable and antenna feed losses at both ends of the circuit. In many cases such detailed knowledge is nonexistent.

Furthermore, to apply a correct antenna gain to a measured field strength we must know which mode (or modes) we are receiving. The gains are then determined by prediction programs that assign take-off angles to the mode ray. Any errors contained in the antenna gain patterns and in the propagation prediction programs are included in the quoted data value. These considerations make the worldwide collection of uncontrolled data for inclusion in a data base a questionable process. To then attempt to draw detailed conclusions from comparison of predictions to such data is a risky proposition, at best.

Aside from these considerations, the overall performance of the models tested in this report is quite poor. Specifically, we believe that the over-the-MUF prediction models require further investigations. While we usually work below the MUF in any operational communication system, an accurate prediction of usable field strength at frequencies greater than the MUF could be useful in certain scenarios.

Figures 1 to 6 show that both models perform poorly for frequency-to-MUF ratios greater than ~1.5. The fact that the average relative residual and absolute relative residual are identical in this range shows that the HFBC84 model consistently underpredicts the field strength in these cases. This result has been suspected before and shows up clearly here (private communication, David B. Sailors, 1986).

In figure 67 we show a comparison of the current CCIR over-the-MUF loss term, L_m , with a calculation based on the full Wheeler method, equation 27. Notice that the CCIR method shows a bias with respect to the full Wheeler method. We recommend a calculation based on this method be implemented in the CCIR model to assess its accuracy for over-the-MUF calculation.

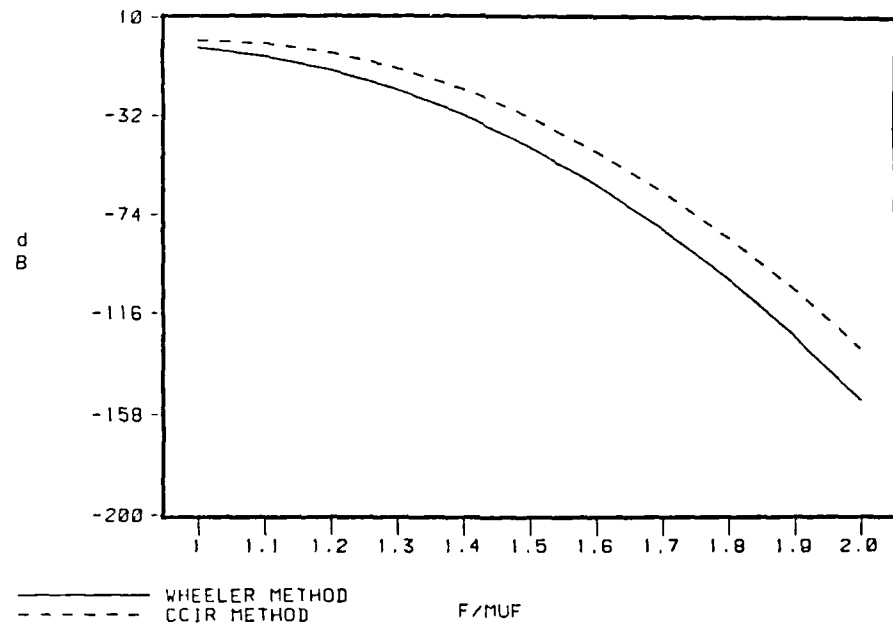


Figure 67. Comparison of full Wheeler method and current CCIR method for over-the-MUF loss.

At the same time, the PROPHET model similarly shows very poor results over the range of frequency-to-MUF ratios of ~1.5 and higher. This implies that the determination of the operational MUF using the HPF factor, which differs from the FTZ method, is not adequate. However, the poor performance of the long-path (FTZ) model in HFBC84, in general, shows this model may not be capable of providing accurate global predictions.

Given these considerations, we recommend that future work on the PROPHET field strength model be geared toward the implementation of an HFBC84-like model for paths less than approximately 7000 km. By this we mean a prediction scheme that separately models the various loss mechanisms and combines them, as in equation 3, to produce the field strength prediction.

A desirable feature of such a modeling scheme is that it provides a simple method for addition of other loss mechanisms that may be developed. Terms relating to these additional mechanisms can be simply added to equation 3.

In the same way, improved models for the existing loss mechanisms can be easily inserted and tested. For example, the PROPHET ionospheric absorption term used in QLOF and in the determination of f_L in the field strength model is quite accurate, we believe. It provides excellent performance in LUF predictions and may be preferable to the expression used in HFBC84.

Based on the results of the comparison, we recommend using the current PROPHET implementation of the FTZ model for paths greater than 7000 km. From figure 19 we see that, except for the very long paths where both models show poor results, PROPHET does quite well in terms of the average bias for paths up to ~10,000 km. Similarly, the rms residual, figure 20, for the PROPHET model is as good as, or better than, HFBC84 for the same path length ranges. Further work is needed at the very long path lengths where the problem is much more difficult due to multimode propagation and scattering that makes prediction difficult.

In summary, this report has highlighted the good and bad aspects of both prediction models. A combination of the best aspects of both into one model should lead to a prediction scheme which is fast, accurate, and will provide a reliable input into higher level models.

REFERENCES

- Argo, P.E., and Hill, J.R. (1977). *Lowest Observable Frequency (LOF) Model: Solrad Application*, Naval Electronics Laboratory Center Technical Document 3304 (Unpublished).
- Barghausen, A.F., Finney, J.W., Proctor, L.L., and Schultz, L.D. (1969). *Predicting Long-term Operational Parameters of High Frequency Sky-wave Telecommunications Systems*, ESSA Technical Report ERL-110-ITS 78, U.S. Government Printing Office, Washington.
- Beckmann, B. (1967). Notes on the relationship between the receiving-end field strength and the limits of the transmission frequency range MUF-LUF, *NTZ-Comm. J.*, 6(1), 37-47.
- Booker, H.G. (1984). *Cold Plasma Waves*, Martinus Nijhoff Publishers.
- Bradley, P.A., and Liu, R.Y. (1982). *An Evaluation of the FTZ Sky-wave Field-Strength Prediction Method*, Submission to CCIR XVIth Plenary Assembly, Study Group 6, IWP 6/1 Doc. 205.
- Bradley, P.A., Liu, R.Y., Lockwood, M., and Dick, M.I. (1982). *Above-the-MUF Loss*, Submission to CCIR XVIth Plenary Assembly, Study Group 6, IWP 6/1 and 6/12, IWP 6/1 Document 209.
- CCIR Interim Method for Estimating Sky-wave Field Strength and Transmission Loss At Frequencies Between the Approximate Limits of 2 and 30 MHz* (1970). CCIR Report 252-2, New Delhi.
- Damboldt, T. (1975), A comparison between the Deutsche Bundespost ionospheric HF radio propagation predictions and measured field strength, in *Radio Systems and the Ionosphere*. Ed. W.T. Blackband, 12-1, AGARD Conference Proceedings 173, Technical Editing and Reproduction Ltd. London.
- Davies, K. (1969). *Ionospheric Radio Waves*, Blaisdell Publishing Company.
- Dieminger, W., and Rose, G. (1961). Zum Feldstarkeverlauf am Rande der Toten Zone, (On the Variation of Field Strength Near the Border of the Skip Zone), *NYZ*, 14, 492-495.
- Lucas, D.L., and Haydon, G.W. (1966). *Predicting Statistical Performance Indexes for High Frequency Ionospheric Telecommunications Systems*, ESSA Technical Report IERI-ITSAL, U.S. Government Printing Office, Washington.
- Report by the Chairman, Interim Working Party 6/1 (1975). *Sky-wave Field Strength and Transmission Loss at Frequencies Above 1.5 MHz, Correction 1 to Document 6/18-E*.

Report to the Second Session of the Conference, World Administrative Radio Conference for the Planning of the HF Band (1984). First Session, Geneva, (1984).

Rose, R.B., and Martin, J.N. (1978). *MINIMUF-3: A Simplified HF MUF Prediction Algorithm*, (NOSC Tech. Doc. 201). San Diego: Naval Ocean Systems Center.

Roy, T.N., and Sailors, D.B. (1987). *HF Maximum Usable Frequency (MUF) Model Uncertainty Assessment* (NOSC Tech. Doc. 1184). San Diego: Naval Ocean Systems Center.

Sailors, D.B., and Moision, W.K. (1987). *Quiet Time Lowest Frequency Model Uncertainty Assessment* (NOSC Tech. Doc. 1189). San Diego: Naval Ocean Systems Center.

Sailors, D.B., Moision, W.K., and Brown, R.P. (1981). *Accuracy of High Frequency Maximum Usable Frequencies (MUF) Prediction* (NOSC Tech. Doc. 695). San Diego: Naval Ocean Systems Center.

Sailors, D.B., Sprague, R.A., and Rix, W.H. (1986). *MINIMUF-85: An Improved HF MUF Prediction Algorithm*, (NOSC Tech. Doc. 1121). San Diego: Naval Ocean Systems Center.

Schultz, L.D., and Gallet, R.M. (1970). *A Survey and Analysis of Normal Ionospheric Absorption Measurements Obtained from Radio Pulse Reflection*, ESSA Professional Paper 4, U.S. Government Printing Office, Washington.

Second CCIR Computer-based Interim Method for Estimating Sky-wave Field Strength and Transmission Loss at Frequencies Between 2 and 30 MHz (1978). CCIR, Supplement to Report 252-2, Kyoto.

Wakai, N. (1961). Non-deviative Absorption at Night, *J. Radio Res. Labs.*, Japan, 8 (37), 213-218.

Wheeler, J.L. (1966). Transmission Loss for Ionospheric Propagation Above the Standard MUF, *Radio Science*, 1 (11), 1303-1308.

APPENDIX A

OVERALL RESULTS

This appendix presents overall results in tabular form for the cases investigated in this report. In each table, the average residual, rms residual, average relative residual, rms relative residual, average absolute relative residual, and correlation are given for each condition. The values given in the table are in the form HFB84/PROPHET.

TABLES

A-1.	Summary of results as a function of a frequency-to-MUF ratio for entire data base	A-2
A-2.	Summary of results as a function of circuit for entire data base	A-3
A-3.	Summary of results as a function of circuit length for entire data base	A-5
A-4.	Summary of results as a function of season for entire data base	A-6
A-5.	Summary of results as a function of smoothed sunspot number for entire data base	A-6
A-6.	Summary of results as a function of midpath local time for entire data base	A-7

Table A-1. Summary of results as a function of frequency-to-MUF ratio for entire data base.

CONDITIONS	Avg Residual	RMS Residual	Avg Rel. Res.	RMS Rel. Res.	Avg Abs. Rel. Res.	Correlation	%
.2	-5.5	55.1	14.4	71.2	7.4	.88	.3
.3	-7.1	15.5	12.4	85.2	3.6	.67	2.5
.4	1.1	6.2	12.2	24.3	10.6	.76	2.9
.5	1.8	3.6	12.5	19.9	3.3	.75	8.6
.6	1.5	2.9	11.1	20.5	1.7	.77	9.4
.7	1.6	1.6	13.1	15.9	2.9	.73	12.4
.8	1.0	1.0	10.6	32.5	3.3	.73	11.8
.9	-2.5	10.5	15.6	14.2	2.0	.69	12.7
1.0	-3.1	4.7	11.0	13.7	1.6	.69	11.0
1.1	-6.1	5.5	13.3	19.7	2.8	.60	10.6
1.2	-9.1	5.0	16.3	16.5	2.0	.81	9.5
1.3	-10.8	6.2	16.2	14.5	2.1	.83	9.9
1.4	-10.9	6.5	17.2	17.9	1.5	.84	7.7
1.5	-8.6	5.1	14.9	17.5	2.1	.81	6.4
1.6	13.1	4.7	12.6	16.5	2.4	.75	5.4
1.7	27.8	3.5	17.8	16.1	1.3	.78	4.5
1.8	40.6	4.9	30.2	14.5	1.4	.71	3.9
1.9	42.2	9.0	43.4	16.4	1.1	.71	2.8
2.0	39.6	14.9	40.5	19.9	1.5	.72	2.8
2.5	36.2	31.6	37.3	23.0	1.1	.59	2.1
3.0	31.5	66.7	32.4	34.8	1.1	.66	1.0
3.5	28.5	83.1	29.1	68.5	1.1	.66	1.0
4.0	25.0	82.3	25.3	83.5	1.1	.66	1.0
4.5	21.6	80.3	22.5	80.5	1.1	.66	1.0
5.0	20.4	75.9	21.0	76.2	1.0	.66	1.0
>5.0	18.4	73.8	19.2	73.9	.9	.57	.2

Table A-2. Summary of results as a function of circuit for entire data base.

CONDITIONS	Avg Residual	RMS Residual	Avg Rel Res.	RMS Rel Res.	Avg Abs Res.	Avg Rel Res.	Correlation	%
1	-3.8	13.6	7.6	15.7	.2	.4	.5	.15
2	-13.7	-7.9	14.7	10.0	-4.3	25.2	4.3	.84
3	2.0	10.3	8.3	3.2	-5.0	1.1	2.4	.88
4	-1.5	3.1	3.1	3.2	0.0	.1	.3	.69
5	23.5	23.8	38.3	4.4	4.7	50.8	5.6	.78
6	8.7	21.4	13.4	9.7	4.0	64.4	5.0	.32
7	22.9	12.5	23.8	7.2	.6	22.0	12.5	9.5
8	20.9	28.7	37.7	7.5	6.5	54.1	6.6	.59
9	18.0	31.2	32.5	2.4	6.5	61.3	7.8	.40
10	1.6	19.8	22.1	4.9	1.5	6.6	6.3	.40
11	1.6	1.8	15.4	8.7	-2.2	2.9	4.1	.39
12	-6.8	-12.0	7.8	13.1	-3.2	53.0	6.9	.78
13	-2.3	-1.0	11.6	9.2	-1.8	1.4	.7	.78
14	-3.5	-2.3	7.8	8.5	-2.2	14.5	6.5	.62
15	14.7	7.4	23.1	36.0	-2.5	35.0	16.5	.62
16	7.1	7.6	8.4	8.0	-8.0	9.1	6.1	.58
17	8.0	5.5	10.9	11.8	.3	1.4	.4	.54
18	-5.0	4.8	7.3	5.5	.2	1.0	2.2	.68
19	7.1	20.1	9.5	23.5	-2.0	18.3	36.5	.59
20	22.5	22.7	23.2	23.4	-3.4	7.3	5.6	.59
21	-9.5	-12.6	11.9	14.2	-31.4	-35.0	1.0	.14
22	16.0	22.7	16.3	22.9	-1.4	.4	31.4	.35
23	8.0	17.0	8.1	17.3	.2	.5	1.0	.08
24	26	13.5	23.5	23.4	-1.0	1.4	1.4	.00
25	27	23.4	13.9	23.6	-0.6	1.4	1.6	.04
26	6.3	-8.0	17.9	9.4	-7	1.0	.7	.52
27	9.0	-4	13.1	4.4	-3.0	1.5	.4	.67
28	-2.7	-3.2	12.4	8.2	-1.3	4.1	1.2	.0
29	-12.1	-13.0	12.6	13.5	-1.0	1.1	1.2	.0
30	32	1.0	-3.8	0	-1.0	1.1	1.2	.0
31	33	-8	-7.8	1.8	0.0	1.2	1.2	.0
32	5.7	2.4	10.7	9.9	0.1	1.3	1.3	.00
33	14.6	10.7	21.7	15.1	-6.6	1.0	2.2	.25
34	1.3	6	15.8	16.9	-7.4	42.5	38.5	.72
35	3.1	5.9	20.0	16.9	-1.1	20.0	18.4	.66
36	37	-1.4	7.8	6.5	.2	.3	.2	.49
38								.53

Table A-2. Summary of results as a function of circuit for entire data base
(continued).

CONDITIONS	Avg Residual	RMS Residual	Avg Rel. Res.	RMS Rel. Res.	Avg Abs Rel. Res.	Correlation	%
39	-22.3	-3.7	8.6	-3.5	24.7	3.5	.43
42	16.2	11.3	17.3	12.1	26.0	3.5	.80
43	6.3	15.9	13.0	20.0	3.2	1.4	.05
44	22.0	29.0	22.4	29.7	.6	1.3	.10
45	-7.1	-11.1	14.1	19.0	.8	1.8	-.43
46	-27.2	-22.8	27.8	13.8	13.9	1.9	6.2
47	-5.0	-4.8	7.0	8.5	2.4	2.4	-.87
48	-4.3	13.0	11.9	15.5	1.1	1.1	.60
51	52	4.1	11.6	17.4	2.0	2.9	5.8
53	7.6	-6.1	15.5	16.0	1.9	1.9	1.4
54	33.4	34.9	34.2	38.4	2.9	2.9	3.5
55	14.0	20.4	3.7	20.7	4.5	4.5	5.3
56	57	18.1	11.0	19.3	14.4	1.4	1.4
58	7.5	-7.5	2.2	9.4	9.1	9.1	1.0
59	-5.4	-21.0	2.0	8.5	22.1	2.1	-.19
60	5.1	1.6	-22.7	10.9	6.0	6.0	-.26
61	16.0	2.0	16.6	6.8	1.4	1.4	-.04
62	63	14.2	-9.8	4.5	10.5	1.1	-.04
64	14.4	8.7	8.5	15.0	10.4	1.4	1.00
65	13.2	3.0	-1.0	13.6	6.2	1.2	1.00
66	67	12.3	6.1	13.6	16.2	1.4	1.00
68	35.0	31.3	35.0	31.4	6.5	5.1	1.00
70	71	24.8	16.0	24.8	16.2	1.6	1.00
72	17.3	-3.7	20.9	11.2	6.7	10.6	1.00
73	18.1	-9	21.1	12.2	7.1	1.8	1.00
74	20.3	10.9	21.4	12.5	2.4	1.6	1.00
75	24.7	9.0	24.9	9.3	2.2	1.8	1.00
76	28.0	8.5	29.7	9.5	3.0	3.3	1.00
77	19.7	8.5	12.0	13.6	1.3	1.4	1.00
78	12.2	42.0	14.4	56.5	1.2	7.3	1.00
79	21.8	14.8	13.4	18.0	-1.8	6.5	1.00
80	9.3	8	13.6	26.0	-3.5	3.3	1.00
81	7.2	7.0	9.4	26.0	-2.6	1.1	1.00

Table A-3. Summary of results as a function of circuit length for entire data base.

CONDITIONS	Avg Residual	RMS Residual	Avg Rel. Res.	RMS Rel. Res.	Avg Abs. Rel. Res.	Correlation %
0-1	5.2	13.4	20.7	29.9	42.1	44.8
1-2	2.8	6.9	13.3	19.5	21.2	2.0
2-3	2.1	.9	9.2	11.1	.1	.9
3-4	4.3	1.5	19.4	16.4	2.5	2.2
4-5	3.4	1.2	10.7	9.3	1.9	2.4
5-6	2.7	1.1	11.4	15.0	1.8	2.3
6-7	-2.6	-3.2	15.6	19.1	12.1	1.7
7-8	12.8	2.9	16.6	10.4	13.6	23.3
8-9	9.4	1.2	12.3	9.4	1.6	16.5
9-10	2.7	-3.9	11.9	18.6	1.0	.9
10-11	.2	-4.2	16.6	12.6	1.9	19.0
12-13	12.0	28.4	13.9	41.9	1.4	1.3
16-17	-8.9	1.9	13.0	26.0	-3.4	2.7
					24.6	53.7
					3.8	6.5
						.76
						.18
						8.1

Table A-4. Summary of results as a function of season for entire data base.

CONDITIONS	Avg Residual	RMS Residual	Avg Rel. Res.	RMS Rel. Res.	Avg Abs Rel. Res.	Correlation	%
WINTER	1.0	8.7	18.1	30.0	2.3	43.7	.36
SPRING	1.8	1.3	16.2	19.3	.3	21.1	.71
SUMMER	2.7	3.2	14.4	17.7	.4	25.6	.72
FALL	2.4	5.7	16.5	24.0	.4	29.5	.41
						44.3	.69
						3.5	
						4.1	

Table A-5. Summary of results as a function of smoothed sunspot number for entire data base.

CONDITIONS	Avg Residual	RMS Residual	Avg Rel. Res.	RMS Rel. Res.	Avg Abs Rel. Res.	Correlation	%
0-30	-1.5	5.5	27.4	7.1	1.4	20.7	.74
30-60	.6	4.0	15.9	23.0	.5	31.5	.34
60-90	1.8	2.2	15.6	18.4	.4	29.9	3.4
90-120	6.1	8.1	15.4	24.6	.6	32.9	3.3
120-150	3.5	5.2	18.2	22.8	2.1	22.6	50.1
150-180	2.4	3.7	15.8	22.7	1.1	30.0	35.2
					.7	21.1	1.8
						1.1	

Table A-6. Summary of results as a function of midpath local time for entire data base.

CONDITIONS	Avg Residual	RMS Residual	Avg Rel Res.	RMS Rel Res.	Avg Abs Rel Res.	Correlation	%
1	2.6	18.6	1.9	.3	46.7	5.5	.56
2	1.8	18.6	-2.2	-2.6	41.1	6.2	.54
3	1.8	18.3	28.7	-1.7	19.0	1.5	.68
4	2.6	1.9	3.0	.6	16.5	5.2	.53
5	2.9	3.0	31.4	42.6	41.7	5.5	.51
6	3.2	1.3	18.8	41.7	49.7	4.7	.51
7	1.0	-1.2	16.0	2.1	54.6	4.8	.51
8	1.4	-1.2	16.1	-2.4	43.8	2.9	.52
9	2.0	-1.3	16.0	-1.7	37.4	4.8	.3.4
10	1.5	-2.0	14.6	2.1	16.7	1.4	.80
11	1.3	5.9	14.0	1.3	18.2	1.6	.64
12	.7	7.6	13.9	1.4	17.3	1.4	.62
13	.4	9.2	14.0	-1.8	15.4	1.6	.67
14	.8	10.6	14.2	1.0	21.8	1.6	.70
15	1.7	11.5	14.9	2.2	20.0	1.4	.73
16	2.0	10.5	14.9	2.5	33.7	2.2	.75
17	2.4	9.4	15.1	1.3	12.8	2.2	.76
18	1.5	7.2	14.9	1.4	13.4	1.6	.72
19	2.4	6.0	16.1	1.9	20.4	1.6	.70
20	2.2	5.4	15.8	2.8	19.5	2.2	.73
21	2.3	4.9	16.5	2.0	26.5	3.3	.69
22	3.0	4.4	17.4	2.5	24.2	2.5	.69
23	3.4	3.3	17.4	2.3	17.3	1.7	.71
24	2.9	2.9	17.9	1.6	20.8	1.7	.74
					22.1	3.0	.67
					50.1	5.2	.65
					18.0	1.5	.64
					13.4	2.1	.68
					2.5	3.3	.68
					25.3	2.2	.66
					2.0	1.3	.66
					1.3	1.7	.73
					20.8	2.2	.69
					30.8	3.5	.69
					3.1	4.1	.72
					34.1	4.1	.66
					6.4	7.2	.71
					30.6	3.1	.66
					42.0	6.6	.61
					43.4	3.0	.69
					33.1	3.1	.61
					33.0	2.4	.59
					25.5	3.2	.70